Characterizing hydraulic properties of fractured rocks using DFN model and FEMDEM method for tunnelling applications

Jin Wu

2021

Characterizing hydraulic properties of fractured rocks using DFN model and FEMDEM method for tunnelling applications

by

Jin Wu

A Dissertation

Submitted to Graduate School of Engineering

Kyoto University

In Partial Fulfilment of the Requirements

For *Doctor of Philosophy in Engineering*

September 2021

Acknowledgements

Firstly, I would like to express my sincere gratitude to my supervisor Prof. Koike for his invaluable advice, patience, and motivation during my Ph.D. study. His enormous knowledge and immense experience have helped me to be a qualified researcher, to publish a competent journal paper.

Besides my supervisor, I would like to offer my special thanks to Prof. Goto, who has greatly inspired and supported me during my Ph.D. study. He puts faith into me as a stranger to geophysics. He has also provided insightful discussions about my research.

Also, I would like to thank Prof. Kishida and Assoc. Prof. Nara for their precious comments on my Ph.D. thesis. I would also like to thank Assoc. Prof. Kashiwaya, Kubo-san, Watanabe-san, Tada-san, and my lab members, who have supported me.

I wish to express their grateful thanks to the Mizunami and Horonobe Underground Research Laboratory (URL), Japan Atomic Energy Agency (JAEA) for providing physical and mechanical properties of rock mass in the URLs and to Dr. Antonio Munjiza for his permission to use the Y-Geo code for the FEMDEM analysis in Chapters 4 and 5.

Last but not the least, I would like to thank my family and my girlfriend Yalin Chao for supporting me spiritually throughout my Ph.D. study.

Abstract

Fractures (e.g., faults, joints) provide pathways for fluid flow as hydraulic conductors or barriers that prevent flow across them. Characterization and detection of fractures in fractured rock mass have been of great interest in geotechnical, geological, geophysical, and hydraulic engineering practices. In particular, the relations between fractures and their physical properties (e.g., permeability, electrical resistivity, seismic velocity) are fundamental to understanding fractured rock mass in tunnelling. Among several methods, the discrete fracture network (DFN) modeling approach has high capability of characterizing natural rock fractures. For stress-induced fractures (e.g., induced fractures around tunnel excavation), the hybrid finite-discrete element method (FEMDEM) is effective to model fracture initialization and propagation in rock mass. In this thesis, several methods were proposed to characterize fracture patterns and their rock physical properties quantitively by the following six chapters.

Chapter 1 provides background information of fractures and their fractured rock physical properties (e.g., permeability, electrical resistivity, seismic velocity). Also, DFN modeling approach as well as FEMDEM which characterize fractures in the rock mass are introduced briefly.

Chapter 2 presents a method for estimating effective permeability of fractured rock mass by using discrete fracture networks constrained by electrical resistivity data. The permeability of fractured rock mass which is one of fundamental rock physical properties for engineering practice such as tunneling is difficult to be characterized without time-consuming hydraulic tests. DFN models can well represent fracture properties (e.g., fracture lengths, orientations, and densities) and their permeabilities can be estimated analytically using the Oda's crack tensor theory. The distribution of fracture lengths in a DFN model that is conventionally derived from traces maps observed on outcrops or tunnel walls is biased in general. To overcome this problem, a method than can constrain fracture lengths in DFN models using in-situ measured electrical resistivity data is proposed. To validate its rationality, two cases studies are carried out in the fractured rock mass of the Mizunami Underground Research Laboratory (URL) in the Tono area of central Japan. For Case 1, an optimal DFN model with a scaling exponent a = 3.0 was obtained with an in-situ measured resistivity of 2000 $\Omega \cdot$ m. The corresponding average effective permeability is $\bar{k}$ = 5.30×10^{-16} m^2, which is slightly smaller than the in-situ permeability 1.0×10^{-15} m^2. For Case 2, the calculated $\bar{k}$ is 1.18×10^{-14} m^2, which is around four times larger than the in-situ permeability of 2.67×10^{-15} m^2. Consequently, the proposed method can construct optimal DFN models based on in-situ electrical resistivity and then estimate their reasonable effective permeabilities.

Chapter 3 presents a conceptual model to interpret both increase in seismic velocity and electrical resistivity after a tunnel excavation in fractured rock mass. Excavation of a tunnel results in the formation of an excavation damaged zone (EDZ) in surrounding rock mass. Generally,

seismic wave velocity and electrical resistivity decrease after a tunnel excavation, because fractures initiate and propagate in EDZ. However, a special phenomenon where seismic velocity and electrical resistivity increased after tunnel excavation in the Horonobe Underground Research Laboratory (URL) was observed. A possible conceptual model for the phenomenon is proposed in this chapter. The conceptual model assumes that a decrease in liquid saturation around tunnel excavation induces the increases in seismic velocity and electrical resistivity in EDZ. The main cause of liquid saturation change originates from relative humidity variation in the tunnel. In addition, liquid saturation does not have a great influence on stress redistribution after excavation based on a hydro-mechanical modeling of excavation in a fractured rock mass using FlAC3D and TOUGH2. The rock gas saturations around the tunnel excavation surfaces increased after the tunnel excavation with decreasing in their increase rates. The electrical resistivities and seismic velocities in the rock mass were also increased. The numerical simulation incorporating our proposed model succeeds in explaining the phenomenon observed in the Horonobe URL.

Chapter 4 presents a model that links a unified pipe network method and FEMDEM fracture model for estimating equivalent permeability of fractured rock mass. Based on fractures in a fractured rock mass captured by a FEMDEM fracture model, a unified pipe network model that includes matrix pipes and fracture pipes is used to estimate equivalent permeability. Four representative cases studies were carried out to validate its applicability in calculating equivalent permeability. In Case 1 where a single fracture was embedded in a rock, k_{xx} decreased whereas k_{yy} increased as the fracture orientation increased from 0° to 90°, where the *x* and *y* axes are in the horizonal and vertical directions, respectively, and the angle is defined counterclockwisely from the *x* axis. In Case 2 where DFN models with different fracture densities were prepared, their equivalent permeabilities increased with increasing the fracture density increased in general. In Case 3 for a uniaxial compression test of rock specimen, both k_{xx} and k_{yy} increased with increasing the time step. Case 4 for simulating a deep tunnel excavation, permeabilities in different locations around the tunnel were also increased generally.

Chapter 5 presents a numerical method that calculates equivalent electrical resistivity of fractured rock mass using an approach similar to that of Chapter 4. The fracture initiation and propagation in intact rock mass is modeled by FEMDEM model and the electric potential through fractures is simulated by an adapted unified pipe network model. To validate our novel proposed model, four representative cases studies were carried out. The first case was to estimate equivalent resistivities of intact rock mass in which a single fracture was embedded. The change in resistivity was revealed with the change in fractured orientation, and its change pattern was different with the direction. In Case 2, resistivities of DFN models decreased as fracture densities increased. Another case presented a laboratory test for uniaxial compressive strength (UCS) with estimating resistivities of a rock specimen. The resistivities decreased with increasing the time step. The last

case clarified changes at different locations around the tunnel excavation, and the resistivities increased common to all the locations with increasing the time step.

Chapter 6 summarizes the main results obtained by this dissertation and describes future, essential works

Keywords: Fractures; DFN models; FEMDEM method; permeability; electrical resistivity; seismic velocity; tunnelling

Contents

List of Figures

List of Tables

Chapter 1

Introduction

1.1 Background of study

Fractures (e.g., joints, faults) are everywhere at different length scales in rocks and they are important for engineering practice such as tunnelling because they may serve as pathways of fluid flow or barriers that prevent flow across them (e.g., Ishibashi et al., 2016; Li et al., 2009; Wolfsberg, 1996). Fig. 1.1 shows fractures observed on a tunnel wall in the fractured crystalline rock mass in the Mizunami Underground Research Laboratory (URL) in the Tono area of central Japan. These fractures provide pathways for fluid flow into the tunnel.

Though the behavior of a single fracture is well understood through theoretical and laboratory investigations, it is still necessary to build predictive models and understand the behavior of complex fracture networks. The discrete fracture network (DFN) modeling approach has been implemented for characterizing geometrical characteristics of natural fractures in fractured rock. For fracture initiation and propagation in intact rock, the hybrid combined finite-discrete element (FEMDEM) fracture model (Lisjak and Grasselli, 2014; Munjiza, 2004; Munjiza et al., 1995) is efficient. Understanding fracture network and fractured rock physical properties (e.g., permeability, electrical properties, seismic properties) is essential in geological, geotechnical, geophysical, and hydrological practices. Theoretical studies can provide the fundamental physical properties and relationships between parameters that describe the processes of fluid flow and transport, electrical conduction, and seismic wave propagation. Fig. 1.1 also shows the general focus of this dissertation. The DFN modeling approach is used to characterize geometrical properties of natural fractures. The FEMDEM fracture model is used to capture fracture initiation and propagation in intact rock. The effective or equivalent permeability, electrical resistivity and seismic velocity of fractured rocks are further calculated using fracture networks modeled by the DFN model or the FEMDEM fracture model.

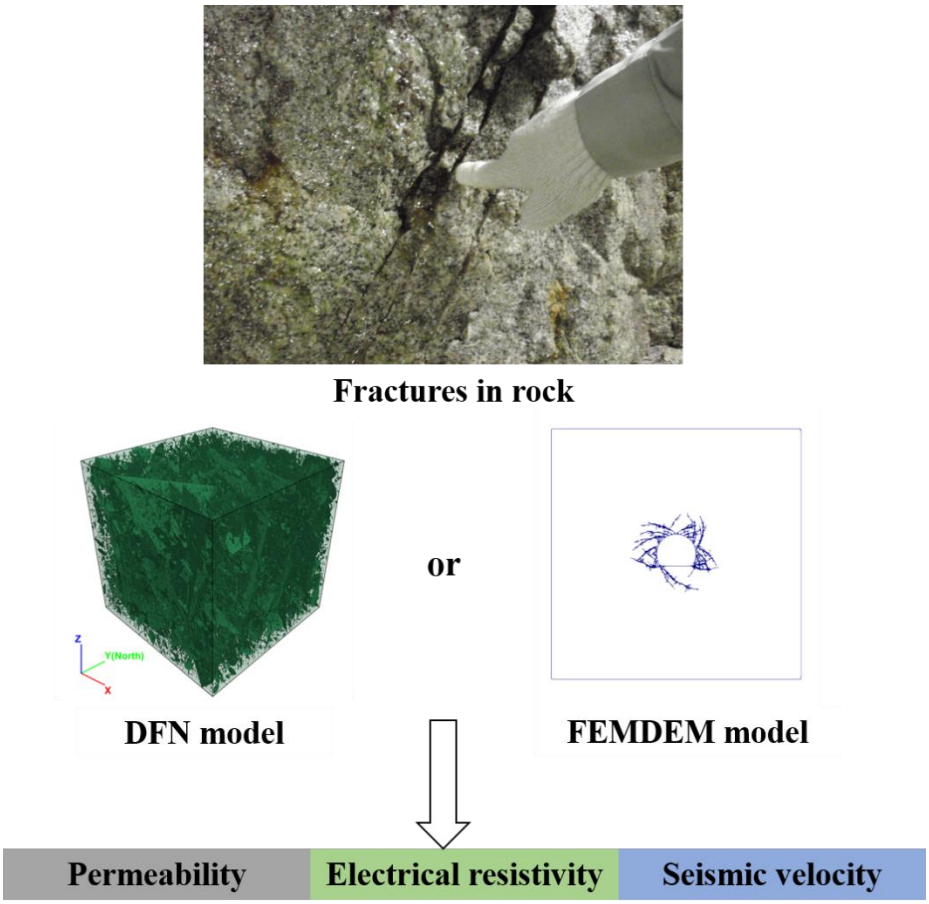

Fig. 1.1. The general focus of this dissertation on developing methods which calculate effective or equivalent permeability, electrical resistivity and seismic velocity of fractured rocks using fracture networks modeled by the DFN model or the FEMDEM model.

1.2 Description of fractures

DFN

The first step to characterize natural fractures in fractured rock is to represent their geometrical properties (e.g., fracture locations, lengths, orientations) explicitly. The DFN model which refers to a mathematical representation of fracture characteristics of each single fracture is widely used to characterize natural fractures (Lei et al., 2017). The DFN modeling approach used to generate fractures is stochastic. One of advantages of DFN modeling approach is that geometrical characteristics of fractures can be represented through stochastic simulations. Another advantage is that it can preserve fracture connections in the fracture network. The geometrical characteristics of fractures which are usually obtained from field data are typically sampled through independent statistical distributions. Fractures are viewed as planar polygons or disks in 3D or line segments in 2D (Baecher, 1983). There are three key properties to be defined for a DFN model: fracture density, fracture orientation and fracture size. The spatial distribution

of fracture locations which are usually populated by the Poisson process is constrained through fracture density. The total surface (mass) of fracture per unit volume (P_{32}, P_{21}, and P_{10}) is the common definition for the fracture density (Dershowitz and Herda, 1992). In 3D. P_{32} is the cumulated fracture surface area per unit volume. In 2D, P_{21} is the cumulated length of fracture per unit surface. In 1D, P_{10} is the number of fractures intersected by unit length of the scanline. Fractures are grouped into different sets with similar orientations by a Gaussian, Fisher, or a uniform distribution (Baecher, 1983; Einstein and Baecher, 1983). Various field studies have shown that fractures scale to scaling laws such as power laws (Baecher, 1983; Barton, 1981; Bonnet et al., 2001; Bour, 2002; Davy et al., 2010; Lei et al., 2015). The fracture size distributions are often be fitted into scaling laws from fracture traces observed on outcrop/tunnel surfaces. Defining fracture size has been problematic because fracture traces obtained from outcrop/tunnel surfaces are not actually fracture sizes. Though Follin et al. (2014) has tried to constrain fracture sizes of DFN model using hydrogeological data obtained from hydraulic tests, more research are needed to study on it. In this dissertation, a novel method which constrains fracture lengths of fracture networks using the in-situ measured electrical resistivity data is proposed. Fig. 1.2a shows a DFN model from geology information obtained from the fractured crystalline rock mass of the Mizunami Underground Research Laboratory (URL) in the Tono area of central Japan. Fig. 1.2b shows an optimal DFN model constrained by the in-situ measured electrical resistivity.

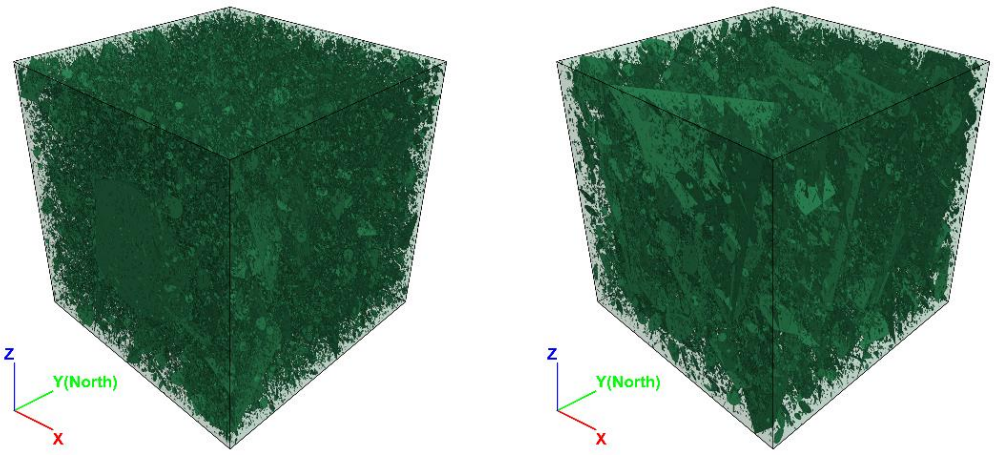

(a) (b)

Fig. 1.2. Fracture networks constructed by the DFN modeling approach (Wu et al., 2021)): (a) a DFN model from geology information obtained from the fractured crystalline rock mass of the Mizunami Underground Research Laboratory (URL) in the Tono area of central Japan; (b): an optimal DFN model of which fracture lengths are constrained by the in-situ observed electrical resistivity data. For more information, please see Chapter 2.

FEMDEM

A hybrid finite-discrete element method (FEMDEM) has been developed to model fracture development in rock masses using a cohesive zone approach (Lisjak and Grasselli, 2014; Munjiza, 2004; Munjiza et al., 1995). The computational domain is meshed into 2D unstructured triangular elements between which four-node joint elements are embedded between triangular elements in (Fig. 1.3a). A linear elastic finite element analysis is used to calculate rock matrix deformation captured by triangular elements. In contrast, the fracture behaviors are characterized by four-node joint elements. Three types of modes are defined to characterize failure of joint elements: Mode I, Mode II, and a mixed mode of Mode I and Mode II. The failure criterion of joint elements is shown in Figs. 1.3b, 1.3c, and 1.3d, respectively. The hybrid FEMDEM can well characterize fracture development in fractured rock due to local stress perturbation such as tunnel excavation. Figs. 1.3e and 1.3f show two representative cases of fracture development in intact rock simulated by the hybrid FEMDEM. Fig. 1.3e shows fracture propagation in a rock sample under a uniaxial compressive strength (UCS) test which is for determining uniaxial compressive strength. Fig. 1.3f shows fracture development around tunnel excavation simulated by FEMDEM. The excavation damaged zone (EDZ) develops gradually around tunnel. The Y-Geo in which FEMDEM is embedded is used to model fracture development.

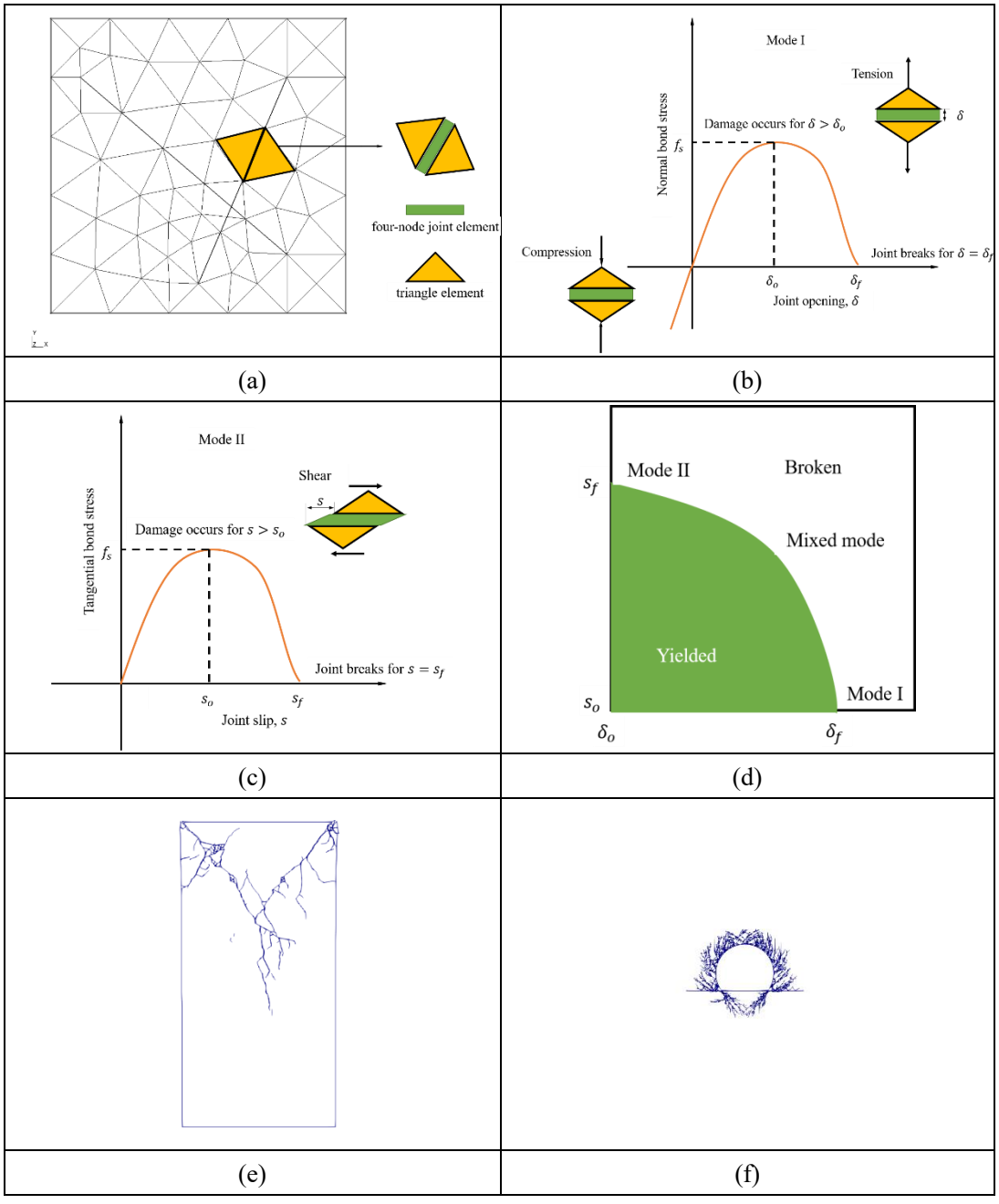

Fig. 1.3. The hybrid FEMDEM: (a) 2D unstructured mesh of triangular elements surrounded by four-node joint elements; (b) Mode I characterizing tension fracture; (c) Mode II characterizing shear fracture; (d) Mixed mode of Mode I and Mode II. (a), (b), (c), and (d) are modified from (Lisjak et al., 2014); (e) fracture development in rock sample under uniaxial compression; (f) fracture development around tunnel excavation. For more information, please see Chapter 4 or 5.

1.3 Hydraulic properties

Permeability

Fractured rock permeablity is one of fundamental rock physical properties for characterizing fluid flow in rock mass. It can be estimated through various laboratory tests, field hydraulic tests using packers, and numerical upscaling methods (e.g., Sævik and Nixon, 2017; Hamm et al., 2007). Among them, laboratory and filed tests are time-consuming (Wolfsberg, 1996). Thus, various analytical and numerical methods have been developed to estimate fractured rock permeability. The numerical upscaling methods can be based on the equivalent continuum model which includes dual porosity (Barenblatt et al., 1960; Warren and Root, 1963), dual permeability (Vogel et al., 2000) and multi-continuum method (Pruess and Narasimhan, 1982; Pruess et al., 1999), the discrete fracture-matrix model (Karimi-Fard et al., 2003; Sandve et al., 2012), discrete fracture network model (e.g., Valera et al., 2017), and pipe network model (e.g., Dershowitz and Fidelibus, 1999; Hadgu et al., 2017). The numerical upscaling methods demand high computational resources, analytical methods (e.g., Oda's crack tensor theory (Oda, 1986)) also be also used. The analytical models and the DFN modeling approach can be jointly used to estimate fracture rock permeability. It is still necessary to constrain DFN models because fracture lengths in the DFN models which are inferred from fracture traces observed on outcrops and tunnel walls are biased (Mak, 2014). Based on constrained DFN models and analytical methods (e.g., Oda's crack tensor theory), realistic fractured rock permeabilities can be estimated.

Electrical properties

Fractures (e.g., faults, joints) provide pathways for fluid flow as hydraulic conductors or barrier that prevent flow across them (Wolfsberg, 1997). Characterization and detection of fractures in fractured rock has been of great interest in geotechnical, geological, geophysical, and hydraulic engineering. The higher conductivity of water-filled fractures than intact rock makes electrical methods and electromagnetic methods possible to detect of water-filled fracture because water-filled fractures have higher electrical conductivities than intact rock. The mobility of conductive ions in the water that moves through fractures, fracture fillings dominated by clay minerals, and fracture network connectivity cause that fractures have higher electrical conductivities than intact rock (Elis et al., 2019; SEKINE et al., 1997; Wolfsberg, 1997). Though various laboratory experiments have been made to determine electrical properties of rocks (e.g., Brace and Orange, 1966, 1968; Wang et al., 1978), there are quite limited papers which study the relationship between fractures and electrical properties of rocks. By contrast, numerical methods that estimate the effective or equivalent electrical resistivity or conductivity of fractured rock have been developed by utilizing the analogy between Darcy's law and Ohm's law that describe fluid flow and electrical flow, respectively (e.g., Bahr, 1997; Brown, 1989; Kirkby et al., 2016; Kirkby

and Heinson, 2017; Sanz et al., 2017). Alternative to numerical methods, effective medium methods including the self-consistent approximation, the Maxwell approximation, the T-matrix approximation, etc. have also been developed (e.g., Saevik et al., 2014). The geometrical properties of fractures used in those methods are described by certain statistical distributions of natural fractures in rocks. The discrete fracture network (DFN) modelling approach provides possible statistical descriptions of natural fractures (e.g., Dverstorp and Andersson, 1989; Lei et al., 2017). The variations in electrical resistivity of fractures caused by the initiation and propagation of fractures in intact rock are not well described by the DFN modeling approach. Instead, the hybrid finite-discrete element method (FEMDEM) has been developed to simulate fracture initialization and propagation due to local stress perturbations (e.g., tunnel excavations) in intact rock (Lisjak and Grasselli, 2014; Munjiza, 2004; Munjiza et al., 1995). To our best knowledge, there is no research that has been made to estimate equivalent electrical resistivity of fractures characterized by the FEMDEM fracture model.

Seismic properties

Fractures (e.g., faults, joints) provide pathways for fluid flow as hydraulic conductors or barrier that prevent flow across them (Wolfsberg, 1997). Fractures in fractured rock are zones of anomaly physical properties. It is a challenging issue to quantify the geometric parameters of a fracture which are described by its location, size, orientation, etc. (Boadu and Long, 1996). Many efforts have been made to characterize their geometric properties through geological observations, hydraulic and tracer tests though these experiments are expensive and time-consuming in their operation. The remote detection and characterization of fractures in fractured rock has been of great interest in engineering practice. Various geophysical methods (e.g., seismic methods, electrical methods, etc.) which detect and characterize fractures indirectly have been developed (Adepelumi et al., 2006; Day-Lewis et al., 2017; Robinson et al., 2016; Seaton and Burbey, 2002). Since elastic properties can be estimated at greater ranges than electromagnetic and electric properties, seismic methods have been the most useful tools for imaging and mapping fractures remotely. Rock fractures change the amplitudes and traveltimes of seismic waves that travel through them. Attempts have been made to study effects of fractures on seismic waves through theoretical, experimental, and numerical investigations (Anderson et al., 1974; Berryman, 2007; Boadu and Long, 1996; Hudson, 1981, 1981; Pyrak-Nolte et al., 1990; Schoenberg and Sayers, 1995; Yang et al., 2019; Zhu et al., 2020). Since the presence of fractures result in the azimuthal variations of P-wave attributes, it is possible to estimate of fracture parameters from azimuthal analysis of P-wave velocities. Amplitude versus offset (AVO) analysis of seismic wave data has also been successful in characterizing fracture orientations (e.g., Montoya et al., 2002; Pérez et al., 1999). Based on the dependence of anisotropy on frequency because of fractures in the rock

mass, it is possible to characterize fractures using the frequency-dependent seismic wave anisotropy analysis (Al-Harrasi et al., 2011; Maultzsch et al., 2003). The seismic method which is most important geophysical technique is valuable for detection and characterization of fractures (Germán Rubino et al., 2013). Seismic wave attenuation is recognized as a common phenomenon observed in fractured rocks since seismic energy loss is significant in the presence of fractures. Understanding seismic attenuation across fractures can help improve detection and characterization of fracture in fractured rocks. Seismic wavelengths are much longer than fracture lengths, it is difficult to relate measured seismic attributes to fractures (Hunziker et al., 2018). Many analytical effective medium models (e.g., Galvin and Gurevich, 2015; Kong et al., 2017; Song et al., 2020) as well as numerical methods (e.g., Chen et al., 2019, 2018; De Basabe et al., 2016; Hunziker et al., 2018; Möller and Friederich, 2019; Zhan et al., 2017) are available to study relationships between seismic waves and fracture properties (e.g., fracture density, length, orientation). The Biot-Gassmann theory is a widely used model to describe the relationship between seismic velocities and rock physical properties of fractured rock (Biot, 1956; Gassmann, 1951; Gutierrez et al., 2012; Lee, 2002).

1.4 Research objectives

The general objective of this dissertation is to study on relationships between fractures and their rock physical properties (e.g., permeability, electrical resistivity, and seismic velocity). The relationship between fractures and their physical properties helps assess rock mass behavior for tunnelling applications. The DFN modeling approach is used to characterize geometrical properties of natural fractures. The fracture initiation and propagation in the intact rock is captured by the hybrid FEMDEM fracture model. There are still several issues that need further investigations. One issue is that unrealistic DFN models maybe generated if fracture lengths in a DFN model are conventionally derived from trace length measurements (Mak, 2014). A phenomenon observed in the Horonobe underground research laboratory that seismic velocities and electrical resistivities around tunnel excavation surfaces increased after tunnel excavation. There is still not a conceptual model that can explain such phenomenon. Another issue that there is quite limited research on estimating equivalent permeability/electrical resistivity change in a rock sample under a uniaxial compression test or in a rock mass where a tunnel is excavated. The overview of existing issues is shown in Fig. 1.4. Considering these issues, several methods are proposed in the dissertation. The main objectives are summarized as follows:

1. To develop a method for estimating fractured rock effective permeability by using discrete fracture networks constrained by electrical resistivity data.
2. To propose a conceptual model interpreting an increase in seismic velocity and electrical resistivity after a tunnel excavation in fractured rock.

3. To present a model which links a unified pipe network method and FEMDEM fracture model for estimating equivalent permeability of fractured rock masses.
4. To propose a numerical method that calculates equivalent fractured rock electrical resistivity through a combination of the hybrid FEMDEM fracture model and the unified pipe network model.

The novelty of this thesis lies in the following:

1. Electrical resistivity data is used to constrain fracture lengths in a DFN model. Based on a constrained DFN model, a realistic permeability can be estimated.
2. A phenomenon observed in the Horonobe URL that seismic velocities and electrical resistivities increase around tunnel is explained by a conceptual model. The conceptual model is validated through a numerical simulation.
3. The equivalent permeability/electrical resistivity change in a rock sample under a uniaxial compression test and a rock mass where a tunnel is excavated is estimated.

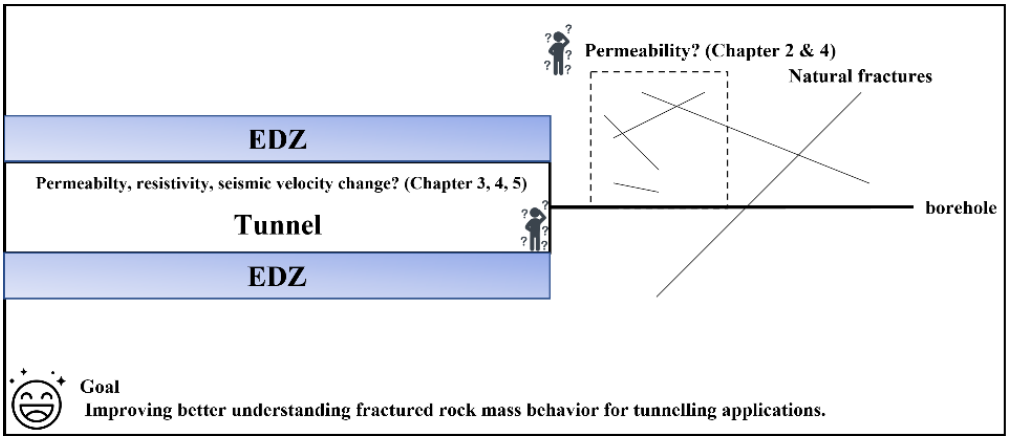

Fig. 1.4. An overview of existing issues with regard to fractures and their physical properties.

1.5 Dissertation structure

This dissertation intends to study the relationship between fracture network and fractured rock physical properties (e.g., permeability, electrical resistivity, seismic velocity). The fractures in rock mass are characterized either by a DFN model or a hybrid FEMDEM method. The proposed models were applied in tunnelling applications. There are 6 chapters in total.

Chapter 1: Introduction

This chapter provides background information of fracture network (which is characterized by DFN models or a hybrid FEMDEM method) and fractured rock physical properties (e.g., permeability, electrical resistivity, seismic velocity).

Chapter 2: A method for estimating fractured rock effective permeability by using

discrete fracture networks constrained by electrical resistivity data

This chapter was previously published by *Engineering Geology*, *Estimating fractured rock effective permeability using discrete fracture networks constrained by electrical resistivity data* (Wu et.al., 2021). This chapter studies on fractured rock permeability which is one of rock physical properties using fracture networks described by DFN models. The chapter focus on interpreting fractured rock permeability and DFN models which are constrained by electrical resistivity data. The DFN models are biased without any constraints. The electrical resistivity data was used to constrain fracture lengths in the DFN models. Then, fractured rock effective permeability of constrained DFN models are estimated using an improved version of Oda's crack tensor theory. The electrical resistivity data as well as geological data which constructed DFN models were obtained from an advanced borehole in tunnelling.

The chapter presents a method for estimating fractured rock effective permeability by using discrete fracture networks constrained by electrical resistivity data. Although the permeability of fractured rock mass is a fundamentally important property for the safe construction of civil and mining engineering structures such as tunnels, the in-situ characterization of the permeability without resorting to hydraulic tests is difficult. For a quick estimate over a wide area, a method at a field-scale using geological and geophysical investigation data is proposed. The method is not based on the results of conventional hydraulic tests. Instead, it combines the stochastic generation of fracture networks with the crack tensor theory. The most important parameter for this method is the fracture length distribution. Although the distribution parameters in the DFN model are assigned through sampling, a bias is in general experienced, because of the limited sampling area. To improve the estimation of such parameter, in-situ electrical resistivity data and a symmetric self-consistent method are used as a constraint of the fracture length distribution. The proposed method is applied to the fractured crystalline rock mass of the Mizunami Underground Research Laboratory (URL) in the Tono area of central Japan. Its effectiveness and correctness are demonstrated through good correspondence of the derived permeability with the in-situ measured permeability.

Chapter 3: A conceptual model interpreting an increase in seismic velocity and electrical resistivity after a tunnel excavation in fractured rock

This chapter also uses DFN models to characterize fracture networks in the rock mass. Based on DFN models, fractured rock electrical resistivity and seismic velocity are estimated. This chapter proposed a model interpreting relation between seismic velocity and electrical resistivity and DFN models in tunnelling. Chapter 2 did not involve any mechanical analysis due to tunnelling in interpreting relations between fractures and rock physical properties. This chapter studied rock physical properties change due to a tunnel excavation in fracture rock mass.

The chapter presents a conceptual model interpreting an increase in seismic velocity and

electrical resistivity after a tunnel excavation in fractured rock. Excavation of a tunnel results in formation an excavation damaged zone (EDZ) in surrounding rock. Generally, seismic wave velocity and electrical resistivity decrease after a tunnel excavation because fractures initiate and propagate in the EDZ. However, a special phenomenon where seismic velocity and electrical resistivity increased after tunnel excavation in the Horonobe Underground Research Laboratory (URL) was observed. A possible conceptual model which interprets such phenomenon is proposed in this chapter. The conceptual model assumes that a decrease in liquid saturation around a tunnel after excavation increases seismic velocity and electrical resistivity in the EDZ. The main cause of liquid saturation change comes from relative humidity variation in the tunnel. Also, liquid saturation does not have a great influence on stress redistribution after excavation based on a hydro-mechanical modeling of excavation in a fractured rock using FlAC3D and TOUGH2. A discrete fracture network (DFN) modeling method to describe natural fractures in the rock mass. The numerical simulation incorporating our proposed model succeeds in explaining the phenomenon observed in the Horonobe URL.

Chapter 4: Estimating fractured rock equivalent permeability using fractures characterized by FEMDEM method

Chapter 4 continues to study relationship between fractures and their rock physical properties. Instead of using DFN models which characterize fractures, this chapter uses DFN models and FEMDEM method to characterize fractures in the rock mass. Both static and dynamic evolution of fracture rock permeability were studied.

The chapter presents a model which links a unified pipe network method and FEMDEM fracture model for estimating equivalent permeability of fractured rock masses. A unified pipe network method is implemented into a combined finite-discrete element (FEMDEM) method to estimate equivalent permeability of a fractured rock mass. Based on fractures in a fractured rock captured by a FEMDEM fracture model, a unified pipe network which includes matrix pipe network and fracture pipe network is used to estimate equivalent permeability. Four case studies including a single fracture embedded in a rock, DFN models with different densities, a uniaxial test of a rock sample and a fractured rock in which a tunnel is excavated are carried out to verify the ability of integration of unified pipe network and FEMDEM fracture model to calculate equivalent permeability of a fractured rock.

Chapter 5: Estimating fractured rock equivalent electrical resistivity using fractures characterized by FEMDEM method

The unified pipe network that used in Chapter 4 can also be used to estimate fractured rock electrical resistivity by making an analogy between Darcy's law and Ohm's law. The FEMDEM method that used in Chapter 4 is also applied in this chapter for characterizing fractures initialization and propagation.

The chapter presents a numerical method that calculates the equivalent fractured rock electrical resistivity through a combination of the hybrid FEMDEM fracture model and the unified pipe network model. The fracture initiation and propagation in intact rock is modeled by the hybrid finite-discrete element (FEMDEM) fracture model. The electric potential through fractures is simulated by an adapted unified pipe network model. The variations of the equivalent electrical resistivity due to the initial and propagation of fractures in intact rock can be estimated jointly using the hybrid FEMDEM fracture model and the unified pipe network model. To validate our novel proposed model, four representative cases studies were carried out. The first case is to estimate the equivalent electrical resistivity of intact rock in which a single fracture is embedded. In Case 2, resistivities of DFN models with different fracture densities were calculated. Another case presented a uniaxial compressive strength (UCS) laboratory test which estimates the variations of electrical resistivity of fracture networks developed in rock. The last case shows electrical resistivities of different locations near the tunnel excavation surface which capture the initiation and propagation due to a local excavation in the rock mass.

Chapter 6: Conclusion

This chapter summarizes various models proposed in this dissertation.

The general flowchart showing thesis structure is shown in Fig. 1.5.

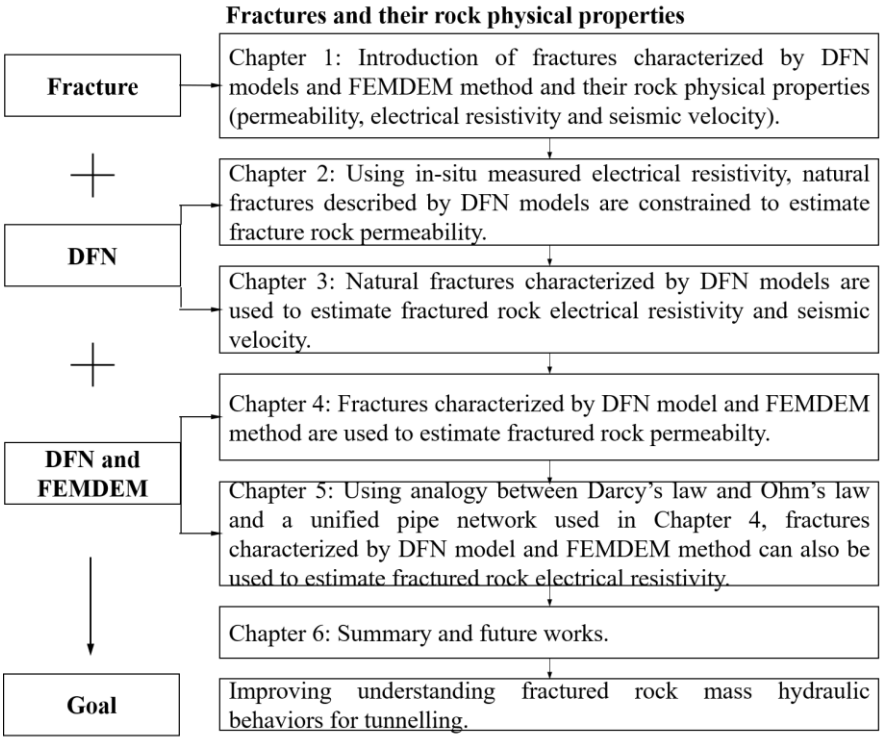

Fig. 1.5. Flowchart showing thesis structure.

References

Adepelumi, A.A., Yi, M.J., Kim, J.H., Ako, B.D., Son, J.S., 2006. Integration of surface geophysical methods for fracture detection in crystalline bedrocks of southwestern Nigeria. Hydrogeol. J. 14, 1284–1306. https://doi.org/10.1007/s10040-006-0051-2

Al-Harrasi, O.H., Kendall, J.M., Chapman, M., 2011. Fracture characterization using frequency-dependent shear wave anisotropy analysis of microseismic data. Geophys. J. Int. 185, 1059–1070. https://doi.org/10.1111/j.1365-246X.2011.04997.x

Anderson, D.L., Minster, B., Cole, D., 1974. The effect of oriented cracks on seismic velocities. J. Geophys. Res. 79, 4011–4015. https://doi.org/10.1029/jb079i026p04011

Baecher, G.B., 1983. Statistical analysis of rock mass fracturing. J. Int. Assoc. Math. Geol. 15, 329–348. https://doi.org/10.1007/BF01036074

Bahr, R., 1997. Electrical anisotropy and conductivity distribution functions of fractal random networks and of the crust: The scale effect of connectivity. Geophys. J. Int. 130, 649–660. https://doi.org/10.1111/j.1365-246X.1997.tb01859.x

Barenblatt, G.., Zheltov, I.., Kochina, I.., 1960. Basic concepts in the theory of seepage of homogeneous liquids in fissured rocks [strata]. J. Appl. Math. Mech. 24, 1286–1303. https://doi.org/10.1016/0021-8928(60)90107-6

Barton, N., 1981. Some size dependent properties of joints and faults. Geophys. Res. Lett. 8, 667–670. https://doi.org/10.1029/GL008i007p00667

Berryman, J.G., 2007. Seismic waves in rocks with fluids and fractures. Geophys. J. Int. 171, 954–974. https://doi.org/10.1111/j.1365-246X.2007.03563.x

Biot, M.A., 1956. Theory of propagation of elastic waves in a fluid-saturated porous solid, I: Low-frequency range. J. Acoust. Soc. Am. 28, 168–191. https://doi.org/10.1121/1.1908241

Boadu, F.K., Long, L.T., 1996. Effects of fractures on seismic-wave velocity and attenuation. Geophys. J. Int. 127, 86–110. https://doi.org/10.1111/j.1365-246X.1996.tb01537.x

Bonnet, E., Bour, O., Odling, N.E., Davy, P., Main, I., Cowie, P., Berkowitz, B., 2001. Scaling of fracture systems in geological media. Rev. Geophys. 39, 347–383. https://doi.org/10.1029/1999RG000074

Bour, O., 2002. A statistical scaling model for fracture network geometry, with validation on a multiscale mapping of a joint network (Hornelen Basin, Norway). J. Geophys. Res. 107. https://doi.org/10.1029/2001jb000176

Brace, W.F., 1975. Dilatancy-related electrical resistivity changes in rocks. Pure Appl. Geophys. PAGEOPH 113, 207–217. https://doi.org/10.1007/BF01592911

Brace, W.F., Orange, A.S., 1968. Electrical resistivity changes in saturated rocks during fracture and frictional sliding. J. Geophys. Res. 73, 1433–1445. https://doi.org/10.1029/jb073i004p01433

Brace, W.F., Orange, A.S., 1966. Electrical resistivity changes in saturated rock under stress. Science (80-.). 153, 1525–1526. https://doi.org/10.1126/science.153.3743.1525

Brace, W.F., Orange, A.S., Madden, T.R., 1965. The effect of pressure on the electrical resistivity of water-saturated crystalline rocks. J. Geophys. Res. 70, 5669–5678. https://doi.org/10.1029/jz070i022p05669

Brown, S.R., 1989. Transport of fluid and electric current through a single fracture. J. Geophys. Res. 94, 9429–9438. https://doi.org/10.1029/JB094iB07p09429

Chen, G., Song, L., Liu, L., 2019. 3D Numerical Simulation of Elastic Wave Propagation in Discrete Fracture Network Rocks. Pure Appl. Geophys. 176, 5377–5390. https://doi.org/10.1007/s00024-019-02287-0

Chen, G., Song, L., Zhang, R.R., 2018. Modeling acoustic attenuation of discrete stochastic fractured media. Acta Geod. Geophys. 53, 679–690. https://doi.org/10.1007/s40328-018-0237-9

Davy, P., Le Goc, R., Darcel, C., Bour, O., De Dreuzy, J.R., Munier, R., 2010. A likely universal model of fracture scaling and its consequence for crustal hydromechanics. J. Geophys. Res. Solid Earth 115. https://doi.org/10.1029/2009JB007043

Day-Lewis, F.D., Slater, L.D., Robinson, J., Johnson, C.D., Terry, N., Werkema, D., 2017. An overview of geophysical technologies appropriate for characterization and monitoring at fractured-rock sites. J. Environ. Manage. 204, 709–720. https://doi.org/10.1016/j.jenvman.2017.04.033

De Basabe, J.D., Sen, M.K., Wheeler, M.F., 2016. Elastic wave propagation in fractured media using the discontinuous Galerkin method. Geophysics 81, T163–T174. https://doi.org/10.1190/GEO2015-0602.1

Dershowitz, W.S., Fidelibus, C., 1999. Derivation of equivalent pipe network analogues for three-dimensional discrete fracture networks by the boundary element method. Water Resour. Res. 35, 2685–2691. https://doi.org/10.1029/1999WR900118

Dverstorp, B., Andersson, J., 1989. Application of the discrete fracture network concept with field data: Possibilities of model calibration and validation. Water Resour. Res. 25, 540–550. https://doi.org/10.1029/WR025i003p00540

Einstein, H.H., Baecher, G.B., 1983. Probabilistic and statistical methods in engineering geology - Specific methods and examples part I: Exploration. Rock Mech. Rock Eng. 16, 39–72. https://doi.org/10.1007/BF01030217

Elis, V.R., Bondioli, A., Ustra, A.T., Carlos, I.M., Pozzo, H.Â.P.D., 2019. Resistivity imaging for identification of fracture zones in crystalline bedrock in Brazil. Sustain. Water Resour. Manag. 5, 1089–1101. https://doi.org/10.1007/s40899-018-0287-8

Follin, S., Hartley, L., Rhén, I., Jackson, P., Joyce, S., Roberts, D., Swift, B., 2014a. A methodology to constrain the parameters of a hydrogeological discrete fracture network model for sparsely fractured crystalline rock, exemplified by data from the proposed high-level nuclear waste repository site at Forsmark, Sweden. Hydrogeol. J. 22, 313–331. https://doi.org/10.1007/s10040-013-1080-2

Follin, S., Hartley, L., Rhén, I., Jackson, P., Joyce, S., Roberts, D., Swift, B., 2014b. A methodology to

constrain the parameters of a hydrogeological discrete fracture network model for sparsely fractured crystalline rock, exemplified by data from the proposed high-level nuclear waste repository site at Forsmark, Sweden. Hydrogeol. J. 22, 313–331. https://doi.org/10.1007/s10040-013-1080-2

Galvin, R.J., Gurevich, B., 2015. Frequency-dependent anisotropy of porous rocks with aligned fractures. Geophys. Prospect. 63, 141–150. https://doi.org/10.1111/1365-2478.12177

Gassmann, F., 1951. Elasticity of porous media. Vierteljahrsschr. Naturforsch. Gesselschaft 96, 1–23.

Germán Rubino, J., Guarracino, L., Müller, T.M., Holliger, K., 2013. Do seismic waves sense fracture connectivity? Geophys. Res. Lett. 40, 692–696. https://doi.org/10.1002/grl.50127

Gutierrez, M., Katsuki, D., Almrabat, A., 2012. Effects of CO2 Injection on the Seismic Velocity of Sandstone Saturated with Saline Water. Int. J. Geosci. 03, 908–917. https://doi.org/10.4236/ijg.2012.325093

Hamm, S.Y., Kim, M.S., Cheong, J.Y., Kim, J.Y., Son, M., Kim, T.W., 2007. Relationship between hydraulic conductivity and fracture properties estimated from packer tests and borehole data in a fractured granite. Eng. Geol. 92, 73–87. https://doi.org/10.1016/j.enggeo.2007.03.010

Hudson, J.A., 1981. Wave speeds and attenuation of elastic waves in material containing cracks. Geophys. J. R. Astron. Soc. 64, 133–150. https://doi.org/10.1111/j.1365-246X.1981.tb02662.x

Hunziker, J., Favino, M., Caspari, E., Quintal, B., Rubino, J.G., Krause, R., Holliger, K., 2018. Seismic Attenuation and Stiffness Modulus Dispersion in Porous Rocks Containing Stochastic Fracture Networks. J. Geophys. Res. Solid Earth 123, 125–143. https://doi.org/10.1002/2017JB014566

Basabe, J.D. De, Sen, M.K., Wheeler, M.F., 2016. Elastic wave propagation in fractured media using the discontinuous Galerkin method. https://doi.org/10.1190/geo2015-0602.1 81, T163–T174. https://doi.org/10.1190/GEO2015-0602.1

Wu, J., Goto, T. nori, Koike, K., 2021. Estimating fractured rock effective permeability using discrete fracture networks constrained by electrical resistivity data. Eng. Geol. 289, 106178. https://doi.org/10.1016/J.ENGGEO.2021.106178

Kirkby, A., Heinson, G., 2017. Three-dimensional resistor network modeling of the resistivity and permeability of fractured rocks. J. Geophys. Res. Solid Earth 122, 2653–2669. https://doi.org/10.1002/2016JB013854

Kirkby, A., Heinson, G., Krieger, L., 2016. Relating permeability and electrical resistivity in fractures using random resistor network models. J. Geophys. Res. Solid Earth 121, 1546–1564. https://doi.org/10.1002/2015JB012541

Kong, L., Gurevich, B., Zhang, Y., Wang, Y., 2017. Effect of fracture fill on frequency-dependent anisotropy of fractured porous rocks. Geophys. Prospect. 65, 1649–1661. https://doi.org/10.1111/1365-2478.12505

Lee, M.W., 2002. Modified Biot-Gassmann theory for calculating elastic velocities for unconsolidated and consolidated sediments. Mar. Geophys. Res. 23, 403–412.

https://doi.org/10.1023/b:mari.0000018195.75858.12

Lei, Q., Latham, J.P., Tsang, C.F., 2017. The use of discrete fracture networks for modelling coupled geomechanical and hydrological behaviour of fractured rocks. Comput. Geotech. https://doi.org/10.1016/j.compgeo.2016.12.024

Lei, Q., Latham, J.P., Tsang, C.F., Xiang, J., Lang, P., 2015. A new approach to upscaling fracture network models while preserving geostatistical and geomechanical characteristics. J. Geophys. Res. Solid Earth 120, 4784–4807. https://doi.org/10.1002/2014JB011736

Lisjak, A., Grasselli, G., 2014. A review of discrete modeling techniques for fracturing processes in discontinuous rock masses. J. Rock Mech. Geotech. Eng. https://doi.org/10.1016/j.jrmge.2013.12.007

Lisjak, A., Grasselli, G., Vietor, T., 2014. Continuum-discontinuum analysis of failure mechanisms around unsupported circular excavations in anisotropic clay shales. Int. J. Rock Mech. Min. Sci. 65, 96–115. https://doi.org/10.1016/j.ijrmms.2013.10.006

Mak, S.W., 2014. Assessing fracture network connectivity of prefeasibility-level high temperature geothermal projects using discrete fracture network modelling. https://doi.org/10.14288/1.0167612

Maultzsch, S., Chapman, M., Liu, E., Li, X.Y., 2003. Modelling frequency-dependent seismic anisotropy in fluid-saturated rock with aligned fractures: Implication of fracture size estimation from anisotropic measurements. Geophys. Prospect. 51, 381–392. https://doi.org/10.1046/j.1365-2478.2003.00386.x

Möller, T., Friederich, W., 2019. Simulation of elastic wave propagation across fractures using a nodal discontinuous Galerkin method-theory, implementation and validation. Geophys. J. Int. 219, 1900–1914. https://doi.org/10.1093/gji/ggz410

Montoya, P., Fisher, W., Marrett, R., Tatham, R., 2002. Estimation of fracture orientation and relative intensity using azimuthal variation of P-wave AVO responses and oriented core data in the Tacata Field, Venezuela. SEG Tech. Progr. Expand. Abstr. 21, 261–264. https://doi.org/10.1190/1.1817225

Munjiza, A., 2004. The Combined Finite-Discrete Element Method, The Combined Finite-Discrete Element Method. John Wiley & Sons, Ltd, Chichester, UK. https://doi.org/10.1002/0470020180

Munjiza, A., Owen, D.R.J., Bicanic, N., 1995. A combined finite-discrete element method in transient dynamics of fracturing solids. Eng. Comput. 12, 145–174. https://doi.org/10.1108/02644409510799532

Pérez, M.A., Gibson, R.L., Toksöz, M.N., 1999. Detection of fracture orientation using azimuthal variation of P-wave AVO responses. GEOPHYSICS 64, 1253–1265. https://doi.org/10.1190/1.1444632

Pruess, K., Narasimhan, T., 1982. A practical method for modeling fluid and heat flow in fractured porous media.

Pruess, K., Oldenburg, C.M., Moridis, G.J., 1999. TOUGH2 User's Guide Version 2.

Pyrak-Nolte, L.J., Myer, L.R., Cook, N.G.W., 1990. Transmission of seismic waves across single natural fractures. J. Geophys. Res. 95, 8617. https://doi.org/10.1029/JB095iB06p08617

Robinson, J., Slater, L., Johnson, T., Shapiro, A., Tiedeman, C., Ntarlagiannis, D., Johnson, C., Day-Lewis, F., Lacombe, P., Imbrigiotta, T., Lane, J., 2016. Imaging Pathways in Fractured Rock Using Three-Dimensional Electrical Resistivity Tomography. Groundwater 54, 186–201. https://doi.org/10.1111/gwat.12356

Saevik, P.N., Jakobsen, M., Lien, M., Berre, I., 2014. Anisotropic effective conductivity in fractured rocks by explicit effective medium methods. Geophys. Prospect. 62, 1297–1314. https://doi.org/10.1111/1365-2478.12173

Sævik, P.N., Nixon, C.W., 2017. Inclusion of Topological Measurements into Analytic Estimates of Effective Permeability in Fractured Media. Water Resour. Res. 53, 9424–9443. https://doi.org/10.1002/2017WR020943

Sanz, V.C., Roubinet, D., Demirel, S., Irving, J., 2017. 2.5-D discrete-dual-porosity model for simulating geoelectrical experiments in fractured rock. Geophys. J. Int. 209, 1099–1110. https://doi.org/10.1093/gji/ggx080

Schoenberg, M., Sayers, C.M., 1995. Seismic anisotropy of fractured rock. Geophysics 60, 204–211. https://doi.org/10.1190/1.1443748

Seaton, W.J., Burbey, T.J., 2002. Evaluation of two-dimensional resistivity methods in a fractured crystalline-rock terrane. J. Appl. Geophys. 51, 21–41. https://doi.org/10.1016/S0926-9851(02)00212-4

SEKINE, I., NISHIMAKI, H., ISHIGAKI, K., HARA, T., SAITO, A., 1997. Influence of fracture and its filling materials on rock resistivity. J. Japan Soc. Eng. Geol. 38, 213–223. https://doi.org/10.5110/jjseg.38.213

Song, Y., Hu, H., Han, B., 2020. Seismic attenuation and dispersion in a cracked porous medium: An effective medium model based on poroelastic linear slip conditions. Mech. Mater. 140, 103229. https://doi.org/10.1016/j.mechmat.2019.103229

Valera, M., Guo, Z., Kelly, P., Matz, S., Cantu, V.A., Percus, A.G., Hyman, J.D., Srinivasan, G., Viswanathan, H.S., 2017. Machine learning for graph-based representations of three-dimensional discrete fracture networks. Comput. Geosci. 22, 695–710. https://doi.org/10.1007/s10596-018-9720-1

Vogel, T., Gerke, H.H., Zhang, R., Van Genuchten, M.T., 2000. Modeling flow and transport in a two-dimensional dual-permeability system with spatially variable hydraulic properties. J. Hydrol. 238, 78–89. https://doi.org/10.1016/S0022-1694(00)00327-9

Wang, C.-Y., Sundaram, P.N., Goodman, R.E., 1978. Electrical Resistivity Changes in Rocks During Frictional Sliding and Fracture, in: Rock Friction and Earthquake Prediction. Birkhäuser Basel, pp. 717–731. https://doi.org/10.1007/978-3-0348-7182-2_10

Warren, J.E., Root, P.J., 1963. The Behavior of Naturally Fractured Reservoirs. Soc. Pet. Eng. J. 3, 245–255. https://doi.org/10.2118/426-PA

Wolfsberg, A., 1997. Rock fractures and fluid flow, contemporary understanding and applications, Rock fractures and fluid flow, contemporary understanding and applications. National Academy Press USA. https://doi.org/10.1029/97eo00345

Wolfsberg, A., 1996. Rock Fractures and Fluid Flow. https://doi.org/10.17226/2309

Yang, H., Duan, H.F., Zhu, J.B., 2019. Ultrasonic P-wave propagation through water-filled rock joint: An experimental investigation. J. Appl. Geophys. 169, 1–14. https://doi.org/10.1016/j.jappgeo.2019.06.014

Zhan, Q., Sun, Q., Ren, Q., Fang, Y., Wang, H., Liu, Q.H., 2017. A discontinuous Galerkin method for simulating the effects of arbitrary discrete fractures on elastic wave propagation. Geophys. J. Int. 210, 1219–1230. https://doi.org/10.1093/gji/ggx233

Zhu, J., Ren, M., Liao, Z., 2020. Wave propagation and diffraction through non-persistent rock joints: An analytical and numerical study. Int. J. Rock Mech. Min. Sci. 132. https://doi.org/10.1016/j.ijrmms.2020.104362

Chapter 2

Estimating effective permeability using DFN models constrained by resistivity data

2.1 Introduction

Fractures (e.g., joints, faults), which are geologic discontinuities, are ubiquitous at different length scales in crustal rocks: they can extend for millimeters to kilometers. Fractures are fundamentally important for engineering applications such as high-level radioactive waste disposal, enhanced geothermal systems, and underground construction because they might serve as pathways of fluid flow or barriers that prevent flow across them (e.g., Ishibashi et al., 2016; Li et al., 2009; Wolfsberg, 1996). Especially at excavations of underground tunnels in hard-rock masses, highly pressurized groundwater inflow in fractures causes geohazards (e.g., Li et al., 2009). Estimating the permeability of fractured rock masses persists as a challenging issue for studying fluid flow and transport behaviors in fractured rock masses. Permeability can exist as equivalent or effective permeability. The latter, an intrinsic rock property at a large homogenization scale with a representative elementary volume (REV) size (Lei et al., 2017b; Renard and De Marsily, 1997), is the main target of this study.

Generally, permeability can be measured using laboratory tests, field tests within boreholes, and numerically based upscaling algorithms (e.g., Sævik and Nixon, 2017). Field hydraulic tests using packers and water pumps in single or multiple boreholes are more reliable than laboratory tests for estimating the field-scale effective permeability of fractured rock mass over a size larger than REV (Hamm et al., 2007). Multiple-borehole hydraulic tests are used for measuring anisotropic permeability if the fractured rock is assumed homogeneous and anisotropic.

Typical difficulties hindering the use of such hydraulic tests are the high cost and the necessity of long experimental times (Wolfsberg, 1996). Numerical and analytical methods have been developed to characterize the main fractures hydraulically and to estimate permeability. Fluid flow and transport through fractured rock mass can be modeled using the Equivalent Continuum (EC), the Discrete Fracture-Matrix (DFM) model, Discrete Fracture Network (DFN), and Pipe Network (PN, e.g., Dershowitz and Fidelibus, 1999; Hadgu et al., 2017; Koike et al., 2015; Leung et al., 2012; Liu et al., 2019). The EC models are based on dual porosity (Barenblatt et al., 1960; Warren and Root, 1963), dual permeability (Vogel et al., 2000), and multi-continuum method (Pruess and Narasimhan, 1982; Pruess et al., 1999). However, EC models are inappropriate to simulate the fluid flow through a small number of large-scale fractures. A DFM model, which uses two-point or multi-point flux approximations to assess interactions between a rock matrix and fractures, has been well developed to model fluid flow in fractured rock masses

(Karimi-Fard et al., 2003; Sandve et al., 2012). For cases in which fractures provide predominant pathways of fluid flow in a rock mass with low permeability, a DFN model or a pipe network model is reliable (e.g., Valera et al., 2017).

Those numerically based methods engender requirements for high computational demand. Therefore, analytical methods such as the crack tensor theory (e.g., Oda, 1986) are applicable as alternatives. Analytical models might also use stochastically generated fracture DFNs. An important difficulty of DFN modeling is the incorrectness of the fracture length distribution that is inferred from the trace lengths obtained from outcrops and tunnel walls (Mak, 2014). Several simplifications are necessary for estimation of the distribution parameters, which might cause unrealistic DFN. Therefore, rational constraints are necessary for correction of the fracture length distribution. Although geophysical, hydrological, and geomechanical data have been used as constraints for stochastic DFN modeling (den Boer and Sayers, 2018; Dorn et al., 2013; Follin et al., 2014; Lei et al., 2014; Williams-Stroud et al., 2013), no method using electrical resistivity data has been proposed for constraining the fracture length distribution.

Herein, the electrical resistivity is selected as a novel constraint condition of a DFN because it is sensitive to permeable fractures through which much of the groundwater flows. The primary objective of this study is to estimate the effective permeability accurately and efficiently without hydraulic tests by combining DFN modeling and a crack tensor theory with a constraint by in-situ measured resistivity for fracture length distribution and upscaling of calculated permeability. The resistivity data used for this study originate from geological surveys conducted with borehole cameras and geophysical logging in a pilot borehole for tunnel excavation (Fig. 2.1). The constrained DFN model is then used to estimate upscaled permeability. The proposed method is applied to the fractured crystalline rock mass of the Mizunami Underground Research Laboratory in the Tono area of central Japan as a case study. Its effectiveness is demonstrated by comparing the estimated effective permeability with the in-situ measured permeability. This chapter is organized as follows. Section 2 introduces the DFN modeling approach, Oda's crack tensor theory and symmetric self-consistent method. Then, an overall workflow is presented in Fig. 2.2. Finally, two cases studies are conducted to validate our proposed method.

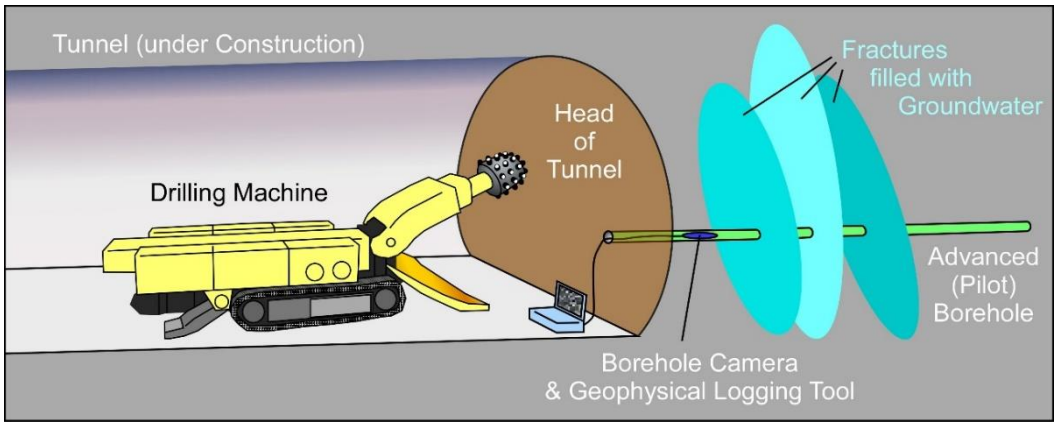

Fig. 2.1. Schematic view of an advanced (pilot) borehole. Camera and logging tools (e.g., electrical logging) are installed along an advanced hole.

2.2 Methods for calculating effective permeability

Discrete Fracture Network modeling

The first step is DFN modeling of fracture distribution because exact deterministic expression of fractures using limited field survey data from outcrops and scanlines is impossible. The DFN modeling expresses stochastic fracture properties such as fracture locations, shapes, lengths, orientations, and apertures and their correlations. Following traditional DFN modeling, this study adopted a homogeneous Poisson approach for fracture position (Xu and Dowd, 2010). This process is based on a random process controlled by a scale-averaging fracture density such as P_{10} or P_{32} in space (Dershowitz and Einstein, 1988). Actually, P_{32} is a scale-averaging volumetric measure of fracture intensity by the total fracture surface area per unit volume; P_{10} is the number of fractures per unit length. Because P_{32} cannot be estimated directly, it is derived from P_{10} using an analytical or a numerical method.

Fracture orientations were derived from the dip direction and angle data that were assumed to follow the von Mises–Fisher distribution with the following probability density function $f(\theta)$ as:

$$f(\theta) = \frac{\kappa \sin\theta e^{\kappa \cos\theta}}{e^{\kappa} - e^{-\kappa}} \tag{2.1}$$

where θ (°) stands for the standard deviation of the dip direction and angle and κ is a Fisher constant expressing dispersion of direction clusters. When κ is large, fractures are closely and parallelly distributed. Fracture orientations can be described as a Fisher distribution for $\kappa \geq 5$.

Fracture length distribution is usually derived from observed trace lengths and is assumed to follow a truncated power law by defining the minimum and maximum lengths (l_{min} and l_{max})(Lei et al., 2017b). A fracture size density distribution, $n(l)$, which describes the number of fractures per unit of volume in the range $[l, l + dl]$ $(dl \ll l)$, is used to set the fracture length distribution as shown below:

$$n(l) = \gamma l^{-a}, l \in [l_{min}, l_{max}] \quad (2.2)$$

In that equation, γ is a fracture density term and a is a scaling exponent. The total number of fractures with sizes in the range of $[l, l + dl]$ in a volume of characteristic size L, $N(l, L)$, is equal to the following:

$$N(l, L) = n(l)L^3 dl \quad (2.3)$$

If a computational domain is cubic, then L is the cube side length. It is noteworthy that L should be larger than or equal to the REV size. For the 3D space, γ is equal to P_{32} and $a \geq 2$ (Lei et al., 2017b). A fundamentally important difficulty is how to find an unknown a value correctly. Assuming that rock mass is saturated, the total volume of saturated fractures is proportional to the total length of fractures in the range $[l_{min}, l_{max}]$. Also, the fracture apertures are constant. In situ measured resistivity data were used to find a, as described in 2.3.

The fracture aperture has been regarded as correlated with the fracture length. Its distribution is generally approximated as a power law or a lognormal distribution (Lei et al., 2017a; Min et al., 2004). The uniform assumption is for cases without sufficient aperture data by observation.

Crack tensor theory

As a semi-analytical upscaling method to calculate the effective permeability of a fractured rock mass, Oda's crack tensor theory has been used widely by assuming the fracture shape as a penny disk (e.g., Koike et al., 2012; Oda 1986). By defining the position, size, and orientation of each disk, a quantity of fractures intersecting a block with volume V_e larger than REV, M_{ij}, can be expressed as the following:

$$M_{ij} = \frac{1}{V_e}\frac{\pi}{4} D^2 b^3 n_i n_j \quad (2.4)$$

Therein, D, b, and $n_i (i = 1,2,3)$, respectively represent the diameter, aperture, and the unit vector component of normal orientation of the fracture disk. The permeability k_{ij} (m^2) of V_e is then calculated using a discrete crack tensor approach (Rutqvist et al., 2013; Wang et al., 2014) as the following equation:

$$k_{ij} = \sum_{i=1}^{N} \frac{1}{12}\left(M_{kk}\delta_{ij} - M_{ij}\right) \quad (2.5)$$

In that equation, the so-called Oda's crack tensor theory, N represents the total number of fractures intersecting V_e; δ_{ij} is Kronecker's delta.

To avoid overestimation of fracture connectivity, an empirical connectivity parameter f for fractures that contribute considerably to effective permeability was introduced as shown below:

$$k_{ij} = \sum_{i=1}^{N} \frac{f}{12}\left(M_{kk}\delta_{ij} - M_{ij}\right) \tag{2.6}$$

In addition, f was given concretely as (Mourzenko et al., 2011):

$$f = \begin{cases} \dfrac{(\tau - \tau_c)^2}{\tau(1/\beta + \tau - \tau_c)}, & \tau \geq \tau_c \\ 0, & \tau < \tau_c \end{cases}, \tag{2.7}$$

where τ represents the mean number of intersections per fracture and τ_c stands for the percolation threshold. Eqs. (2.6) and (2.7) are the improved Oda's crack tensor theory, used in this study. Condition $\tau < \tau_c$ is for a disconnected fracture network; fracture permeability = 0. The combination of $\tau_c = 2.41$ and $\beta = 0.18$ is for the disk-shaped fracture set (Mourzenko et al., 2011; Sævik et al., 2013) used for this study.

The permeability tensor in the 3D space is expressed as shown below:

$$k_{ij} = \begin{bmatrix} k_{xx} & k_{xy} & k_{xz} \\ k_{yx} & k_{yy} & k_{yz} \\ k_{zx} & k_{zy} & k_{zz} \end{bmatrix}$$

Therein, $k_{xy} = k_{yx}$, $k_{xz} = k_{zx}$ and $k_{yz} = k_{zy}$ for a symmetric second-order tensor. Average effective permeability $\bar{k}$, the main rock-mass property of this study, is the average of diagonal components (Li et al., 2009) as presented below:

$$\bar{k} = \frac{1}{3}\left(k_{xx} + k_{yy} + k_{zz}\right) \tag{2.8}$$

Symmetric self-consistent method

Because the resistivity of rock mass is sensitive to the existence of fractures, in-situ measured resistivity data by geophysical logging in a pilot borehole before tunnel excavation are useful to constrain a DFN model, particularly the fracture length distribution. For this constraint, close matching between the calculated and measured resistivity of rock mass is indispensable. The symmetric self-consistent method (SSC; Sævik et al., 2013, 2014) for upscaling effective resistivity ρ_{ij} from resistivity data was used for this matching, because it can consider fracture interactions under large fracture density. In a homogeneous medium of matrix conductivity σ_m (inverse of resistivity) with *N* conductive fractures, ρ_{ij} is formulated as:

$$\rho_{ij} = \frac{1}{\tilde{\sigma}_{ij}\sigma_m} \tag{2.9}$$

$$\tilde{\sigma}_{ij} = \delta_{ij} + \frac{1}{3}\sum_{k=1}^{N} \frac{\varepsilon_k(2\alpha + 1)}{\lambda_k \alpha + \frac{\pi}{4}}\left(\delta_{ij} - n_i n_j\right) \tag{2.10}$$

where the following are true:

$$\alpha = 1 + \frac{2}{9}\sum_{k=1}^{N}\frac{\varepsilon_k(2\alpha+1)}{\lambda_k\alpha + \frac{\pi}{4}} \tag{2.11}$$

$$\varepsilon = \frac{4}{3}\pi\zeta r^3 \tag{2.12}$$

$$\lambda = \frac{\sigma_m}{\sigma_f\omega} \tag{2.13}$$

In those equations, ε represents the dimensionless fracture density, ζ denotes the number of fractures per unit volume, *r* stands for the fracture radius, σ_f denotes conductivity of saturated fracture, and ω expresses the fracture aspect ratio of aperture divided by diameter. Note that λ should be less than 1 in Eq. (2.13) for a numerical converge. Thus, $\sigma_f\omega$ requires site-dependent corrections for converge. Similarly to $\bar{k}$, average resistivity $\bar{\rho}$ is given by calculating the diagonal components of ρ_{ij} as shown below:

$$\bar{\rho} = \frac{1}{3}\left(\rho_{xx} + \rho_{yy} + \rho_{zz}\right) \tag{2.14}$$

Analytical flow

Estimation of $\bar{k}$ of a fractured rock mass was implemented along the flow chart in Fig. 2.2. The first step is construction of a DFN model using fracture data for orientation and density from borehole camera images and a truncated power law of the fracture length distribution.

The second step is calculation of $\bar{\rho}$ from the DFN model using SSC and comparison of $\bar{\rho}$ with the average of in-situ resistivity data from borehole loggings. If the difference is large, then the DFN model is modified by changing *a* value in Eq. (2.2). Otherwise $\bar{k}$ is calculated finally using the improved Oda's crack tensor.

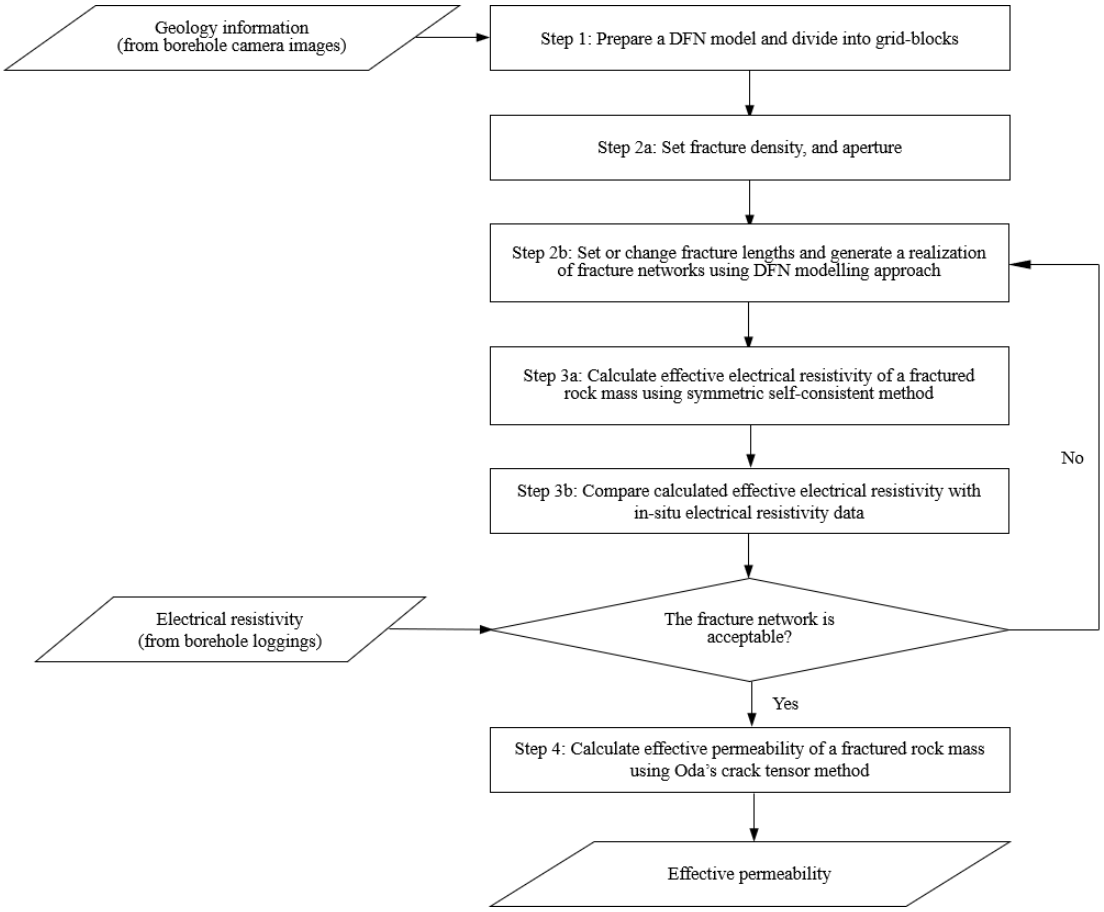

Fig. 2.2. Flowchart for calculating field-scale effective permeability of a fractured rock mass by combining the DFN model with the improved Oda's crack tensor with a constraint by in-situ measured resistivity data for the fracture length distribution.

2.3 Application to Field Data

Study site and fracture data

The proposed method was applied to permeability characterization of a part of the Mizunami Underground Research Laboratory (MIU) in Gifu Prefecture, central Japan (Fig. 2.3). This site is composed primarily of late Cretaceous biotite granite (Toki granite), the basement rock in this area. Multidisciplinary scientific studies have been implemented in the MIU project for clarifying deep geological environments, developing technologies to enhance the reliability of geological disposal of high-level-radioactive wastes (Japan Nuclear Cycle Development Institute, 2002), and investigating details of hydraulic properties of fractures and rock matrix (e.g., Koike et al., 2015; Kubo et al., 2019). Among them, geological surveys, geophysical logging, and packer tests were conducted along an N30°E horizontal borehole (12MI33) with total length of 102 m at 500 m depth (Fig. 2.3); fracture, resistivity, and permeability data were obtained as shown in Fig. 2.4 (Tsuyuguchi et al., 2014), whose data is published and available in our study. The study site is under the groundwater table. Rocks are saturated as described earlier reports (e.g., Tsuji et al.,

2017).

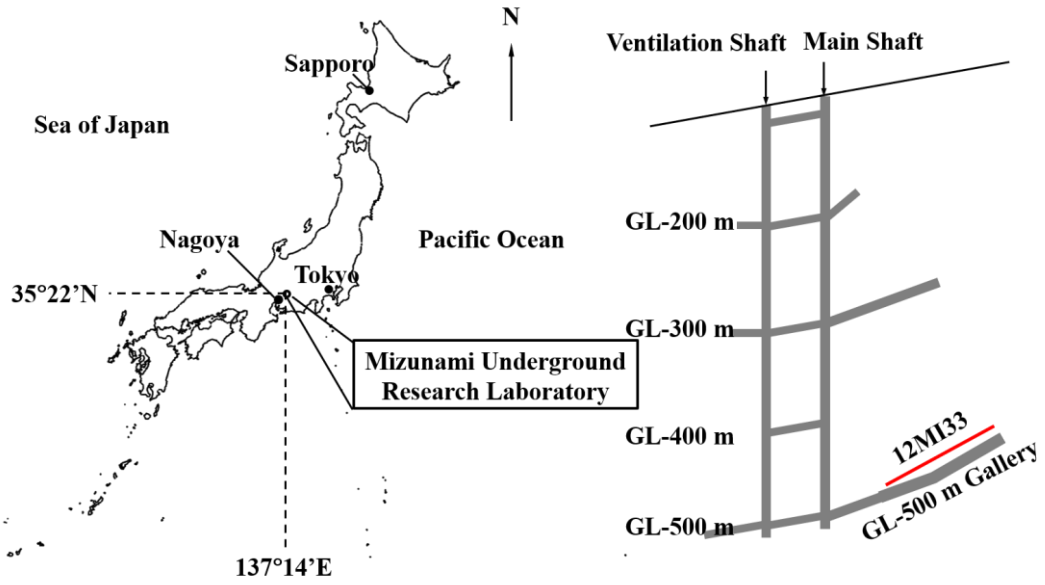

Fig. 2.3. Location map of the Mizunami Underground Research Laboratory and the borehole 12MI33 with 102 m length marked as a red line in the Tono area, central Japan. Geological surveys, electric logging, and hydraulic tests were implemented in 12MI33 at the 500-m-deep gallery.

From borehole televiewer images, 297 fractures were observed along borehole 12MI33. The typical observed results are summarized in Fig. 2.4c and Table 2.1. The fractures generally accompany filling minerals and argillic alterations composed of chlorite and epidote (Kubo et al., 2019; Yoshida et al., 2013). The filling minerals, materials, and water decrease the fracture resistivity to below the level of the rock matrix resistivity. This decline was confirmed by the low resistivity of the water samples collected from borehole 12MI33. Fractures were concentrated in the damage zone around a minor fault that appeared in the tunnel (gallery) along 12MI33 (Fig. 2.3), as shown in Figs. 2.4c and 2.4d (Tsuyuguchi et al., 2014), whose data is published and available in our study. Only 17 fractures were observed to be open with clear apertures of about 0.5 mm (Fig. 2.4c). Using spherical K-means clustering, the fractures were grouped into a single set with the average dip direction and angle shown in Table 2.1 (Kalinina et al., 2018). Parameter K in the von Mises–Fisher directional statistics was found as 7.0, which demonstrated that the fracture orientations are well approximated by the Fisher distribution (Kalinina et al., 2018).

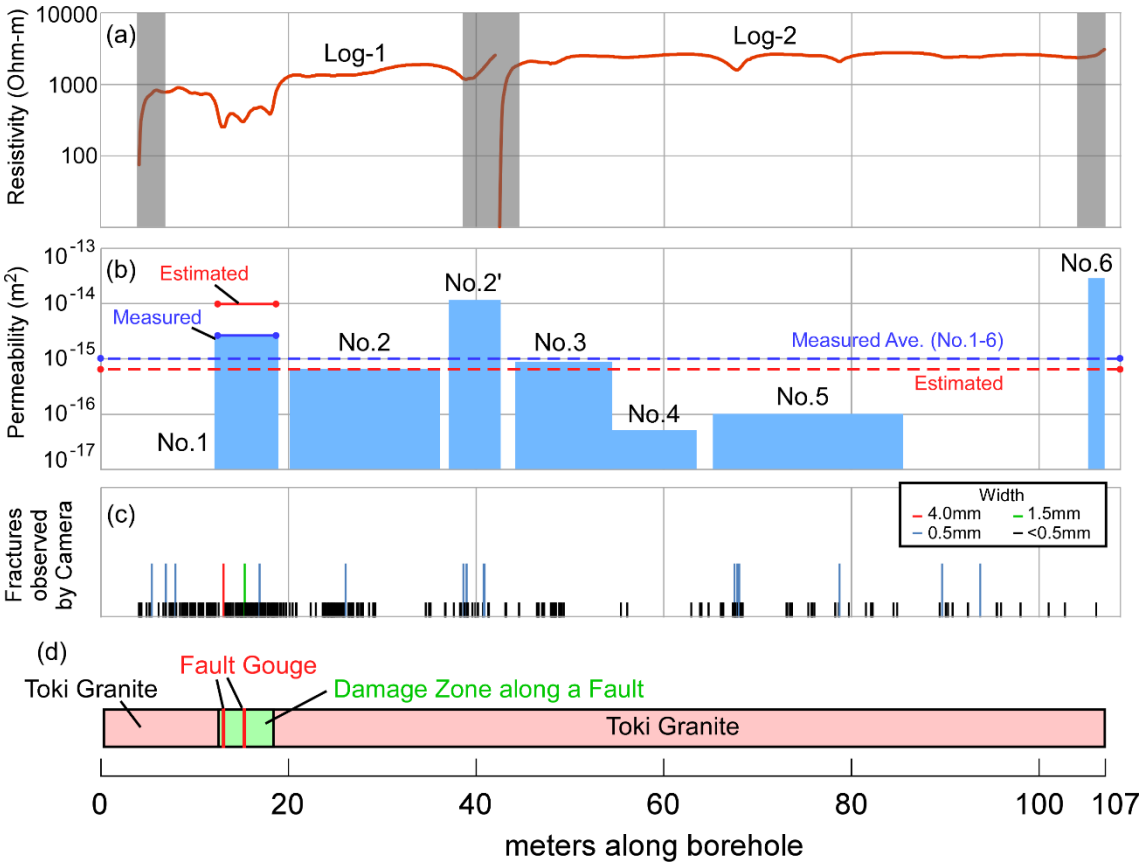

Fig. 2.4. Summary of observed data along the horizontal borehole 12MI33 with (a) in situ resistivity data, (b) measured permeability by hydraulic tests at the six borehole sections (Nos. 1-6), (c) distribution of fractures observed clearly by the borehole televiewer, and (d) geological settings based on descriptions of core samples. Two electric loggings (Log-1 and Log-2) were implemented. The gray hatched zones were excluded because of abnormal values in (a). Blue dashed and solid bars in (b) represent the average of all data in the six sections and in-situ measured value in the No. 1 section. Red dashed and solid bars are the permeabilities estimated using the proposed method, as described in section 4. The observed data is from (Tsuyuguchi et al., 2014).

Table 2.1. Observed fracture orientation and density for the DFN modeling. Cases 1 and 2 respectively denote the average fracture parameters along borehole 12MI33 and parameters only for the No. 1 section in Fig. 2.4. The dip direction is measured in a clockwise fashion from true north.

Case 1(Avg.)	dip (°)	dip direction (°)	κ	P_{10} (m^{-1})
set-1	82.0	28.0	7.0	0.17
Case 2 (No.1)	dip (°)	dip direction (°)	κ	P_{10} (m^{-1})
set-1	62.4	52.2	5.0	0.44

These fracture parameters are used in our DFN modeling, described later. Two cases, (Table 2.1) are conducted: i) averaged values along borehole 12MI33, and ii) averaged ones only in the section No.1 of 12MI33. Each fracture location is not accurately modeled. Instead, the fracture distribution shown in Table 2.1 is used in the modeling. Fracture aperture is a critical parameter for which an adjustment is required in the DFN model. In this study, the authors simply assume the representative values of electrical and hydraulic apertures based on the borehole-based observations and experiments, then investigate how effective the adjustment of only one parameter (fracture length) of DFN generation is to reproduce the observed permeability. Fractures occur at all scales, and the multi-scale fractures would be involved in the modeling. The authors focus only on the open (visible) fractures having various fracture length in this study, since the distribution of fractures observed by the borehole televiewer and the geological settings show a good correspondence with the measured permeability values by hydraulic tests (especially at the section No. 1 and the surroundings; Fig. 2.4). Here, the 17 open fractures (Fig. 2.4c) were used for $\bar{\rho}$ by assuming that all electrical apertures are equal to the geometrical aperture 0.5 mm irrespective of the fracture length. Another important parameter is hydraulic aperture b, which differs from the geometry aperture but which can be estimated using an empirical equation derived from laboratory tests and assuming a proportional relation to the fracture radius, as described in an earlier report (Kalinina et al., 2018):

$$b = 1.16 \times 10^{-5} r \tag{2.15}$$

An averaged aperture weighted by fracture lengths in each grid-block is used to avoid overestimation of effective permeability by using Equation (2.15) directly.

Physical properties of rock

The in-situ resistivity data by electrical logging using short normal with 25 cm electrode separation was 250–2770 $\Omega \cdot \mathrm{m}$ along 12MI33 (Iwatsuki et al., 2019), as presented in Fig. 2.4a. One remarkable feature is the large decrease of resistivity in the fault damage zone (the No.1 section), with average 600 $\Omega \cdot \mathrm{m}$ versus the overall average of 2000 $\Omega \cdot \mathrm{m}$. It is noteworthy that the erroneous resistivities in the hatched zones (Fig. 2.4b) were excluded from analyses. To assign the resistivity of the saturated fracture, the resistivity of the water samples from 12MI33 was measured as 7.0 $\Omega \cdot \mathrm{m}$ (Table 2.2). The matrix resistivity without open fractures was assumed as 5000 $\Omega \cdot \mathrm{m}$ based on the maximum resistivity measured at intact rock masses on the GL-500 m gallery (Fig. 2.3). Other rock properties obtained using geophysical logging were 2.56 g/cm^3 average density (2.36 g/cm^3 around the No. 1 section), 2% or less porosity, and 5.5–5.7 km/s P-wave velocity (Tsuyuguchi et al., 2014), which suggests intact granite along 12MI33, except for the damage zone.

The hydraulic conductivities K_{ij} (m/s) obtained through the hydraulic tests are portrayed

in Fig. 2.4c, which were converted into permeability k_{ij} (m^2) by:

$$K_{ij} = \frac{\rho_w g}{\mu} k_{ij} \tag{2.16}$$

where μ represents fluid viscosity (1.0×10^{-3} $Pa \cdot s$), ρ_w signifies water density (1000 kg/m^3), and g stands for gravitational acceleration (9.8 m/s^2). A value 1.0×10^{-15} m^2 was used as a reference field-scale permeability, similarly to a study reported by Iwatsuki et al. (2019).

Model setup

Two cases of fracture parameters were prepared for DFN modeling to examine permeable fractures specifically: Case 1 – averages of all fracture data; and Case 2 – averages of only fracture data in the highly permeable section of No. 1 (Table 2.1). The No. 2 section was around the junction of two logging tests: Log-1 and Log-2 (Fig. 2.4a). Furthermore, the No. 6 section had a high flow rate of groundwater observed at the end of drilling (Tsuyuguchi et al., 2014). Both were permeable, but they were excluded because of a lack of resistivity data. Details of all results are explained below for Case 1, but only main results are shown for Case 2.

Parameter values used for the DFN modeling and crack tensor are presented in Table 2.2. To ensure a numerical converge in calculating $\bar{\rho}$, $\sigma_f \omega$ was site-dependent adjusted before a formal analysis. $\sigma_f \omega$ was multiplied by an optimal correction factor of 28. The correction factor which was necessary for analysis showed that σ_f or ω shown in Table 2.2 was far from real in-situ field data. Either σ_f or ω should be increased. Cubic grid blocks of 5 × 5 × 5 with each side length (REV size) of 20 m were set in the computational domain. First, several tests were performed to decide the range of *a*. When *a* was smaller than 2.5 or larger than 3.5, the estimated electrical resistivity of a DFN model differed greatly from the in-situ measured electrical resistivity. Consequently, the optimum value of *a* was selected as 2.5–3.5 through matching between the calculated $\bar{\rho}$ and the resistivity data.

Three axes of the calculation domain were set along E–W (*x*) and N–S (*y*). The vertical (*z*) and the domain were divided into several grid blocks of cubic shape by assuming that REV was smaller than this grid-block. The authors ascertained the REV size of fractured rock mass following the method reported by Min et al. (2004). After 100 large 'parent' DFN models of 100 m × 100 m × 100 m were generated, each model was divided into grid blocks with 5–25 m side length. The average of $\bar{k}$ values of all grid blocks changed with increasing unit grid-block size. A suitable REV size was inferred when the change of $\bar{k}$ average became gradual.

Table 2.2. Parameter values used for DFN modeling and crack tensor.

Matrix resistivity	5000 $\Omega \cdot m$
Fracture resistivity	7 $\Omega \cdot m$
Field-scale resistivity	Case 1 (Avg.): 2000 $\Omega \cdot m$
	Case 2 (No. 1): 600 $\Omega \cdot m$
Characteristic size	100 m
Minimum fracture length	0.5 m
Maximum fracture length	100.0 m
Side length of each grid block size	20 m as explained in 4.1.
Scaling exponent	2.5 to 3.5
Electrical aperture	5.0×10^{-4} m
Hydraulic aperture	Application of Eq. 2.15
Correction factor of Eq. 2.13	28

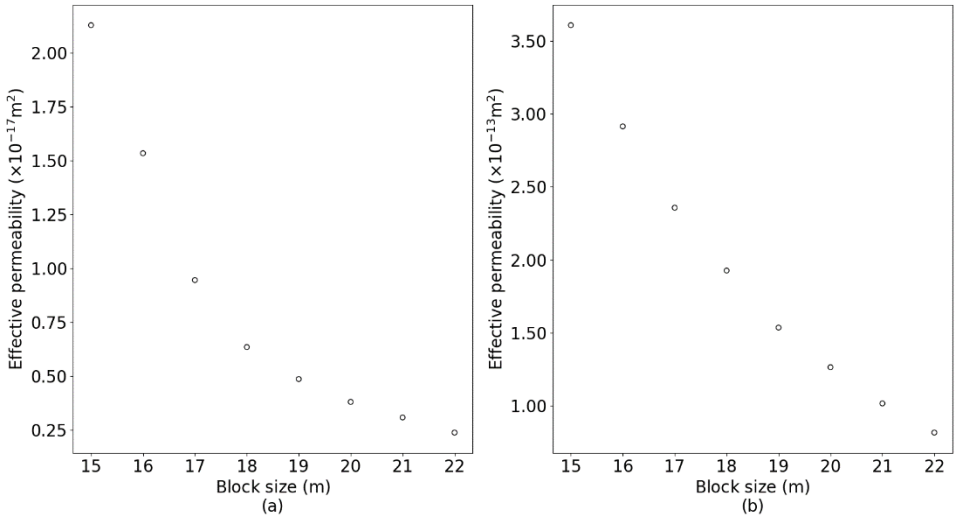

Fig. 2.5. Change in the average of effective permeability of grid blocks in a computational domain with 100 m characteristic side length. DFN models were constructed using the parameters defined in Tables 2.1 and 2.2 with scaling exponents *a* (a) 3.5 and (b) 2.5.

2.4 Results

REV size

The $\bar{k}$ averages of grid blocks decreased concomitantly with increasing side block length using the maximum (3.5) and minimum (2.5) *a* value (Fig. 2.5). Both changes became gradual at a certain side length (e.g., 20 m) or greater side length. Based on Fig. 2.5, a larger side length

would be preferable to estimate the effective permeability. However, in the crack tensor theory, the rock masses are treated as homogeneous media (Oda, 1985). The fracture distribution in the large parent DFN model is stochastically generated, and not always statistically homogeneous. That is a reason to establish the REV, in which the characteristic of fractures assumed to be constant. In addition, considering the statistical stability, a large number of grid blocks (e.g., > 100) is preferable for the estimation of the $\bar{k}$ average of a DFN model.

Determination of optimal block size of a REV is a subjective task, depending the stability of estimated physical parameters and its spatial resolution (e.g., Min et al, 2004). Although several methods to determine the size of REV are proposed (Min et al., 2004; Ni et al., 2017; Ma et al., 2020), a simple way is applied here; the REV size corresponds to the minimum size beyond which the averaged physical value is stable (Pouya and Ghoreychi, 2001; Chalhoub and Pouya, 2008). The corner of curve in Fig. 2.5 is not sharp, so several different values represent reasonable block sizes; 19-22 m approximately. More quantitatively, the relative difference of effective permeability between two neighboring block sizes (e.g., 15 & 16 m, 16 & 17 m, and so on) is calculated. It keeps around 5%, and does not change much beyond the block size of 20 m. The authors consider the relative difference with 5% can be accepted as small. In addition, the large 'parent' DFN model has a side length of 100 m, so that the REV size is basically limited to its divisors: 10, 20, 25, or 50 m. Therefore, the REV size was determined as 20 m in the later results. Another case under the REV size of 25 m will be also discussed later.

Optimum DFN model

The scaling exponent *a* has a great effect on the fracture length and density, and also on the physical parameters of the rock mass (effective resistivity and permeability). The average fracture length in the DFN model for Case 1 decreased gradually with *a* (Fig. 2.6). It is easily inferred from the definition of *a* (see equation (2.3)). The number of fractures per unit volume in the computational domain, P_{30} (m^{-3}), increased with increasing *a* value (Fig. 2.7). In this study, the constant fracture density is assumed in the DFN modeling; however, it is the number of fractures per unit length P_{10} (m^{-1}) shown in Table 2.1. The longer fractures contribute to P_{10} values as well as smaller fractures, but less to P_{30} values. The averages of $\bar{\rho}$ and $\bar{k}$ values of 125 grid blocks also changed gradually with increasing *a* value (Fig. 2.8). As an example of the constructed DFN model, the model with the shortest average fracture length by $a = 3.5$ is presented in Fig. 2.9a, for which the average $\bar{\rho}$ (3094 $\Omega \cdot$ m) is larger than the field-scale resistivity, 2000 $\Omega \cdot$ m(Table 2.2). The resistivity difference is much larger than the matching criterion in Fig. 2.2. Therefore, the DFN model is unsuitable. By repeating the change of *a* value, the resistivity difference fell into the criterion at $a = 3.0$. The optimum DFN model was obtained as presented in Fig. 2.9b. Regarding Case 2, optimum *a* was found as 2.8 for average fracture length assigned as 1.10 m.

Sensitivity of fracture distribution to a was demonstrated using a vertical cross-section in the middle of y axis (y = 50 m) by comparing two DFN models with a = 3.5 and 3.0 for Case 1 (Fig. 2.10). The respective average fracture lengths are 0.83 m (a = 3.5) and 0.99 m (a = 3.5). Comparison confirms the presence of many more long fractures in the model a = 3.0, which almost matched the calculated $\bar{\rho}$ almost with the measured resistivity. Results show that the constraint of resistivity data obtained from geophysical logging is valid for construction of a plausible DFN model.

Effective electrical resistivity

The ρ_{ij} values along the x, y, and z axes of each grid block in the DFN model with a = 3.0 are presented in Fig. 2.11. The resistivity along each direction differs because of anisotropy of the DFN model (Fig. 2.9b). However, $\bar{\rho}$ was 2064 $\Omega \cdot$ m, which is around the field-scale resistivity of 2000 $\Omega \cdot$ m. This similarity also supports the suitability of the DFN model.

Effective permeability

The diagonal permeability components, k_{xx}, k_{yy}, and k_{zz} of each grid block in the DFN model with a = 3.0 and their planar distributions at the vertical cross-section as the same location with Fig. 2.10 are depicted respectively in Figs. 2.12 and 2.13. Grid blocks with high permeabilities in Fig. 2.12 correspond to small resistivities in Fig. 2.11. Averages of all k_{xx}, k_{yy}, and k_{zz} values and the resultant $\bar{k}$ are compared with the hydraulic test data in Table 2.3. Because the fractures were steep, as shown by the average dip, 82° (Table 2.1), a feature by which k_{zz} (related to vertical flow) and k_{yy} (related to horizontal flow) are, respectively, the maximum and minimum, is reasonable. The second largest value of k_{xx} is related to the dominant strike of fractures, N62°W, which is perpendicular to the main dip direction, 28° (Table 2.1). Comparison of Figs. 2.10 and 2.12 reveals that the k_{zz} values tend to increase in zones where long fractures are concentrated.

For the measured $\bar{k}$ = 1.0 × 10^{-15} m^2, the value of $\bar{k}$ calculated using the proposed method was about its half, 5.30 × 10^{-16} m^2. The calculated $\bar{k}$ in Case 2, 1.18 × 10^{-14} m^2, was about four times larger than the measured $\bar{k}$ = 2.67 × 10^{-15} m^2(Table 2.3). Despite these discrepancies, the differences are smaller than one order in both cases. Therefore, the proposed method can be regarded as effective.

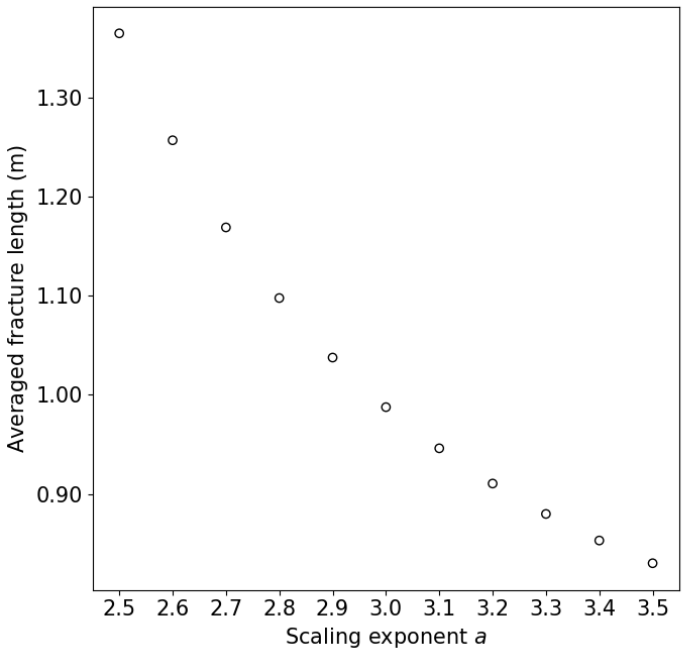

Fig. 2.6. Relation between average facture length and scaling exponent a between 2.5 and 3.5 for Case 1.

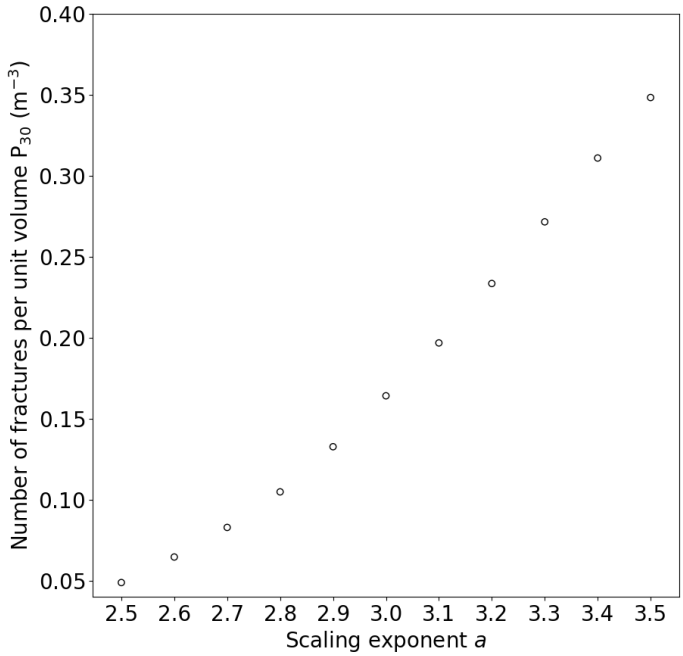

Fig. 2.7. Relation between the number of fractures per unit volume P30 and scaling exponent a

between 2.5 and 3.5 for Case 1.

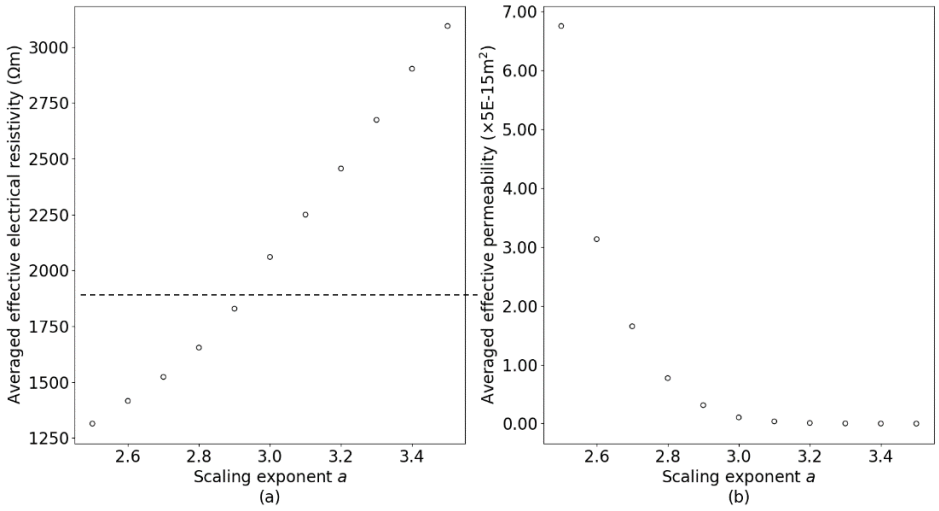

Fig. 2.8. Relationship between scaling exponent a (= 2.5–3.5) and (a) average of effective electrical resistivity and (b) effective permeability of 125 grid blocks, respectively for Case 1. The dashed line in (a) shows the in-situ measured resistivity value.

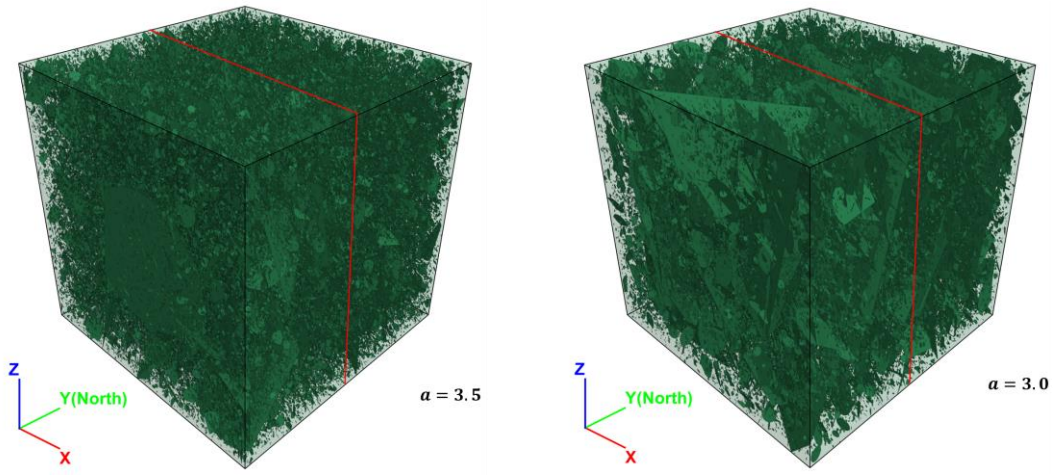

(a) (b)

Fig. 2.9. DFN models constructed for Case 1 with a = 3.5 (a) and the optimum value, 3.0 (b) in the calculation domain of 100 m × 100 m × 100 m and the location of cross-sections in Fig. 2.10 by red lines. The (a) model does not satisfy the convergence criterion presented in Fig. 2.2. Finally, the (b) model is used for subsequent examinations and discussions. The x, y, and z axes are respectively oriented eastward, northward, and upward vertical.

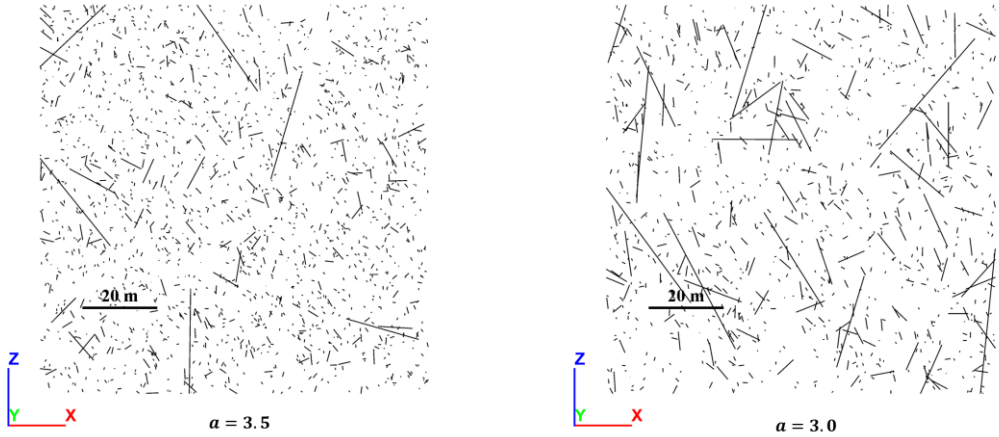

(a) (b)

Fig. 2.10. Vertical cross-sections of the DFN models in Fig. 2.9, constructed with a = 3.5 (a) and 3.0 (b), at the middle of the y axis (y = 50 m).

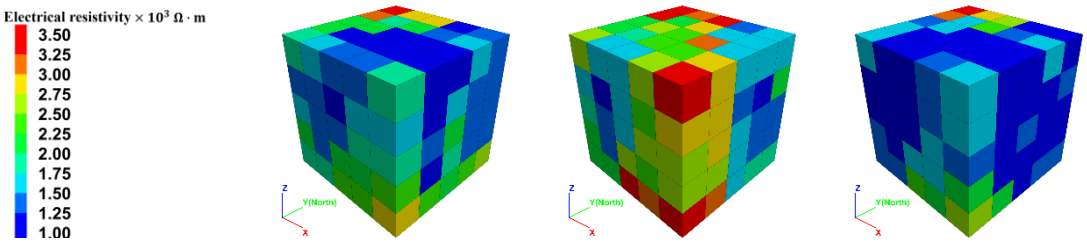

(a) (b) (c)

Fig. 2.11. Resistivities of diagonal components, (a) ρ_{xx}, (b) ρ_{yy}, and (c) ρ_{zz} of respective DFN model grid blocks constructed with a = 3.0 for Case 1 in Fig. 2.9b. The side length of each grid block is 20 m. The calculation domain size is shown in Fig. 2.9.

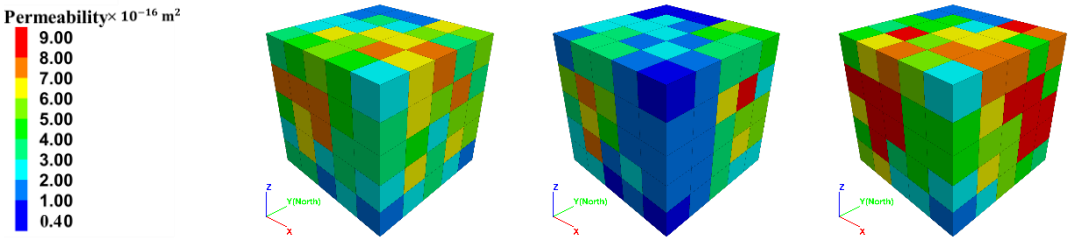

(a) (b) (c)

Fig. 2.12. Permeabilities of diagonal components, (a) k_{xx}, (b) k_{yy}, and (c) k_{zz} of each grid blocks in the DFN model constructed with a = 3.0 for Case 1 in Fig. 2.9b. The domain size is presented in Fig. 2.11.

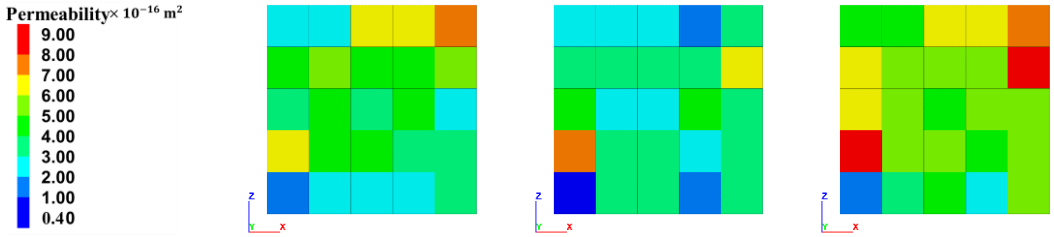

(a) (b) (c)

Fig. 2.13. Vertical cross-sections of (a) k_{xx}, (b) k_{yy}, and (c) k_{zz} of grid blocks in the DFN model constructed with a = 3.0 for Case 1 in Fig. 2.12. The cross-section location is portrayed in Fig. 2.10.

Table 2.3. Comparison between calculated diagonal permeabilities through the constructed DFN model in Fig. 2.9b and permeability by in-situ hydraulic testing

Case 1 (Avg.)	Calculated effective permeability (m^2)	In-situ measured permeability (m^2)
k_{xx}	5.91×10^{-16}	Unmeasured
k_{yy}	3.15×10^{-16}	Unmeasured
k_{zz}	6.84×10^{-16}	Unmeasured
$\frac{1}{3}(k_{xx}+k_{yy}+k_{zz})$	5.30×10^{-16}	1.0×10^{-15}

Case 2 (No.1)	Calculated effective permeability (m^2)	In-situ measured permeability (m^2)
k_{xx}	1.03×10^{-15}	Unmeasured
k_{yy}	1.22×10^{-14}	Unmeasured
k_{zz}	1.28×10^{-14}	Unmeasured
$\frac{1}{3}(k_{xx}+k_{yy}+k_{zz})$	1.18×10^{-14}	2.67×10^{-15}

2.5 Discussion

In this study, the difference between the calculated effective permeability and in-situ measured permeability is less than one order for each case. The authors believe that our scheme of permeability estimation is effective; however, minor difference still remains. One possible

cause of the difference is the presence of clay minerals as filling fractures: chloritization was observed in the fault gouge in the core samples from damage zone from the No. 1 section (Fig. 2.4; Tsuyuguchi et al., 2014). Clay minerals in saturated rocks generally decrease the resistivity and permeability. If clay minerals are not taken into consideration, the lower the resistivity, the longer the fracture length (which may result in the over-estimation of permeability). Accordingly, the predicted $\bar{k}$ was slightly higher than the actual value at the No. 1 section (Case 2 in Table 2.3; Fig. 2.4b). Another possible cause is that a single-borehole hydraulic test was unable to measure anisotropic permeabilities of fractured rock mass: the in-situ measured permeability is always an average behavior, irrespective of direction. Fractures perpendicular to the borehole direction tend to appear much more than fractures parallel to the direction. This directional bias of fractures might induce a phenomenon by which the measured permeability differs from the intrinsic permeability of the fractured rock mass.

This study optimized only one unknown parameter *a*, scaling exponent, in the DFN model. Other parameters such as fracture location and aperture are also necessarily constrained to construct a more accurate DFN model using data of various types. A multi-parameter optimization scheme is expected to be effective for the constraint. Then, multiple DFN models with equal accuracy might be built. Geophysical logging tool (Fig. 2.1) obtains various physical parameters along a borehole (e.g., seismic velocity, density, porosity with resistivity), and will be helpful for the multi-parameter optimization. Several other approaches can be also used to reduce uncertainty of DFN models. For example, microseismic data together with geologic data were used to constrain fracture locations to decrease uncertainty of the DFN models (Sun et al., 2016). In this method, fracture length was assumed to follow a power-law distribution without any constraint and only fracture locations were constrained by considering that microseismic events were located at or close to fractures. Instead of constraining fracture locations of a DFN model, the power law parameters in DFN models were calibrated using in-situ hydrogeological data (Follin et al., 2014) with construction of initial DFN model using the geological data obtained from the boreholes. The frequency of connected open fractures observed in the hydraulic pumping tests was used to adjust the size distributions of fractures. Those two approaches can be implemented to reduce the uncertainties of DFN models by using available datasets (e.g., geophysical logging and hydraulic tests along a test borehole), then the optimized model parameters can be applied to permeability prediction along other boreholes. Even with our limited parameter optimization, the estimated permeability along borehole 12MI33 is similar to the observed ones with moderately small discrepancies (less than one order of magnitude; Cases 1 and 2 in Table 2.3). As mentioned, electrical resistivity was selected by this study to constrain a DFN model because of its sensitivity to fractures. Geophysical surveys for in-situ electrical resistivity data are common in engineering practice (e.g., tunnel construction). Consequently, using electrical resistivity data as a constraint

of building a DFN model is feasible, and a permeability of fractured rock is obtainable.

Several issues remain in relation our proposed method. The effective permeability continues to decrease over the side length of the DFN model, 20 m, although the rate of decrease becomes low as shown in Fig. 2.5. This phenomenon may result from the relation between hydraulic aperture and the fracture length. Effective permeability becomes constant over a certain block size if the hydraulic aperture is constant and does not vary with the fracture length.

The authors used effective permeability in this study to represent fractured rock permeability. Using equivalent permeability is also possible. This equivalent permeability does not necessarily require a REV size of DFN model, which seems more flexible than the effective permeability. However, equivalent permeability is changeable with the grid-block size. Accordingly, several equivalent permeabilities might be calculated under a condition for determining a single effective permeability, which results in increasing uncertainty of permeability estimation. Although more examination of the difference between effective and equivalent permeabilities is necessary, effective permeability might be suitable for a comparison with the in-situ measured permeability.

2.6 Conclusion

This study was conducted using resistivity logging data obtained in pilot drilling for tunnel excavation as a constraint of the distribution, thereby overcoming a persistent difficulty of DFN modeling: uncertainty in fracture length distribution. Effectiveness of using the electrical resistivity and the symmetric self-consistent method were proved respectively to constrain fracture lengths and calculate electrical resistivity of a DFN model. Through this application, an optimized scaling exponent for the fracture distribution was determined, which enabled derivation of a suitable effective permeability of the *x*, *y*, and *z* axes and their average using an improved Oda's crack tensor theory.

To validate the proposed method, we conducted two case studies examining fracture and resistivity data obtained from a borehole at 500 m depth at the Mizunami Underground Research Laboratory, central Japan. The data were from the Toki granite. The difference between the average effective permeability using our proposed method and the averaged permeability measured by hydraulic tests was less than one order. For Case 1, which targeted the whole case study area with all available data, a DFN model with scaling exponent a = 3.5 was unsuitable, because its $\bar{\rho}$ was larger than the in-situ measured resistivity. By changing a to 3.0, the optimal DFN model was constructed with corresponding average effective permeability $\bar{k} = 5.30 \times 10^{-16}$ m^2, which is about half of in-situ measured permeability 1.0×10^{-15} m^2. For Case 2, which was limited to the fault damage zone, a was set as 2.8. The calculated $\bar{k}$ was 1.18×10^{-14} m^2, which was about four times greater than the in-situ measured permeability of 2.67×10^{-15} m^2. Based on results of these two case studies, we conclude that the constrained DFN modeling

approach using in-situ resistivity data can avoid constructing unrealistic DFN models with too many short fractures.

Improvement of the proposed method, our next step, can be accomplished by changing the Oda's crack tensor theory and the symmetric self-consistent method, which are empirical methods, to more accurate numerically based methods. Moreover, this study examined only the effects of *a* on the DFN modeling, but the modeling accuracy depends also on other parameters such as the minimum and maximum fracture lengths, fracture aperture, fracture location together with clay mineral contents. Deep consideration of all control parameters for DFN modeling and their sensitivities to the accuracy of DFN models will be achieved by multi-physical data, and are important subjects for future work.

References

Barenblatt, G.., Zheltov, I.., Kochina, I.., 1960. Basic concepts in the theory of seepage of homogeneous liquids in fissured rocks [strata]. J. Appl. Math. Mech. 24, 1286–1303. https://doi.org/10.1016/0021-8928(60)90107-6

Chalhoub, M., Pouya, A., 2008. Numerical homogenization of a fractured rock mass: a geometrical approach to determine the mechanical representative elementary volume. Electron J Geotech Eng, 13, 1-12.

Dershowitz, W.S., Einstein, H.H., 1988. Characterizing rock joint geometry with joint system models. Rock Mech. Rock Eng. 21, 21–51. https://doi.org/10.1007/BF01019674

Dershowitz, W.S., Fidelibus, C., 1999. Derivation of equivalent pipe network analogues for three-dimensional discrete fracture networks by the boundary element method. Water Resour. Res. 35, 2685–2691. https://doi.org/10.1029/1999WR900118

Dorn, C., Linde, N., Borgne, T. Le, Bour, O., de Dreuzy, J.-R., 2013. Conditioning of stochastic 3-D fracture networks to hydrological and geophysical data. Adv. Water Resour. 62, 79–89. https://doi.org/10.1016/J.ADVWATRES.2013.10.005

Follin, S., Hartley, L., Rhén, I., Jackson, P., Joyce, S., Roberts, D., Swift, B., 2014. A methodology to constrain the parameters of a hydrogeological discrete fracture network model for sparsely fractured crystalline rock, exemplified by data from the proposed high-level nuclear waste repository site at Forsmark, Sweden. Hydrogeol. J. 22, 313–331. https://doi.org/10.1007/s10040-013-1080-2

Hadgu, T., Karra, S., Kalinina, E., Makedonska, N., Hyman, J.D., Klise, K., Viswanathan, H.S., Wang, Y., 2017. A comparative study of discrete fracture network and equivalent continuum models for simulating flow and transport in the far field of a hypothetical nuclear waste repository in crystalline host rock. J. Hydrol. 553, 59–70. https://doi.org/10.1016/j.jhydrol.2017.07.046

Hamm, S.Y., Kim, M.S., Cheong, J.Y., Kim, J.Y., Son, M., Kim, T.W., 2007. Relationship between hydraulic conductivity and fracture properties estimated from packer tests and borehole data in a

fractured granite. Eng. Geol. 92, 73–87. https://doi.org/10.1016/j.enggeo.2007.03.010

Iwatsuki, T., Onoe, H., Ishibashi, M., 2019. DECOVALEX-2019 Task C; GREET Intermediate report [WWW Document]. URL https://jopss.jaea.go.jp/search/servlet/search?5064318&language=1 (accessed 3.23.20).

Japan Nuclear Cycle Development Institute, 2002. Master Plan of the Mizunami Underground Research Laboratory Project, JNC-TN7410 2003-001, 153 pp.

Kalinina, E., Hadgu, T., Wang, Y., Ozaki, Y., Iwatsuki, T., 2018. Development and Validation of a Fracture Model for the Granite Rocks at Mizunami Underground Research Laboratory Japan. Proceeding of 2nd International Discrete Fracture Network Engineering Conference, DFNE18-435, American Rock Mechanics Association.

Karimi-Fard, M., Durlofsky, L.J., Aziz, K., 2003. An Efficient Discrete Fracture Model Applicable for General Purpose Reservoir Simulators, in: SPE Reservoir Simulation Symposium. Society of Petroleum Engineers. https://doi.org/10.2118/79699-MS

Koike, K., Kubo, T., Liu, C., Masoud, A., Amano, K., Kurihara, A., Matsuoka, T., Lanyon, B., 2015. 3D geostatistical modeling of fracture system in a granitic massif to characterize hydraulic properties and fracture distribution. Tectonophysics 660, 1–16. https://doi.org/10.1016/J.TECTO.2015.06.008

Koike, K., Liu, C., Sanga, T., 2012. Incorporation of fracture directions into 3D geostatistical methods for a rock fracture system. Environ. Earth Sci. 66, 1403–1414. https://doi.org/10.1007/s12665-011-1350-z

Kubo, T., Matsuda, N., Kashiwaya, K., Koike, K., Ishibashi, M., Tsuruta, T., Matsuoka, T., Sasao, E., Lanyon, G.W., 2019. Characterizing the permeability of drillhole core samples of Toki granite, Central Japan to identify factors influencing rock-matrix permeability. Eng. Geol. 259, 105163. https://doi.org/10.1016/J.ENGGEO.2019.105163

Lei, Q., Latham, J.-P., Xiang, J., Tsang, C.-F., Lang, P., Guo, L., 2014. Effects of geomechanical changes on the validity of a discrete fracture network representation of a realistic two-dimensional fractured rock. Int. J. Rock Mech. Min. Sci. 70, 507–523. https://doi.org/10.1016/J.IJRMMS.2014.06.001

Lei, Q., Latham, J.-P., Tsang, C.-F., 2017a. The use of discrete fracture networks for modelling coupled geomechanical and hydrological behaviour of fractured rocks. Comput. Geotech. 85, 151–176. https://doi.org/10.1016/J.COMPGEO.2016.12.024

Lei, Q., Latham, J.P., Tsang, C.F., 2017b. The use of discrete fracture networks for modelling coupled geomechanical and hydrological behaviour of fractured rocks. Comput. Geotech. 85, 151–176. https://doi.org/10.1016/j.compgeo.2016.12.024

Leung, C.T.O., Hoch, A.R., Zimmerman, R.W., 2012. Comparison of discrete fracture network and equivalent continuum simulations of fluid flow through two-dimensional fracture networks for the DECOVALEX–2011 project. Mineral. Mag. 76, 3179–3190. https://doi.org/10.1180/minmag.2012.076.8.31

Li, J.H., Zhang, L.M., Wang, Y., Fredlund, D.G., 2009. Permeability tensor and representative elementary volume of saturated cracked soil. Can. Geotech. J. 46, 928–942. https://doi.org/10.1139/T09-037

Liu, C., Kubo, T., Lu, L., Koike, K., Zhu, W., 2019. Spatial Simulation and Characterization of Three-Dimensional Fractures in Gejiu tin District, Southwest China, Using GEOFRAC. Nat. Resour. Res. 28, 99–108. https://doi.org/10.1007/s11053-018-9381-8

Ma, K., Wang, L., Peng, Y., Long, L., Wang, S., Chen, T., 2020. Permeability characteristics of fractured rock mass: a case study of the Dongjiahe coal mine. Geomatics, Natural Hazards and Risk, 11, 1724-1742. https://doi.org/10.1080/19475705.2020.1811403

Mak, S.W., 2014. Assessing fracture network connectivity of prefeasibility-level high temperature geothermal projects using discrete fracture network modelling. https://doi.org/10.14288/1.0167612

Min, K.-B., Jing, L., Stephansson, O., 2004. Determining the equivalent permeability tensor for fractured rock masses using a stochastic REV approach: Method and application to the field data from Sellafield, UK. Hydrogeol. J. 12, 497–510. https://doi.org/10.1007/s10040-004-0331-7

Mourzenko, V. V., Thovert, J.F., Adler, P.M., 2011. Permeability of isotropic and anisotropic fracture networks, from the percolation threshold to very large densities. Phys. Rev. E - Stat. Nonlinear, Soft Matter Phys. 84, 036307. https://doi.org/10.1103/PhysRevE.84.036307

Ni, P., Wang, S., Wang, C., Zhang, S., 2017. Estimation of REV size for fractured rock mass based on damage coefficient. Rock Mechanics and Rock Engineering, 50, 555-570. https://doi.org/10.1007/s00603-016-1122-x

Oda, M., 1986. An equivalent continuum model for coupled stress and fluid flow analysis in jointed rock masses. Water Resour. Res. 22, 1845–1856. https://doi.org/10.1029/WR022i013p01845

Pouya, A., Ghoreychi, M., 2001. Determination of rock mass strength properties by homogenization. International Journal for Numerical and Analytical Methods in Geomechanics, 25, 1285-1303. https://doi.org/10.1002/nag.176

Pruess, K., Narasimhan, T., 1982. A practical method for modeling fluid and heat flow in fractured porous media. in: 6th SPE symposium on Reservoir Simulation. Society of Petroleum Engineers. https://escholarship.org/content/qt0km6n7qv/qt0km6n7qv.pdf (accessed 3.23.20).

Pruess, K., Oldenburg, C.M., Moridis, G.J., 1999. TOUGH2 User's Guide Version 2, Lawrence Berkeley National Laboratory, 197pp.

Renard, P., De Marsily, G., 1997. Calculating equivalent permeability: A review. Adv. Water Resour. 20, 253-278. https://doi.org/10.1016/s0309-1708(96)00050-4

Rutqvist, J., Leung, C., Hoch, A., Wang, Y., Wang, Z., 2013. Linked multicontinuum and crack tensor approach for modeling of coupled geomechanics, fluid flow and transport in fractured rock. J. Rock Mech. Geotech. Eng. 5, 18–31. https://doi.org/10.1016/j.jrmge.2012.08.001

Sævik, P.N., Berre, I., Jakobsen, M., Lien, M., 2013. A 3D Computational Study of Effective Medium Methods Applied to Fractured Media. Transp. Porous Media 100, 115–142.

https://doi.org/10.1007/s11242-013-0208-0

Sævik, P.N., Jakobsen, M., Lien, M., Berre, I., 2014. Anisotropic effective conductivity in fractured rocks by explicit effective medium methods. Geophys. Prospect. 62, 1297–1314. https://doi.org/10.1111/1365-2478.12173

Sævik, P.N., Nixon, C.W., 2017. Inclusion of Topological Measurements into Analytic Estimates of Effective Permeability in Fractured Media. Water Resour. Res. 53, 9424–9443. https://doi.org/10.1002/2017WR020943

Sandve, T.H., Berre, I., Nordbotten, J.M., 2012. An efficient multi-point flux approximation method for Discrete Fracture–Matrix simulations. J. Comput. Phys. 231, 3784–3800. https://doi.org/10.1016/J.JCP.2012.01.023

Sun, J., Gamboa, E.S., Schechter, D., Rui, Z., 2016. An integrated workflow for characterization and simulation of complex fracture networks utilizing microseismic and horizontal core data. J. Nat. Gas Sci. Eng. 34, 1347–1360. https://doi.org/10.1016/j.jngse.2016.08.024

Tsuji, M., Kobayashi, S., Mikake, S., Sato, T., Matsui, H., 2017. Post-Grouting Experiences for Reducing Groundwater Inflow at 500 m Depth of the Mizunami Underground Research Laboratory, Japan, in: Procedia Engineering. Elsevier Ltd, pp. 543–550. https://doi.org/10.1016/j.proeng.2017.05.216

Tsuyuguchi, K., Kuroiwa, H., Kawamoto, K., Yamada, N., 2014. Results of pilot borehole investigation in -500m access/research gallery-north (12MI27 and 12MI33 boreholes. JAEA-Technology 2013-044, Japan Atomic Energy Agency, 89 pp. https://doi.org/10.11484/jaea-technology-2013-044

Valera, M., Guo, Z., Kelly, P., Matz, S., Cantu, V.A., Percus, A.G., Hyman, J.D., Srinivasan, G., Viswanathan, H.S., 2017. Machine learning for graph-based representations of three-dimensional discrete fracture networks. Comput. Geosci. 22, 695–710. https://doi.org/10.1007/s10596-018-9720-1

Vogel, T., Gerke, H.H., Zhang, R., Van Genuchten, M.T., 2000. Modeling flow and transport in a two-dimensional dual-permeability system with spatially variable hydraulic properties. J. Hydrol. 238, 78–89. https://doi.org/10.1016/S0022-1694(00)00327-9

Wang, Z., Rutqvist, J., Wang, Y., Leung, C., Hoch, A., Dai, Y., 2014. The effect of stress on flow and transport in fractured rock masses using an extended multiple interacting continua method with crack tensor theory, in: Nuclear Technology. Taylor & Francis, pp. 158–168. https://doi.org/10.13182/NT13-76

Warren, J.E., Root, P.J., 1963. The Behavior of Naturally Fractured Reservoirs. Soc. Pet. Eng. J. 3, 245–255. https://doi.org/10.2118/426-PA

Williams-Stroud, S., Ozgen, C., Billingsley, R.L., 2013. Microseismicity-constrained discrete fracture network models for stimulated reservoir simulation. GEOPHYSICS 78, B37–B47. https://doi.org/10.1190/geo2011-0061.1

Wolfsberg, A., 1996. Rock Fractures and Fluid Flow: Contemporary Understanding and Applications. The

National Academies Press, 568pp. https://doi.org/10.17226/2309

Xu, C., Dowd, P., 2010. A new computer code for discrete fracture network modelling. Comput. Geosci. 36, 292–301. https://doi.org/10.1016/j.cageo.2009.05.012

Yoshida, H., Metcalfe, R., Ishibashi, M., Minami, M., 2013. Long-term stability of fracture systems and their behaviour as flow paths in uplifting granitic rocks from the Japanese orogenic field. Geofluids 13, 45–55. https://doi.org/10.1111/gfl.12008

Chapter 3

Modeling of electrical resistivity and seismic velocity changes after tunnel excavation

3.1 Introduction

An excavation damaged zone (EDZ) has been known to develop around underground excavations (e.g., tunnel, nuclear waste disposal) in the rock mass. The underground excavation which is a local stress perturbation causes the initiation and propagation of fractures. The EDZ is a disturbed zone around excavation surface in which various rock physical properties (e.g., mechanical, hydraulic, thermal, chemical) have been altered (Cai and Kaiser, 2005; Kwon et al., 2009; Tsang et al., 2005). The EDZ is mechanically unstable which has potentially negative effects of long-term tunnel stability. Also, the EDZ fractures serve as pathways of fluid flow or barriers that prevent flow across them. Therefore, the EDZ analysis is important for the design and construction of tunnels. Various methods have been developed to assess the extent of EDZ such as borehole cameras on excavation walls (e.g., Shao et al., 2008), geologic surveys (e.g., Bossart et al., 2002), hydrological methods(e.g., Aoyagi and Ishii, 2019; Bossart et al., 2002), and geophysical investigations by electrical and seismic methods (Kruschwitz and Yaramanci, 2004; Nicollin et al., 2010, 2008; Schuster et al., 2001a). It has been known that seismic velocities in the EDZ generally decrease because of the initiation and propagation of fractures (e.g., Falls and Young, 1998; Schuster et al., 2001; Spies and Eisenblätter, 2001; Wright et al., 2000).

The rock desaturation process around the tunnel excavation surface has been observed in the low permeable rock mass (e.g., Bossart et al., 2002; Charpentier et al., 2003; Maßmann et al., 2009; Matray et al., 2007; Valès et al., 2004). The desaturation process is assumed to be initialized by the saturated rock near the tunnel excavation surface interacting with the ambident air in the tunnel (Maßmann et al., 2009). The extent of the desaturation process is sensitive to the relative humidity of the ambident air. A special phenomenon that pressure increase around the tunnel excavation surface is observed in the in-situ measurement and is validated through numerical simulations (Maßmann et al., 2009). Another special phenomenon where seismic velocity and electrical resistivity increased after tunnel excavation in the Horonobe Underground Research Laboratory (URL) was observed. It may be caused by the desaturation process. A possible conceptual model which interprets such phenomenon is proposed in this chapter. The conceptual model assumes that a decrease in liquid saturation around a tunnel after excavation increases seismic velocity and electrical resistivity in the EDZ. The main cause of liquid saturation change comes from relative humidity in the tunnel.

The chapter is organized as follows. First, a possible conceptual model which interprets the

special phenomenon is presented. Then, several theories used in the hydromechanical analysis which incorporates the conceptual model are introduced. At last, a case study is carried out to validate the conceptual model.

3.2 Theories and methods

Conceptual model

The first step in the development of a formal hydromechanical model is to propose an appropriate conceptual model to explain the phenomenon observed in the Horonobe URL. Fig. 3.1 presents a possible conceptual model. After a tunnel excavation in the saturated rock mass, the EDZ is developed gradually around the excavation surface as shown in Fig. 3.1a. The fracture network which is initialized and propagated in the EDZ provides pathways of fluid flow or barriers that prevent flow across them. The fracture network also allows the ambident air in the tunnel to flow into the saturated rock near the excavation surface (Fig. 3.1b). The desaturation process is initialized and driven by the air which is sucked into the EDZ. The original saturated rock becomes unsaturated gradually. The evolution rate of the denaturation process is controlled by the relative humidity of the air in the tunnel. The desaturation process drives the capillary pressure developing in the partial saturated rock. Fig. 3.2 shows an illustration of the relationship between capillary pressure and rock saturation. The capillary pressure increases the effective stress within the EDZ. Thus, the fractures developed in the EDZ tends to close. Both the electrical resistivity and seismic velocity of the EDZ increase along with the desaturation process. The mechanism which explains such increase may come from two aspects. The electrical resistivity and seismic velocity increase as rock saturation near the excavation surface becomes smaller. Also, as the capillary pressure in the desaturated rock becomes larger, their values also increase because open fractures in the EDZ tend to close. However, through our hydromechanical analysis considering the desaturation process, we find that the later does not have a great effect on increasing the electrical resistivity and seismic velocity of the EDZ.

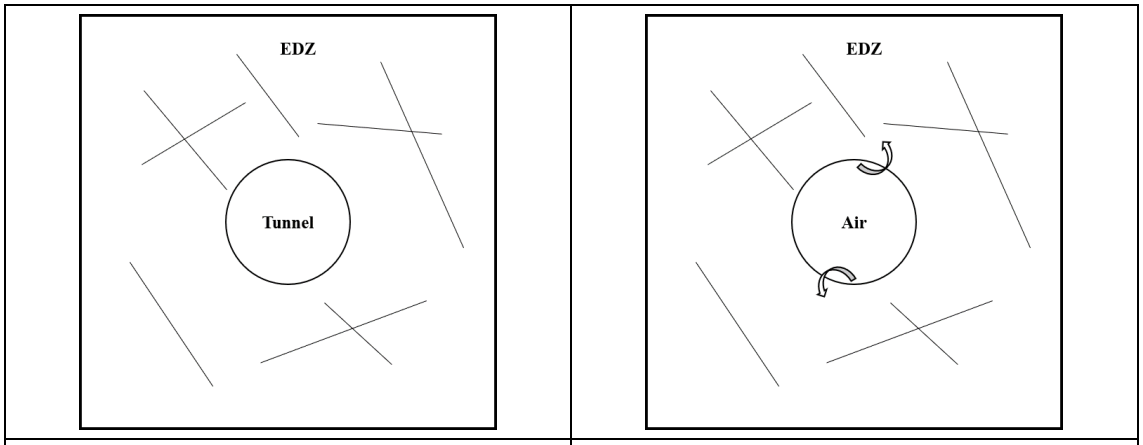

Fig. 3.1. Conceptual model for interpreting a special phenomenon where seismic velocity and electrical resistivity increased after tunnel excavation in the Horonobe Underground Research Laboratory (URL): (a) the EDZ developed around excavation surface; (b) air in the tunnel which is sucked into the EDZ.

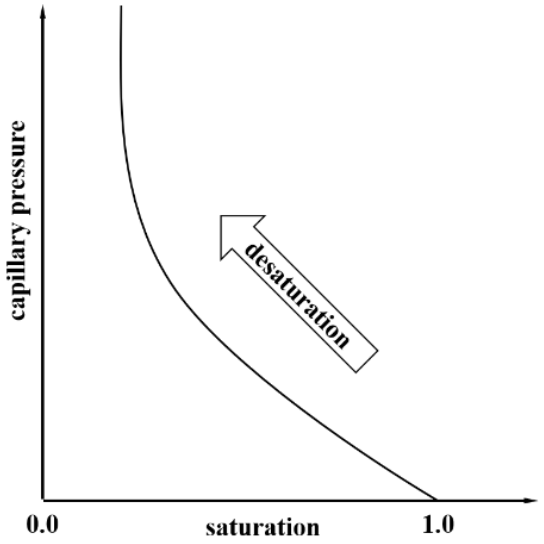

Fig. 3.2. An illustration of capillary pressure versus saturation during the desaturation process in the conceptual model.

DFN

The first step for the hydromechanical numerical analysis is to characterize the geometrical and hydromechanical properties of the EDZ which is developed around the tunnel excavation in

the rock mass. Since fractures initialize and propagate in the EDZ, the discrete fracture network (DFN) modeling approach (Baecher, 1983; Lei et al., 2017) is used to characterize the geometrical properties (e.g., locations, lengths, orientations) of the fractures. Fluid flow in fractured rock can be modeled by the MINC (Multiple Interacting Continua) which is a generalization of the classic dual porosity model (Pruess et al., 1999). Fig. 3.3 shows a conceptual diagram of the MINC model which generalizes the dual porosity model. The dual porosity assumes that fluid flow only occurs through fractures, which are described as an effective medium. Fluid may be exchanged locally between rock matrix and fractures by means of a quasi-steady-state flow driven by their pressure differences. The double porosity model is suitable to model fluid flow in fractured rock if rock matrix has small permeability and large porosity (averaged over fractured rock) while fractures have the opposite characteristics. The fracture volume fraction should be derived to use the MINC capability of TOUGH2. Thus, fracture apertures in the EDZ are necessary to calculate the fracture volume fraction. Since there is no direct information on fracture apertures through the in-situ observed data or laboratory measurements, an inverse analysis as shown in Fig. 3.4 is made to derive fracture apertures in the DFN model. An averaged in-situ measured permeability (3.5×10^{-13} m^2 in this chapter) provides a reference for estimating fracture apertures. The DFN model is optimal when the difference between the equivalent permeability and the in-situ measured permeability is relatively small by adjusting apertures.

The equivalent permeability of the DFN model is estimated from the pipe network model (Valera et al., 2018; Viswanathan et al., 2018). The pipe network model can model fluid flow through fractures neglecting flow in rock matrix. The pipe network model does not consider isolated fractures in fractured rock. A network backbone of fractures prior to modeling of fluid flow using the pipe network model is extracted from the DFN model through an heuristic algorithm that determines the edge-joint shortest path of the graph which representing the DFN model (Hyman et al., 2018). Fig. 3.5a shows the DFN model with isolating fractures. Fig. 3.5b shows the network backbone of fractures. As Fig. 3.6 shows, by applying a constant pressure drop prescribed on two opposite boundaries with left boundaries assigned impermeable, an equivalent permeability K of the DFN model in a certain direction can be back estimated using the Darcy' law defined as (Min et al., 2004; Min and Jing, 2003; Zhao et al., 2013; Zimmerman and Bodvarsson, 1996):

$$K = \frac{uQ}{A\rho_l g J} \tag{3.1}$$

where u is water viscosity, Q is total flow rates on the outlet boundary, A is the outlet boundary cross-sectional area, ρ_l is liquid density, g is the gravitational acceleration, J is the hydraulic pressure gradient.

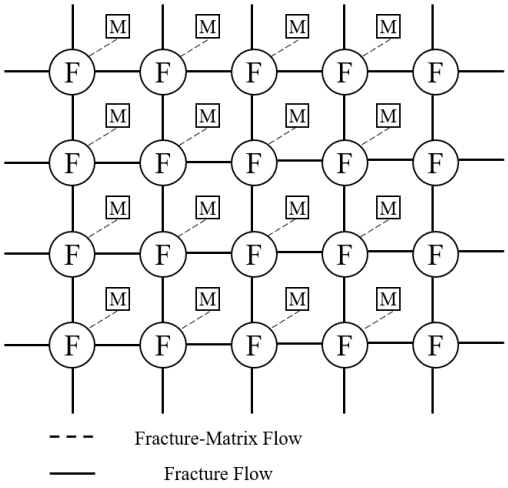

Fig. 3.3. Schematic of the MINC model. The global fluid flow in fractured rock only occurs through fractures. The fractures and rock matrix may exchange fluid locally by means of a quasi-steady-state flow driven by their pressure differences. Adapted from (Pruess, 1992).

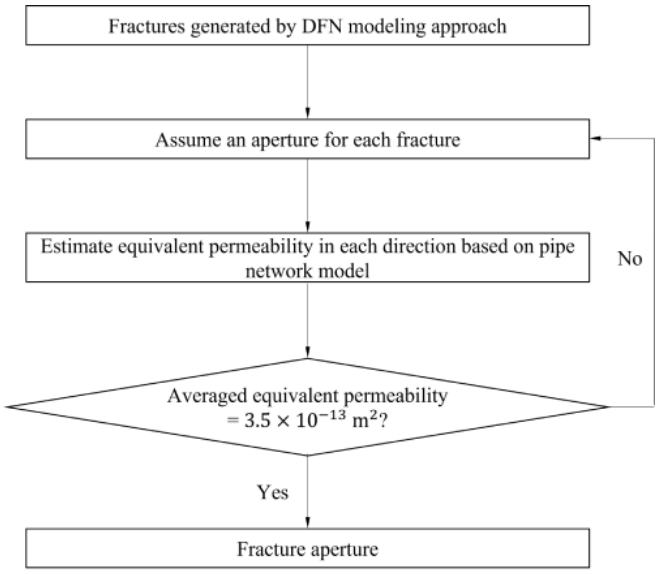

Fig. 3.4. Flowchart for deriving fracture apertures in the DFN model through comparing the equivalent permeability estimated from the pipe network model with the in-situ measured permeability.

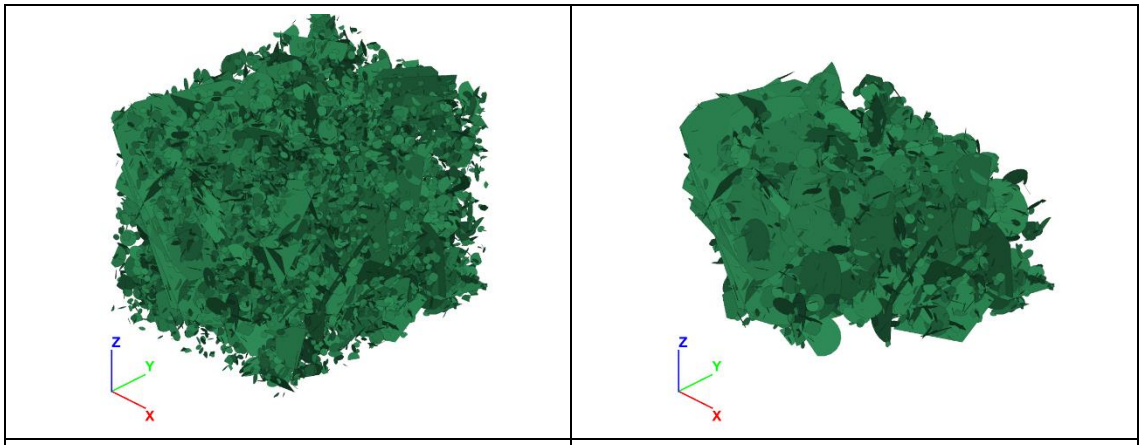

(a) (b)

Fig. 3.5. DFN models used by the pipe network model: (a) the DFN model with the isolated fractures; (b) backbone of the DFN model without the isolated fractures.

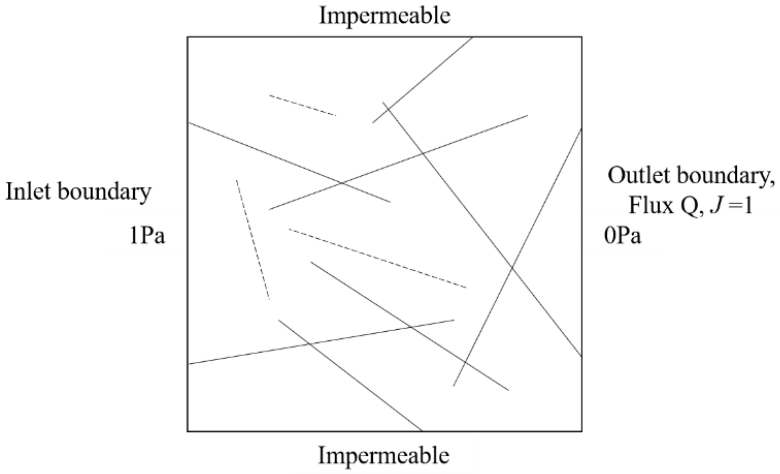

Fig. 3.6. Boundary conditions in which a constant pressure drop prescribed on two opposite boundaries with the leftover boundaries assigned impermeable for deriving an equivalent permeability in a certain direction of fractured rock.

Kelvin's equation

The relationship between an equivalent capillary pressure and the relative humidity of the ambident air in the tunnel can be estimated by Kelvin's equation (Edlefsen and Anderson, 1943; Finsterle and Pruess, 1995):

$$P_c = -\frac{\rho_l RT}{M_w}\ln(h) \tag{3.2}$$

where R is the perfect gas constant, M_w is the molecular weight of the vapor, h is the relative humidity. The desaturation process is initialized and driven by the equivalent capillary pressure which is prescribed directly at the tunnel excavation surface.

Archie equation

The Archie's law (Archie, 2003; Donaldson and Siddiqui, 1989; Mohamad and Hamada, 2017) which considers water saturation is used to estimate effective electrical resistivity of fractured rock. The Archie equation is defined as:

$$\frac{R_1}{R_0} = \left(\frac{\phi_1}{\phi_0}\right)^{-m} \left(\frac{S_{l,1}}{S_{l,0}}\right)^{-n} \tag{3.3}$$

where R_1 is the rock electrical resistivity if the fractured rock has the liquid saturation of $S_{l,1}$, and porosity of ϕ_1; R_0 is the rock electrical resistivity if the fractured rock has the liquid saturation of $S_{l,0}$, and porosity of ϕ_0. From Eq. 3.3, the variations in electrical resistivity of fracture rock come from rock porosity and saturation change.

Biot-Gassmann poroelasticity theory

Various geophysical methods (e.g., electrical and electromagnetic methods, ground penetrating radar, and seismic methods) have been developed to characterize fracture properties in the subsurface (Day-Lewis et al., 2017; Germán Rubino et al., 2013). Seismic wave which propagates through fractured rock generally attenuates. The attenuation across fractures can improve detection and characterization of fractures in rock masses. Since fractures are much smaller than seismic wavelengths, it is challenging to characterize fractures inferred from measured seismic properties (Hunziker et al., 2018). The numerical methods (e.g., Chen et al., 2019, 2018; De Basabe et al., 2016; Hunziker et al., 2018; Möller and Friederich, 2019; Zhan et al., 2017) as well as analytical effective medium models (e.g., Galvin and Gurevich, 2015; Kong et al., 2017; Song et al., 2020) have been developed to correlate seismic waves and geometrical properties of fractures.

The Biot-Gassmann theory is a widely used model to describe the relationship between seismic velocities and rock physical properties of fractured rock (Biot, 1956; Gassmann, 1951; Gutierrez et al., 2012; Lee, 2002). The bulk modulus of fractured rock $\overline{K}$ is defined as follows:

$$\overline{K} = K + \frac{\alpha^2}{\frac{\phi}{K_f} + \frac{\alpha - \phi}{K_s}} \tag{3.4}$$

where K is rock matrix elastic bulk modulus, ϕ is porosity, K_f is fluid bulk modulus, K_s is rock matrix grain bulk modulus, α is a Biot's poroelastic constant, which is defined as:

$$\alpha = 1 - \frac{K}{K_s} \tag{3.5}$$

The relationship between $\overline{K}$ and seismic velocities is described as follows:

$$\overline{K} = \rho\left(V_p^2 - \frac{4}{3}V_s^2\right) \tag{3.6}$$

$$G = \rho V_s^2 \tag{3.7}$$

where G is fractured rock shear modulus. ρ is fractured rock density. ρ is expressed as:

$$\rho = \rho_d + \phi\left[S_g\rho_g + \left(1 - S_g\right)\rho_l\right] \tag{3.8}$$

where ρ_d is dry rock density, S_g is gas saturation, ρ_g is gas density, ρ_l is liquid density.

Correction of hydraulic properties

The porosity and permeability change are calculated from two empirical equations which have been used by Gou (2016). The porosity change is related to volumetric strain ε_v as:

$$\phi = 1 - (1 - \phi_0)e^{-\varepsilon_v} \tag{3.9}$$

where ϕ_0 is initial porosity. The permeability change is calculated as:

$$k = k_0\left(\frac{\phi}{\phi_0}\right)^t \tag{3.10}$$

where k_0 is initial permeability.

3.3 Model setup

Horonobe URL

To validate our proposed conceptual model, a hydro-mechanical numerical analysis of temporal change of electrical resistivity and seismic velocity around the tunnel excavation surface at the Horonobe Underground Research Laboratory (URL) site in northwest Hokkaido is made. The layout of the Horonobe URL site in the sedimentary rock is shown in Fig. 3.7. Various in-situ experiments (e.g., geologic investigations) were carried out to study the deep geological environment in sedimentary rocks for providing references for developing geological disposal technologies and safety assessment methodologies (Aoyagi et al., 2019; Aoyagi and Ishii, 2019; Ishii et al., 2011; Mochizuki et al., 2020). The in-situ experiment was also undertaken in the No. 3 tunnel which at 350 m depth in the Neogene siliceous mudstone of the Wakkanai Formation in the URL. The phenomenon that the electrical resistivity and the seismic velocity near the tunnel surface increased after the tunnel excavation was observed. The electrical resistivity near the excavation surface is around 1 $\Omega \cdot$ m in September 2013. In contrast, it reaches around 15 $\Omega \cdot$ m after the tunnel excavation in March 2014. The seismic velocity near the tunnel surface is around 1500 m/s in October 2013. However, it is around 2200 m/s in March 2014. It can be inferred that

the seismic velocity near the No.3 tunnel is also increased after the excavation.

Model boundary conditions and parameters

The model geometry with hydraulic and mechanical boundary conditions is shown in Fig. 3.7. The side length of the rock mass is 50 m. The tunnel at a depth of 350 m is horseshoe-shaped with a height and span of 3.2 m and 4.0 m. The initial stress state the rock mass comes from the in-situ field measurement (Aoyagi and Ishii, 2019). The stress components σ_{xx}, σ_{yy}, and σ_{zz} are set to compressive stresses of 4.81 MPa, 4.81 MPa, and 5.04 MPa, respectively. The pore pressure is initialized to 2.4 MPa. The model boundaries are given no flux, zero displacement boundary conditions while the top boundary is applied a prescribed stress. To simulate the EDZ that developed after the tunnel excavation, a fracture network is generated in the EDZ by the DFN modeling approach. Fig. 3.8 shows a schematic diagram of the DFN model in the EDZ. The side length of the EDZ is 20 m. The DFN model is built based on the in-situ field observations. The DFN model has 3 fracture sets with different fracture densities. The mass densities (P_{32}) for fracture sets are 0.54 m^2/m^3, 0.25 m^2/m^3, and 0.20 m^2/m^3, respectively. The fracture positions are uniform distributed in the rock mass. The fracture lengths of each set obey the power-law distribution with the scaling exponent of 3.5. The maximum, minimum fracture length is 100 m and 1.0, respectively. Since there is no direct information of fracture apertures from the in-situ field measurements, the methodology which is shown in Fig. 3.4 is used to estimate an average fracture. The average aperture is estimated 1.92×10^{-4} m based on the EDZ permeability with a representative value of 3.5×10^{-13} m^2. The fracture volume fraction which is one of model parameters for the dual porosity model in the TOUGH2 is 5.45×10^{-4}.

To derive the desaturation process in the proposed conceptual model, a constant relative humidity in the tunnel is set to 95%. Assuming the ambident air in the tunnel has a temperature of 15°, an equivalent capillary suction with a value of 6.83 MPa is applied on the excavation surface (Eq. 3.2). Fig. 3.9 shows the relative humidity initial condition in the tunnel.

The general workflow for our hydro-mechanical analysis is shown in Fig. 3.10.

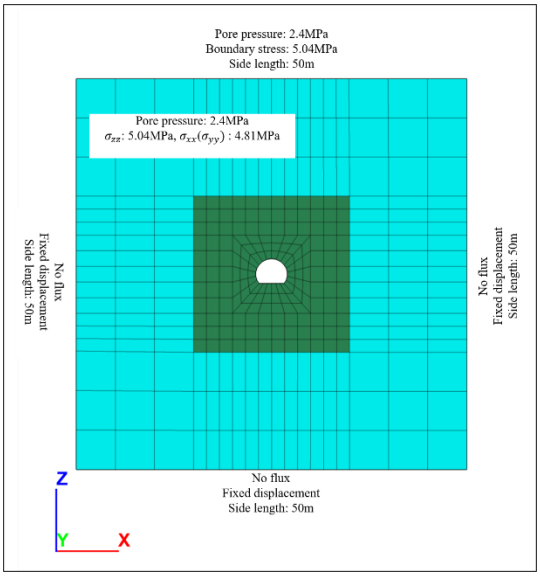

Fig. 3.7. The model geometry with hydraulic and mechanical boundary conditions. The tunnel at a depth of 350 m is horseshoe-shaped with a height and span of 3.2 m and 4.0 m. The stress components σ_{xx}, σ_{yy}, and σ_{zz} are set to compressive stresses of 4.81 MPa, 4.81 MPa, and 5.04 MPa, respectively. The pore pressure is initialized to 2.4 MPa.

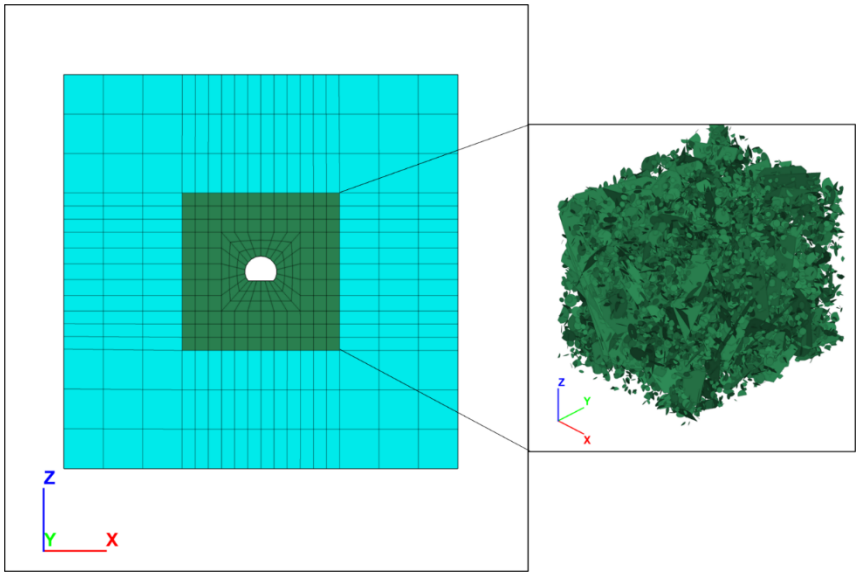

Fig. 3.8. A schematic diagram of the DFN model in the EDZ. The side length of the EDZ is 20m. The mass densities (P32) for fracture sets are 0.54 m^2/m^3, 0.25 m^2/m^3, and 0.20 m^2/m^3, respectively. The fracture positions are uniform distributed in the rock mass. The fracture lengths of each set obey the power-law distribution with the scaling exponent of 3.5. The maximum, minimum fracture length is 100 m and 1.0, respectively.

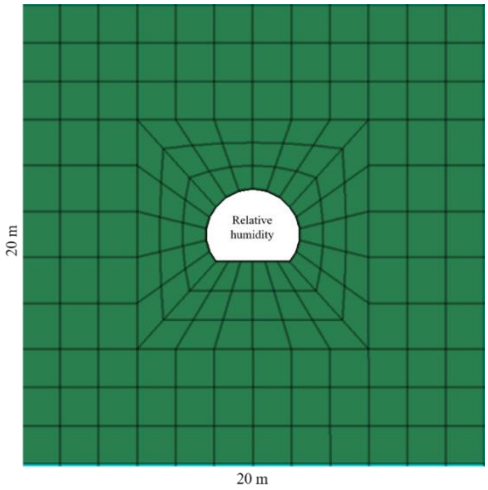

Fig. 3.9. A relative humidity with a value of 95% is applied on the ambident air in the tunnel. Assuming the ambident air has a temperature of 15°, an equivalent capillary suction with a value of 6.83 MPa is prescribed on tunnel excavation surface.

Table 3.1. Key mechanical and physical properties for the hydro-mechanical analysis for validating the proposed conceptual model.

Properties	
Rock	
Young's modulus	1.82 GPa
Poisson's ratio	0.17
Density	1840 kg/m^3
Porosity	0.4
k_0	1.0×10^{-18} m^2
EDZ permeability	3.5×10^{-13} m^2
Electrical resistivity	
n	2
m	2
t	15
Seismic Velocity	
α	0.90
K	9.2×10^{8} Pa
K_f	2.0×10^{9} Pa
ρ_l	1000 kg/m^3
K_s	9.2×10^{9} Pa

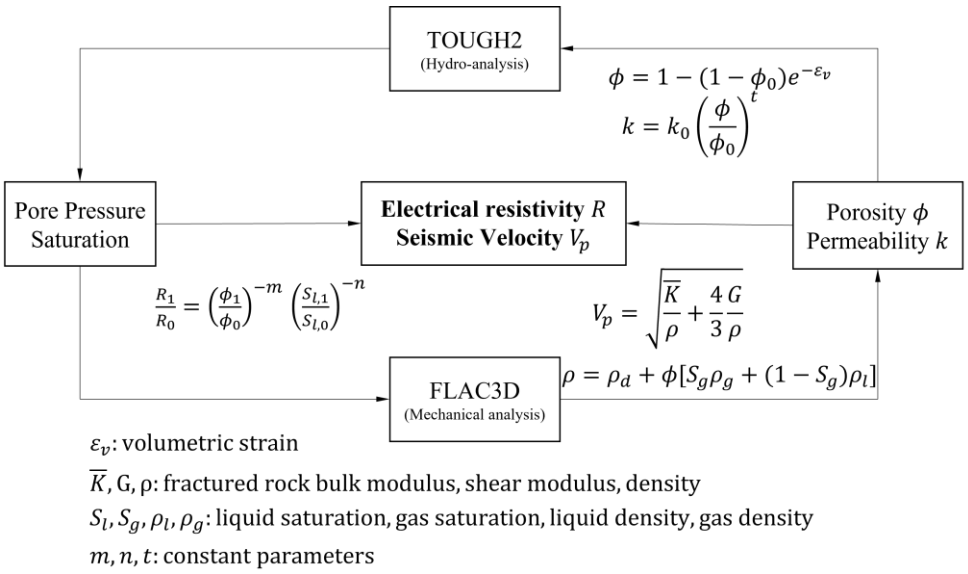

Fig. 3.10. The general workflow for the hydromechanical analysis jointly using FLAC3D and TOUGH2.

3.4 Results

The total simulation time is 6 months with each time step is 1 month. Through our numerical simulation, we find out that the desaturation process in 6 months only causes quite minor of effective stress in the rock mass. Thus, the variations in effective stress, and displacement of the rock mass are neglected.

Capillary pressure

The relative humidity of the air in the tunnel prescribes a strong capillary suction around the tunnel excavation surface. The resultant capillary pressure is shown in Fig. 3.11. Fig. 3.11a shows capillary pressure in the rock mass at 1 month after the tunnel excavation. It shows that the negative capillary pressure developed around the excavation surface. The extent of the capillary pressure decreases gradually as the distance from the excavation surface increases. Figs. 3.11b, 3.11c, 3.11d, 3.11e show the resultant capillary pressure at 2, 3, 4, 5 months, respectively. Though, the capillary pressure increases as time proceeds, it gradually stabilizes. Fig. 3.11f shows the capillary pressure at 6 months. The maximum absolute capillary pressure is around 2.4 MPa. The strong capillary pressure can have a great influence on the rock saturation distribution in the rock mass.

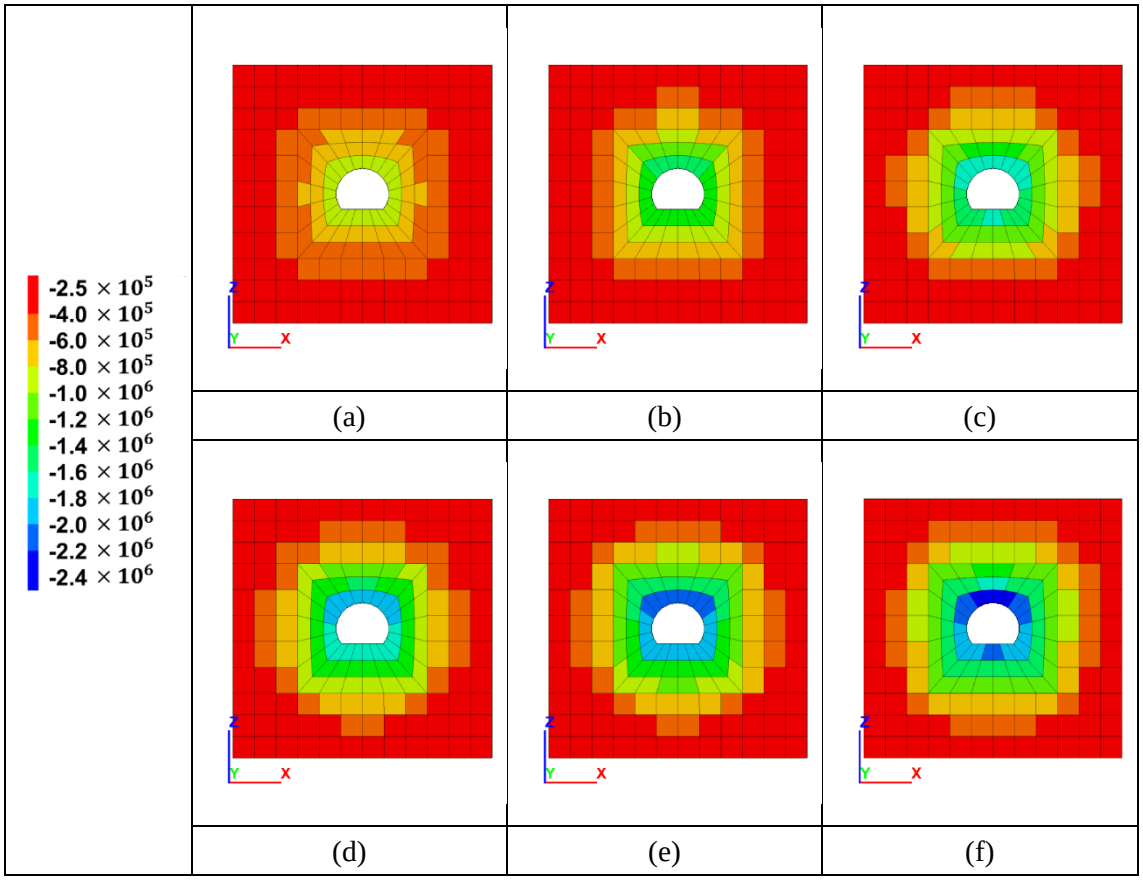

Fig. 3.11. History of capillary pressure in the rock mass: (a), (b), (c), (d), (e), (f) is capillary pressure at 1, 2, 3, 4, 5, 6 months, respectively.

Gas saturation

Fig. 3.12 shows the gas saturation that developed in the rock mass. As time increases, the extent of the gas saturation also increases. The increase rate gradually becomes small. Fig. 3.12a shows the gas saturation at 1 month after the tunnel excavation. The gas saturations around the tunnel do not obviously increase. The initial rock gas saturation is 0.01. The maximum gas saturation which occurs around the tunnel is around 0.35. Figs. 3.12b, 3.12c, 3.12d, 3.12e show gas saturation around tunnel excavation after 2, 3, 4, 5 months, respectively.

The gas saturation increases obviously. At 6 months after the tunnel excavation, the final gas saturations in the rock mass are shown in Fig. 3.12f. The maximum gas saturation is around 0.6. The resultant smallest liquid saturation now is 0.4.

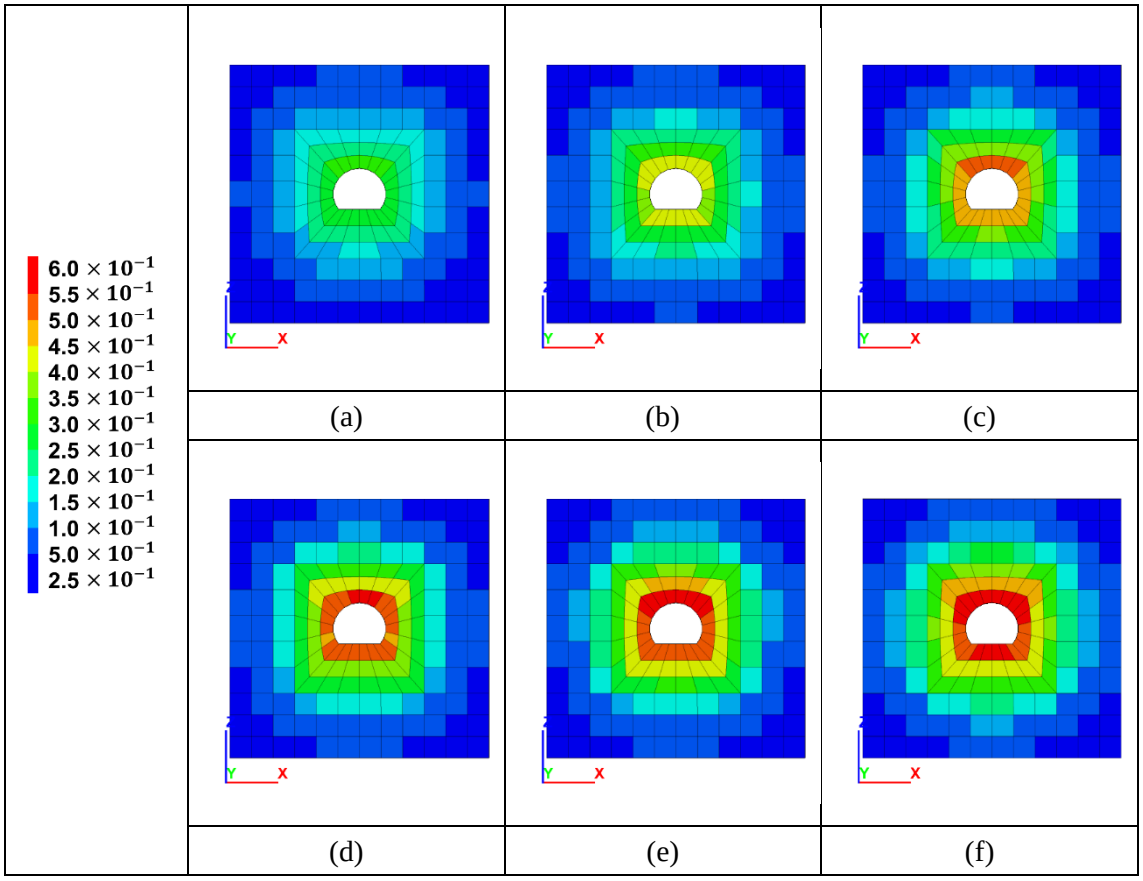

Fig. 3.12. Gas saturation in the rock mass: a, b, c, d, e, f shows gas saturations that developed around tunnel excavation at 1, 2, 3, 4, 5, 6 months, respectively.

Pore pressure

The pore pressure in the rock mass is another parameter that indicates the desaturation process developed in the EDZ. The initial pore pressure set in the model is 1.2 MPa. Fig. 3.13 shows time histories of pore pressures in the rock mass. Fig. 3.13a shows pore pressures at 1 month after the tunnel excavation. It shows that negative pore pressures initialize in the desaturation process. The pore pressures around the tunnel excavation surface are still minor. The absolutes of negative pore pressures increase as time proceeds as shown in Figs. 3.13b, 3.13c, 3.13d, 3.13e, 3.13f. The negative pore pressures developed around tunnel excavation may not be realistic. The potential issue is discussed in detail in the discussion.

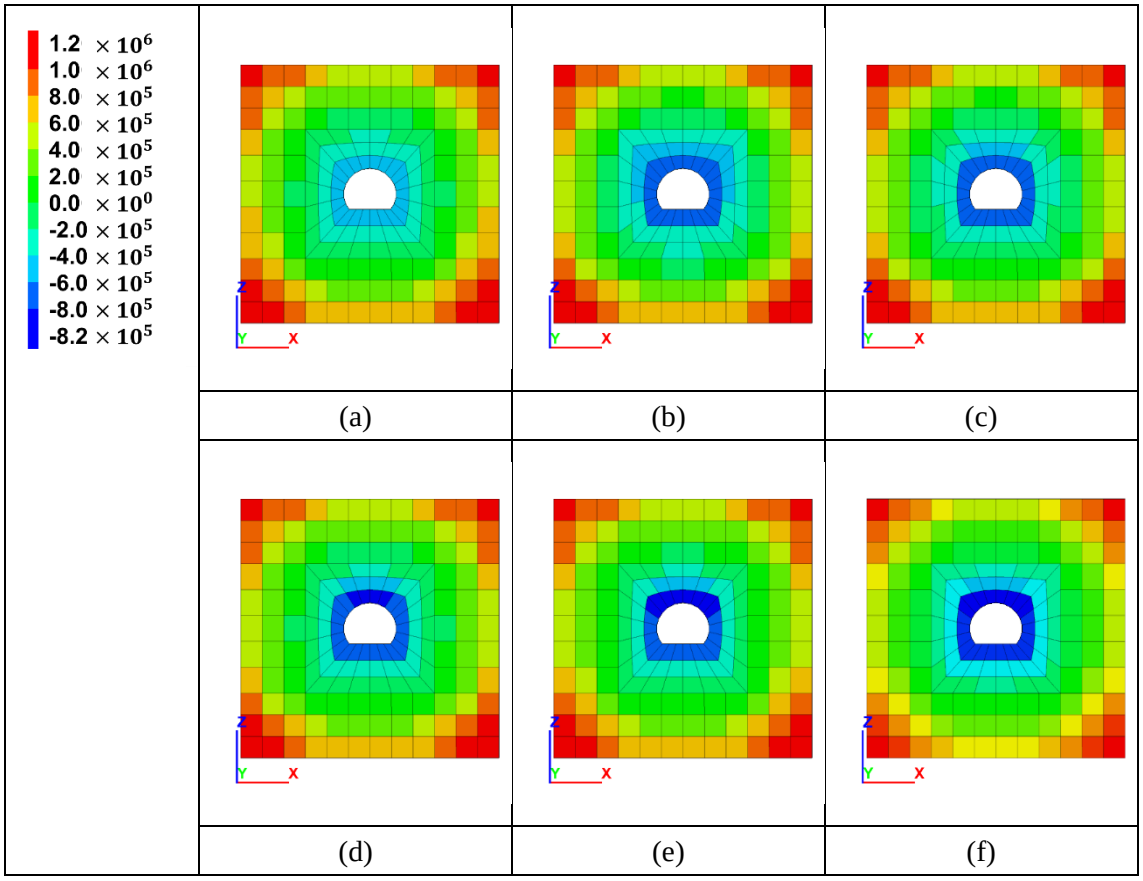

Fig. 3.13. Pore pressure in the rock mass: a, b, c, d, e, f shows pore pressures that developed around tunnel excavation at 1, 2, 3, 4, 5, 6 months.

Electrical resistivity

The electrical resistivities near the tunnel excavation surface at time steps of 1—6 months are shown in Fig. 3.14. At time step 1 month after the excavation, the electrical resistivities near the surface starts to increase though their increase ratio is minor. After two months, the electrical resistivities increase obviously as shown in Fig. 3.14b. Similarly, electrical resistivities continue to increase after three, four, five months, as shown in Figs. 3.14b, 3.14d and 3.14e, respectively. Fig. 3.14f shows the final electrical resistivities. The maximum electrical resistivity is around 5 $\Omega \cdot$ m. The simulation result of electrical resistivities demonstrate that our proposed model can explain the phenomenon that observed in the Horonobe URL. The averaged resistivities around the tunnel in the URL is also similar to numerical results.

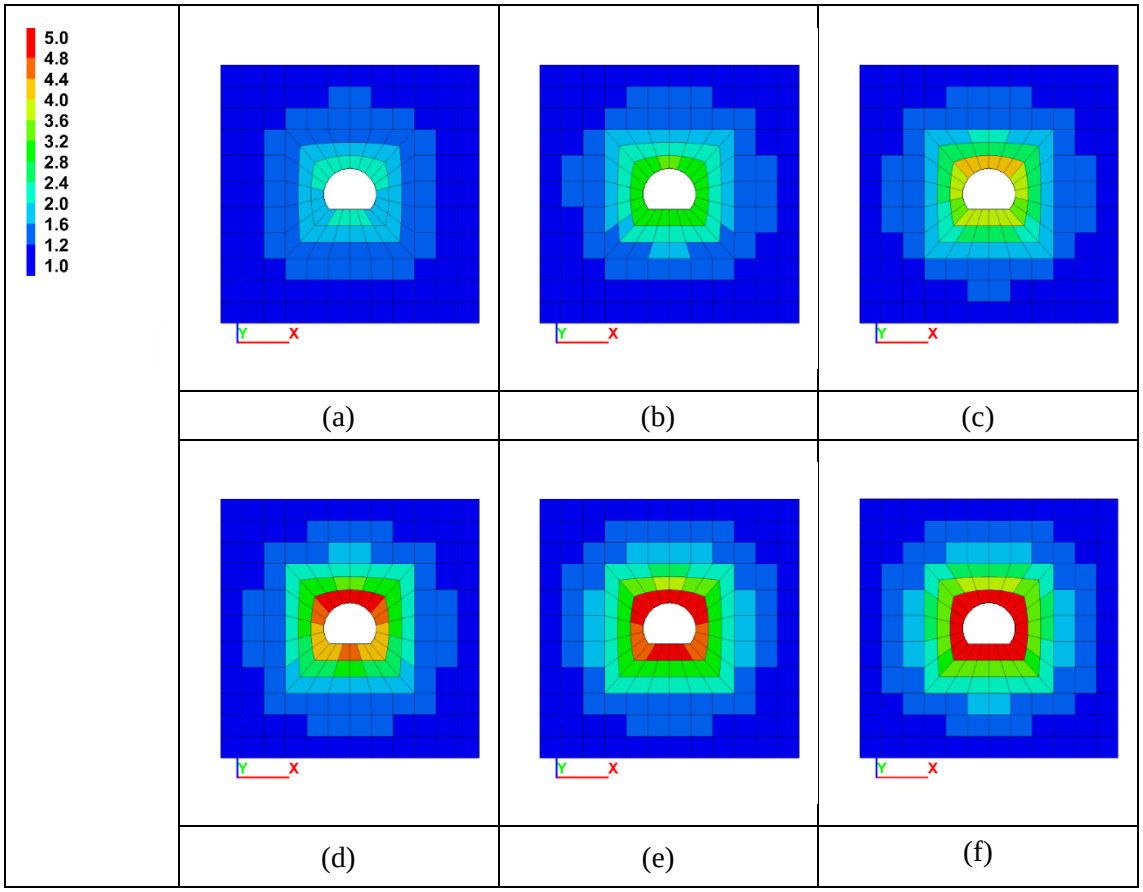

Fig. 3.14. Electrical resistivities around tunnel excavation at times of 1— 6 months, respectively.

Seismic velocity

Similarly, Fig. 3.15 shows seismic velocities around the tunnel excavation. The velocities increase continuously. The initial seismic velocity is around 1650 m/s. However, after 6 months, the maximum seismic velocity is around 1800 m/s, as shown in Fig. 3.15f. The seismic velocities increase continuously. It demonstrates the feasibility of the proposed model to explain the phenomenon observed in the Horonobe URL.

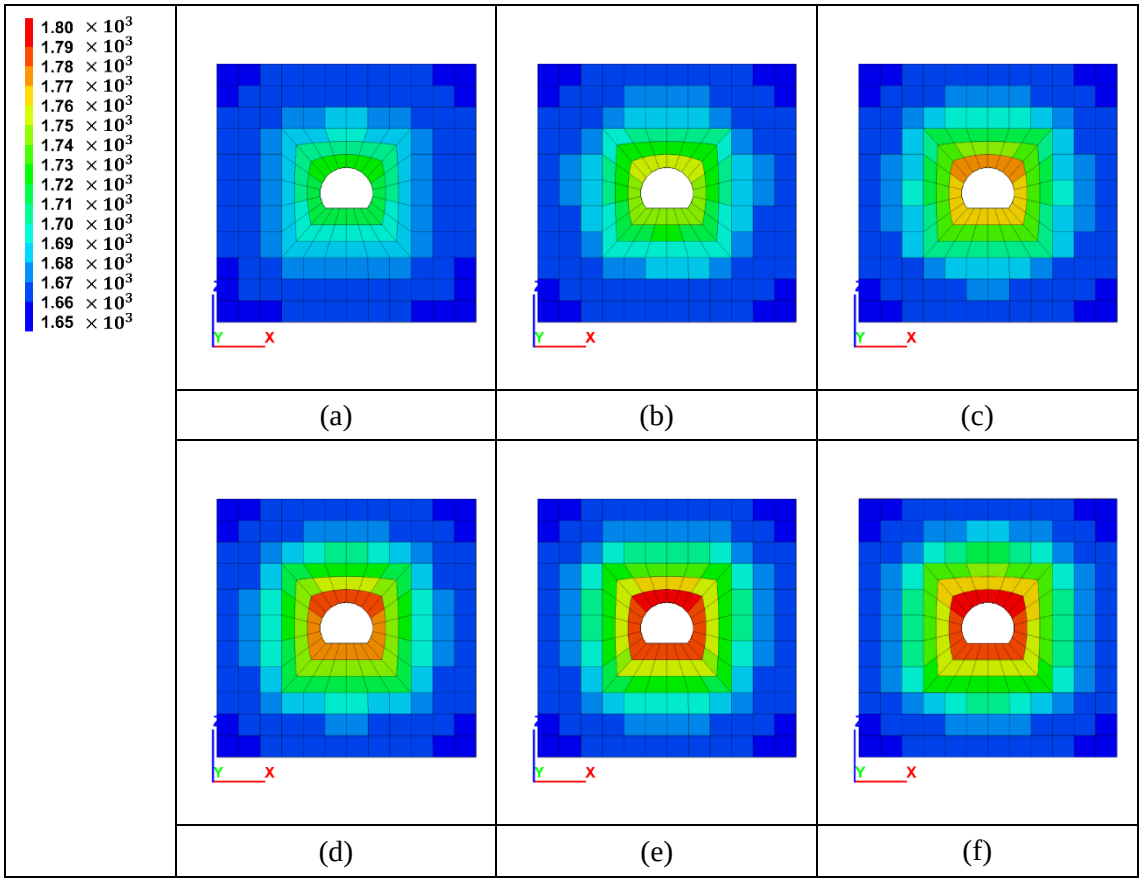

Fig. 3.15. Seismic velocities around tunnel excavation at times of 1—6 months, respectively.

3.5 Discussion

Though our proposed conceptual model can interpret that electrical resistivity and seismic velocity increase after a tunnel excavation which is observed in the Horonobe URL, there are other possible models that also interpret it. Another possible explanation can be the use of shotcrete and rockbolts for the tunnel. On one hand, If the electrical resistivity of shotcrete is larger than that of the rock mass, the electrical resistivity around tunnel excavation surface can also increase after excavation. On the other hand, the use of shotcrete and rockbolts can seal open fractures that developed in the EDZ. The sealing process can also increase electrical resistivity and seismic velocity in the rock mass. However, there is no other extra in-situ field data that support this proposal.

In this chapter, a relatively high relative humidity is assumed. The real relative humidity is not that high. Since there is not much information about relative humidity available. Here, a high relative humidity is assumed. Also, it is assumed that the relative humidity of the ambident air in the tunnel is constant. However, the relative humidity can also change with the temperature in the tunnel. Large negative pore pressures developed around tunnel excavation as shown in Fig. 3.13.

The negative pore pressure indicates that gas pressure is larger than liquid pressure in the pore spaces. The pore spaces may be compressed due to capillary suction around tunnel excavation. Such large negative pore pressure may not be realistic in the Horonobe URL. The negative pore pressures around tunnel excavation in the argillaceous Tournemire site are also observed through a numerical investigation (Maßmann et al., 2009). The validity of large negative pore pressure should be further checked through field measurements.

3.6 Conclusion

A special phenomenon that electrical resistivities and seismic velocities around the tunnel surface were increased after the tunnel excavation was observed the Horonobe URL. To interpret such phenomenon, a conceptual model which considered the desaturation process caused by the ambident air in the tunnel was proposed. The Kelvin's equation was used to relate equivalent capillary pressure applied at the tunnel surface and the relative humidity of the air in the tunnel. The hydromechanical analysis was conducted jointly using TOUGH2 and FLAC3D. Using the simulated gas saturations in the rock mass, the electrical resistivities and seismic velocities were calculated using the Archie's equation and Biot-Gassmann poroelasticity theory. Assuming a constant relative humidity of the tunnel air and prescribing initial and boundary conditions, the hydromechanical analysis was simulated for 6 months. The effect of desaturation process on the change of the stress state in the rock mass was minor thought the analysis. The rock gas saturations driven by the desaturation process increased after the excavation though the increase rate was decreasing. The electrical resistivities and seismic velocities in the rock mass were also increased. The simulation result was in accordance with the observed in the Horonobe URL. Though the proposed conceptual model well explained the phenomenon, other explanations which were discussed in the Discussion were also possible. More field data were necessary to further validate our proposed model.

References

Aoyagi, K., Chen, Y., Ishii, E., Sakurai, A., Ishida, T., 2019. Visualization of Fractures Induced Around the Gallery Wall in Horonobe Underground Research Laboratory. 5th ISRM Young Scholars' Symposium on Rock Mechanics and International Symposium on Rock Engineering for Innovative Future 2019 Dec 1. OnePetro.

Aoyagi, K., Ishii, E., 2019. A Method for Estimating the Highest Potential Hydraulic Conductivity in the Excavation Damaged Zone in Mudstone. Rock Mech. Rock Eng. 52, 385–401. https://doi.org/10.1007/s00603-018-1577-z

Archie, G.E., 2003. The Electrical Resistivity Log as an Aid in Determining Some Reservoir Characteristics. SPE Repr. Ser. https://doi.org/10.2118/942054-g

Baecher, G.B., 1983. Statistical analysis of rock mass fracturing. J. Int. Assoc. Math. Geol. 15, 329–348. https://doi.org/10.1007/BF01036074

Biot, M.A., 1956. Theory of propagation of elastic waves in a fluid-saturated porous solid, I: Low-frequency range. J. Acoust. Soc. Am. 28, 168–191.

Bossart, P., Meier, P.M., Moeri, A., Trick, T., Mayor, J.C., 2002. Geological and hydraulic characterisation of the excavation disturbed zone in the Opalinus Clay of the Mont Terri Rock Laboratory. Eng. Geol. 66, 19–38. https://doi.org/10.1016/S0013-7952(01)00140-5

Cai, M., Kaiser, P.K., 2005. Assessment of excavation damaged zone using a micromechanics model. Tunn. Undergr. Sp. Technol. 20, 301–310. https://doi.org/10.1016/j.tust.2004.12.002

Charpentier, D., Tessier, D., Cathelineau, M., 2003. Shale microstructure evolution due to tunnel excavation after 100 years and impact of tectonic paleo-fracturing. Case of Tournemire, France. Eng. Geol. 70, 55–69. https://doi.org/10.1016/S0013-7952(03)00082-6

Chen, G., Song, L., Liu, L., 2019. 3D Numerical Simulation of Elastic Wave Propagation in Discrete Fracture Network Rocks. Pure Appl. Geophys. 176, 5377–5390. https://doi.org/10.1007/s00024-019-02287-0

Chen, G., Song, L., Zhang, R.R., 2018. Modeling acoustic attenuation of discrete stochastic fractured media. Acta Geod. Geophys. 53, 679–690. https://doi.org/10.1007/s40328-018-0237-9

Day-Lewis, F.D., Slater, L.D., Robinson, J., Johnson, C.D., Terry, N., Werkema, D., 2017. An overview of geophysical technologies appropriate for characterization and monitoring at fractured-rock sites. J. Environ. Manage. 204, 709–720. https://doi.org/10.1016/j.jenvman.2017.04.033

De Basabe, J.D., Sen, M.K., Wheeler, M.F., 2016. Elastic wave propagation in fractured media using the discontinuous Galerkin method. Geophysics 81, T163–T174. https://doi.org/10.1190/GEO2015-0602.1

Donaldson, E.C., Siddiqui, T.K., 1989. Relationship between the Archie saturation exponent and wettability. SPE Form. Eval. 4. https://doi.org/10.2118/16790-pa

Edlefsen, N.E., Anderson, A.B.C., 1943. Thermodynamics of soil moisture. Hilgardia 15, 31–298. https://doi.org/10.3733/hilg.v15n02p031

Falls, S.D., Young, R.P., 1998. Acoustic emission and ultrasonic-velocity methods used to characterise the excavation disturbance associated with deep tunnels in hard rock. Tectonophysics 289, 1–15. https://doi.org/10.1016/S0040-1951(97)00303-X

Finsterle, S., Pruess, K., 1995. Solving the Estimation-Identification Problem in Two-Phase Flow Modeling. Water Resour. Res. 31, 913–924. https://doi.org/10.1029/94WR03038

Galvin, R.J., Gurevich, B., 2015. Frequency-dependent anisotropy of porous rocks with aligned fractures. Geophys. Prospect. 63, 141–150. https://doi.org/10.1111/1365-2478.12177

Gassmann, F., 1951. Elasticity of porous media. Vierteljahrsschr. Naturforsch. Gesselschaft 96, 1–23.

Germán Rubino, J., Guarracino, L., Müller, T.M., Holliger, K., 2013. Do seismic waves sense fracture

connectivity? Geophys. Res. Lett. 40, 692–696. https://doi.org/10.1002/grl.50127

Gou, Y., Hou, Z., Li, M., Feng, W., Liu, H., 2016. Coupled thermo–hydro–mechanical simulation of CO2 enhanced gas recovery with an extended equation of state module for TOUGH2MP-FLAC3D. J. Rock Mech. Geotech. Eng. 8, 904–920. https://doi.org/10.1016/J.JRMGE.2016.08.002

Gutierrez, M., Katsuki, D., Almrabat, A., 2012. Effects of CO2 Injection on the Seismic Velocity of Sandstone Saturated with Saline Water. Int. J. Geosci. 03, 908–917. https://doi.org/10.4236/ijg.2012.325093

Hunziker, J., Favino, M., Caspari, E., Quintal, B., Rubino, J.G., Krause, R., Holliger, K., 2018. Seismic Attenuation and Stiffness Modulus Dispersion in Porous Rocks Containing Stochastic Fracture Networks. J. Geophys. Res. Solid Earth 123, 125–143. https://doi.org/10.1002/2017JB014566

Hyman, J.D., Hagberg, A., Osthus, D., Srinivasan, S., Viswanathan, H., Srinivasan, G., 2018. Identifying Backbones in Three-Dimensional Discrete Fracture Networks: A Bipartite Graph-Based Approach. Multiscale Model. Simul. 16, 1948–1968. https://doi.org/10.1137/18m1180207

Ishii, E., Sanada, H., Funaki, H., Sugita, Y., Kurikami, H., 2011. The relationships among brittleness, deformation behavior, and transport properties in mudstones: An example from the Horonobe Underground Research Laboratory, Japan. J. Geophys. Res. 116, B09206. https://doi.org/10.1029/2011JB008279

J.D., D.B., M.K., S., M.F., W., n.d. Elastic wave propagation in fractured media using the discontinuous Galerkin method. Geophysics 81, T163–T174.

Kong, L., Gurevich, B., Zhang, Y., Wang, Y., 2017. Effect of fracture fill on frequency-dependent anisotropy of fractured porous rocks. Geophys. Prospect. 65, 1649–1661. https://doi.org/10.1111/1365-2478.12505

Kruschwitz, S., Yaramanci, U., 2004. Detection and characterization of the disturbed rock zone in claystone with the complex resistivity method. J. Appl. Geophys. 57, 63–79. https://doi.org/10.1016/j.jappgeo.2004.09.003

Kwon, S., Lee, C.S., Cho, S.J., Jeon, S.W., Cho, W.J., 2009. An investigation of the excavation damaged zone at the KAERI underground research tunnel. Tunn. Undergr. Sp. Technol. 24, 1–13. https://doi.org/10.1016/j.tust.2008.01.004

Lee, M.W., 2002. Modified Biot-Gassmann theory for calculating elastic velocities for unconsolidated and consolidated sediments. Mar. Geophys. Res. 23, 403–412. https://doi.org/10.1023/b:mari.0000018195.75858.12

Lei, Q., Latham, J.P., Tsang, C.F., 2017. The use of discrete fracture networks for modelling coupled geomechanical and hydrological behaviour of fractured rocks. Comput. Geotech. https://doi.org/10.1016/j.compgeo.2016.12.024

Mochizuki, A., Ishii, E., Miyakawa, K., Sasamoto, H., 2020. Mudstone redox conditions at the Horonobe

Underground Research Laboratory, Hokkaido, Japan: Effects of drift excavation. Eng. Geol. 267, 105496. https://doi.org/10.1016/j.enggeo.2020.105496

Maßmann, J., Uehara, S.I., Rejeb, A., Millard, A., 2009. Investigation of desaturation in an old tunnel and new galleries at an argillaceous site. Environ. Geol. 57, 1337–1345. https://doi.org/10.1007/s00254-008-1438-2

Matray, J.M., Savoye, S., Cabrera, J., 2007. Desaturation and structure relationships around drifts excavated in the well-compacted Tournemire's argillite (Aveyron, France). Eng. Geol. 90, 1–16. https://doi.org/10.1016/j.enggeo.2006.09.021

Min, K.B., Jing, L., 2003. Numerical determination of the equivalent elastic compliance tensor for fractured rock masses using the distinct element method. Int. J. Rock Mech. Min. Sci. 40, 795–816. https://doi.org/10.1016/S1365-1609(03)00038-8

Min, K.B., Jing, L., Stephansson, O., 2004. Determining the equivalent permeability tensor for fractured rock masses using a stochastic REV approach: Method and application to the field data from Sellafield, UK. Hydrogeol. J. 12, 497–510. https://doi.org/10.1007/s10040-004-0331-7

Mochizuki, A., Ishii, E., Miyakawa, K., Sasamoto, H., 2020. Mudstone redox conditions at the Horonobe Underground Research Laboratory, Hokkaido, Japan: Effects of drift excavation. Eng. Geol. 267, 105496. https://doi.org/10.1016/j.enggeo.2020.105496

Mohamad, A.M., Hamada, G.M., 2017. Determination techniques of Archie's parameters: *a* , *m* and *n* in heterogeneous reservoirs. J. Geophys. Eng. 14, 1358–1367. https://doi.org/10.1088/1742-2140/aa805c

Möller, T., Friederich, W., 2019. Simulation of elastic wave propagation across fractures using a nodal discontinuous Galerkin method-theory, implementation and validation. Geophys. J. Int. 219, 1900–1914. https://doi.org/10.1093/gji/ggz410

Nicollin, F., Gibert, D., Bossart, P., Nussbaum, C., Guervilly, C., 2008. Seismic tomography of the Excavation Damaged Zone of the Gallery 04 in the Mont Terri Rock Laboratory. Geophys. J. Int. 172, 226–239. https://doi.org/10.1111/j.1365-246X.2007.03615.x

Nicollin, F., Gibert, D., Lesparre, N., Nussbaum, C., 2010. Anisotropy of electrical conductivity of the excavation damaged zone in the Mont Terri Underground Rock Laboratory. Geophys. J. Int. 181, 303–320. https://doi.org/10.1111/j.1365-246X.2010.04517.x

Pruess, K., 1992. Brief guide to the MINC-method for modeling flow and transport in fractured media. Berkeley, CA. https://doi.org/10.2172/6951290

Pruess, K., Oldenburg, C., Moridis, G., 1999. TOUGH2 USER'S GUIDE, VERSION 2.

Schuster, K., Alheid, H.J., Böddener, D., 2001a. Seismic investigation of the Excavation damaged zone in Opalinus Clay. Eng. Geol. 61, 189–197. https://doi.org/10.1016/S0013-7952(01)00054-0

Schuster, K., Alheid, H.J., Böddener, D., 2001b. Seismic investigation of the Excavation damaged zone in Opalinus Clay. Eng. Geol. 61, 189–197. https://doi.org/10.1016/S0013-7952(01)00054-0

Shao, H., Schuster, K., Sönnke, J., Bräuer, V., 2008. EDZ development in indurated clay formations - In situ borehole measurements and coupled HM modelling. Phys. Chem. Earth 33, 5388–5395. https://doi.org/10.1016/j.pce.2008.10.031

Song, Y., Hu, H., Han, B., 2020. Seismic attenuation and dispersion in a cracked porous medium: An effective medium model based on poroelastic linear slip conditions. Mech. Mater. 140, 103229. https://doi.org/10.1016/j.mechmat.2019.103229

Spies, T., Eisenblätter, J., 2001. Acoustic emission investigation of microcrack generation at geological boundaries. Eng. Geol. 61, 181–188. https://doi.org/10.1016/S0013-7952(01)00053-9

Tsang, C.F., Bernier, F., Davies, C., 2005. Geohydromechanical processes in the Excavation Damaged Zone in crystalline rock, rock salt, and indurated and plastic clays - In the context of radioactive waste disposal. Int. J. Rock Mech. Min. Sci. 42, 109–125. https://doi.org/10.1016/j.ijrmms.2004.08.003

Valera, M., Guo, Z., Kelly, P., Matz, S., Cantu, V.A., Percus, A.G., Hyman, J.D., Srinivasan, G., Viswanathan, H.S., 2018. Machine learning for graph-based representations of three-dimensional discrete fracture networks. Comput. Geosci. 22, 695–710. https://doi.org/10.1007/s10596-018-9720-1

Valès, F., Nguyen Minh, D., Gharbi, H., Rejeb, A., 2004. Experimental study of the influence of the degree of saturation on physical and mechanical properties in Tournemire shale (France). Appl. Clay Sci. 26, 197–207. https://doi.org/10.1016/j.clay.2003.12.032

Viswanathan, H.S., Hyman, J.D., Karra, S., O'Malley, D., Srinivasan, S., Hagberg, A., Srinivasan, G., 2018. Advancing Graph-Based Algorithms for Predicting Flow and Transport in Fractured Rock. Water Resour. Res. 54, 6085–6099. https://doi.org/10.1029/2017WR022368

Wright, C., Walls, E.J., De, D., 2000. The seismic velocity distribution in the vicinity of a mine tunnel at Thabazimbi, South Africa. J. Appl. Geophys. 44, 369–382. https://doi.org/10.1016/S0926-9851(00)00014-8

Zhan, Q., Sun, Q., Ren, Q., Fang, Y., Wang, H., Liu, Q.H., 2017. A discontinuous Galerkin method for simulating the effects of arbitrary discrete fractures on elastic wave propagation. Geophys. J. Int. 210, 1219–1230. https://doi.org/10.1093/gji/ggx233

Zhao, Z., Li, B., Jiang, Y., 2013. Effects of Fracture Surface Roughness on Macroscopic Fluid Flow and Solute Transport in Fracture Networks. Rock Mech. Rock Eng. 47, 2279–2286. https://doi.org/10.1007/s00603-013-0497-1

Zimmerman, R.W., Bodvarsson, G.S., 1996. Effective transmissivity of two-dimensional fracture networks. Int. J. Rock Mech. Min. Sci. Geomech. 33, 433–438. https://doi.org/10.1016/0148-9062(95)00067-4

Chapter 4

Estimating fractured rock equivalent permeability using fractures characterized by FEMDEM method

4.1 Introduction

Estimating equivalent permeability of fractured rocks is quite important in engineering practice, such as hydrology engineering , rock engineering, geotechnical and underground engineering, and has raised much attention (Baghbanan and Jing, 2007; K.-B. Min et al., 2004). For a natural fractured rock mass, there are many methods that can be adopted to estimate its equivalent permeability. The Oda's crack tensor theory (Oda, 1985) which is derived from the Snow model (Snow, 1969), and effective medium methods (Sævik et al., 2013) are popular analytical methods to calculate permeability of a fractured media. Numerical upscaling is another straightforward alternative approach to calculate permeability of a fractured rock mass for its relative high accuracy (e.g., K. B. Min et al., 2004). The numerical upscaling methods require that they can handle fluid flow through fractures. Many numerical based methods that simulate fluid flow and transport through fractured rock have been developed such as the Equivalent Continuum (EC) model (Barenblatt et al., 1960; Warren and Root, 1963), the Discrete Fracture-Matrix (DFM) model (Karimi-Fard and Firoozabadi, 2001; Wang et al., 2020), discrete fracture network (DFN) model (e.g., Valera et al., 2017), and Pipe Network (PN) model (e.g., Dershowitz and Fidelibus, 1999; Leung et al., 2012; Liu et al., 2019). The EC model which requires fracture rock is homogenous can be divided into dual porosity model, dual permeability model (Vogel et al., 2000), and multi-continuum approach (Pruess and Narasimhan, 1982; Pruess et al., 1999).

Fracturing processes are often encountered in underground excavations for geological disposal of nuclear waste, tunnel construction and geothermal production. Further developed natural existed fractures and newly formed fractures contribute to changing equivalent permeability of fractured rock masses. The effect of fracture initialization and propagation on the progressive evolution of fractured rock permeability is important. The numerical methods are based on continuum or discontinuum assumptions (Lisjak and Grasselli, 2014; Shen, 2014). The continuum-based numerical method which incorporates plasticity-based material models assumes that the computational domain is regarded as a single continue body. In contrast, the discontinuum approach directly treats the domain as discrete bodies. Based on such assumption, the FEMDEM fracture model has been developed. The model has been widely applied in modeling fracture initialization and propagation (Lei et al., 2017; Mahabadi et al., 2012). The permeability evolution with the development of fractures simulated by the FEMDEM fracture model has not been investigated yet. In this chapter, a numerical-based approach is developed to characterize such

evolution.

The chapter is organized as follows. The FEMDEM fracture model and the unified pipe network method are introduced in detail. To verify the unified pipe network model in modeling fluid flow in a fractured media, two representative cases: a single fracture which is embedded in rock matrix, and a DFN model where fractures are statistically described are carried out. Then, a uniaxial compression test of a rock specimen is made to show our combined FEMDEM fracture model and the pipe network method can capture the progressive evolution of equivalent permeability of fractured rock. Finally, a numerical simulation of a tunnel excavation in a deep underground is made to calculate the equivalent permeability of a fractured rock mass. The last two cses

4.2 Theories and methods

FEMDEM fracture model

The combined finite-discrete element (FEMDEM) fracture model has been well developed to simulate fracture initialization and propagation in fractured rock mass (Lisjak and Grasselli, 2014; Munjiza, 2004; Munjiza et al., 1995). The FEMDEM fracture model requires a two-dimensional (2D) unstructured mesh of triangular elements which are surrounded by the four-node joint elements (Fig. 4.1). The elastic deformation of fractured rock is calculated from a linear elastic finite element analysis using linear triangular elements. For an isotropic linear elastic model, its behavior is fully characterized by Young's modulus and Poisson's ratio. The fracture initialization and propagation in fractured rock are modeled by a cohesive zone approach. The fracture behaviors are captured by the four-node joint elements. The joint elements are created between triangular elements pairs. The joint element is regarded as a broken element transited from unbroken one if a fracture initializes and propagates.

The fracture criterion of joint elements is shown in Fig. 4.2. There are three types of modes that characterize failures of joint elements, namely, Mode I, Mode II, and a mixed mode of Mode I and Mode II. As Fig. 4.2a shows, in the Mode I, the initiation and evolution of damage occur in the joint element as the joint opening amount of two sides of the joint element increases over a critical value δ_0. As the joint opening amount increases and is equal to the maximum opening amount δ_f, the joint element breaks and a tensile fracture is created. In the Mode II as shown in Fig. 4.2b, the initiation and evolution of shear damage starts in the join element when the tangential slip amount of two sides of the joint element increases over a critical value s_0. A shear fracture is generated when the joint slip amount is equal to the maximum slip amount s_f. In the mixed mode of Modes I and II, a fracture of a mixed type of shear and tensile failure of the joint element is generated when the joint opening is equal to δ_f and the joint slip is equal to s_f.

The combined FEMDEM model can well characterize the behaviors of the initialization and

propagation of fractures due to local stress perturbation in fractured rock such as a tunnel excavation. Fig. 4.3 shows two representative cases of fracture initiation and propagation in rocks which are modeled by the hybrid FEMDEM fracture model. Fig. 4.3a shows a uniaxial compressive strength (UCS) test which is used to study the material behavior in tension and compression of an intact rock. Under the axial loading in the UCS simulation, the progressive damage of intact rock is characterized by the initiation and propagation of fractures which are modeled by the hybrid FEMDEM model. Fig. 4.3b shows the progressive evolution of rock mass failure around a tunnel excavation surface modeled. The developed excavation damaged zone (EDZ) is characterized by fractures simulated by the FEMDEM fracture model. Fluid flow through fractures modeled by the FEMDEM model can be easily simulated by the unified pipe network model which will be introduced later.

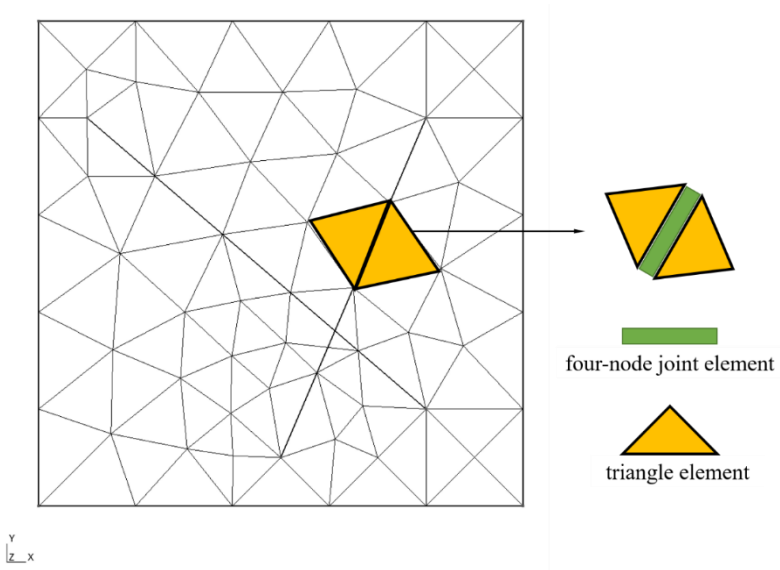

Fig. 4.1. Schematic diagram of an unstructured mesh of triangular elements surrounded the four-node joint elements used by the hybrid FEMDEM fracture model. The deformation behaviors of rock matrix and fracture initialization and propagation are captured by the triangular elements and the four-node joint elements, respectively.

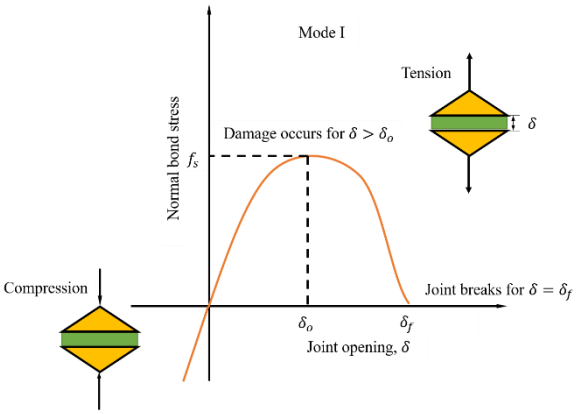

(a)

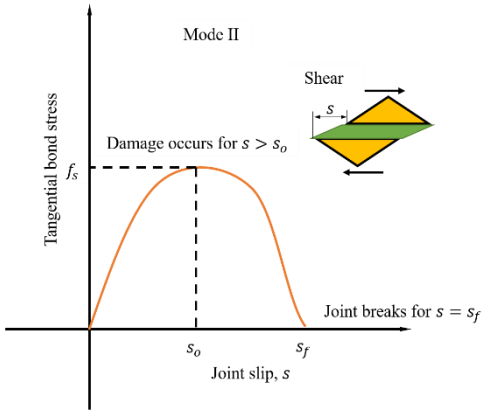

(b)

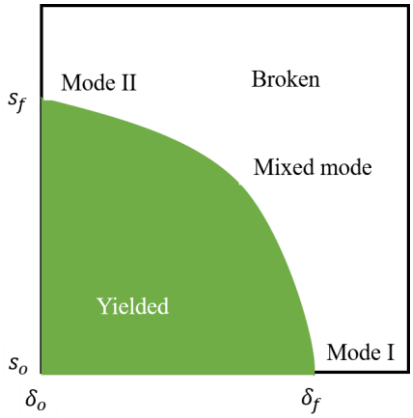

(c)

Fig. 4.2. Schematic illustrations of fracture initiation and propagation modeled by a four-node joint element: (a) Mode I describing relationship between normal bond stress and joint opening; (b) Mode II describing relationship between tangential bond stress and joint slip; (c) Mixed mode of Mode I and Mode II. (a), (b), and (c) are modified from (Lisjak et al., 2014)

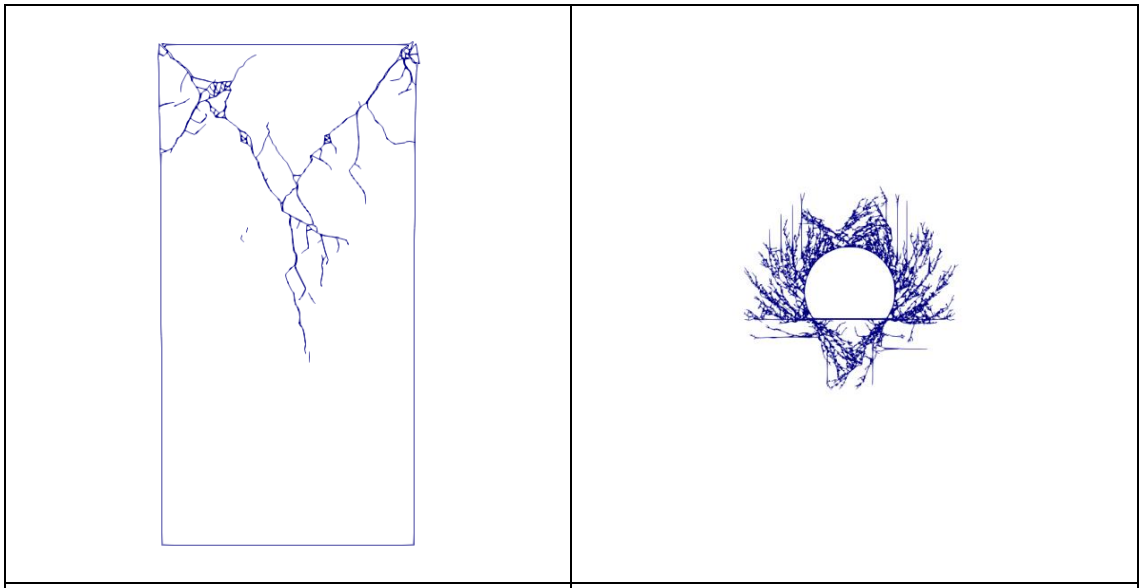

(a) (b)

Fig. 4.3. Two representative cases which are modeled by the FEMDEM fracture model: (a) a uniaxial compressive strength (UCS) laboratory test on an intact rock; (b) a local stress perturbation due to a tunnel excavation in the rock mass.

Unified pipe network model

To calculate equivalent permeability of fractured rock through a numerical way, the fluid pressure distribution should be estimated. Following the unified pipe-network model proposed by (Ren et al., 2017), fluid pressures in the unstructured mesh of triangular matrix elements and four-node fracture elements under hydraulic boundary conditions can be calculated. In the unified pipe network model, the fractured rock mass is divided into a pipe network system as shown in Fig. 4.4. Fig. 4.4a illustrates the rock matrix into which natural fractures are embedded. Fig. 4.4b shows a unified pipe network system representing the fractured rock mass. There are two types of pipes which are shown in Fig. 4.4b: matrix pipes that represent rock matrix, and fracture pipes that represent fractures. The unified pipe network model has an advantage over the traditional pipe network model (e.g., Heydari et al., 2018; Li et al., 2014) in that the former can consider dead-end fractures which are also important in fluid flow in fractured rock.

The equivalent hydraulic parameters of both matrix pipes and fracture pipes are derived from the locally homogenized macroscopic media. The Darcy's law is valid for modeling fluid flow in both matrix pipes and fracture pipes. The Darcy's law is defined as:

$$Q = K\Delta p \tag{4.1}$$

where Q is the flow rate in the pipe, K which is expressed in different forms for matrix pipes and fracture pipes, is the pipe conductance coefficient, p is the fluid pressure potential. For a steady-state fluid flow, a nodal flow at each pipe node which obeys the law of conservation of mass can

be expressed as:

$$\sum_{i=1}^{n} Q_i = Q_{si} \tag{4.2}$$

where n is the total number of pipes that connected to the node, Q_i is the flow rate, and Q_{si} is the source term. A general governing equation of the Darcy's law in a matrix form by substituting Eq. 4.2 into Eq. 4.1 is written as follows:

$$[K]_{n\times n}\{J\}_{n\times 1} = \{Q_s\}_{n\times 1} \tag{4.3}$$

Prescribing the Neumann boundary condition and the Dirichlet boundary condition, the governing equation can be solved numerically. The flow rate in an idealized fracture pipe homogenized from a natural rough fracture by the parallel plate model obeys the cubic law which is defined as (Li et al., 2014; Priest, 1993; Ren et al., 2017; Schrauf and Evans, 1986; Tsang and Witherspoon, 1981):

$$Q = \frac{a^3}{12u}\frac{\partial p}{\partial l} \tag{4.4}$$

where a is the fracture aperture, u is the fluid viscosity, l is the fracture pipe length. Here, fracture permeability k_f is defined as:

$$k_f = \frac{a^2}{12} \tag{4.5}$$

Another general form of calculating the flow rate through the fracture pipe is defined as:

$$Q = \frac{ak_f}{u}\frac{\partial p}{\partial l} \tag{4.6}$$

A rock matrix triangle element is discretized into three matrix pipe elements as shown by Fig. 4.5. o is the circumcenter of the triangle ijk. l_{of} is the length of the perpendicular from o to the line ij. The equivalent conductance coefficient K_{ij} of the matrix pipe which connecting node i and node j is defined as:

$$K_{ij} = \frac{l_{of}k}{l_{ij}u} \tag{4.7}$$

where l_{ij} is the length of the line ij, k is the permeability of rock matrix. Similarly, the equivalent conductance coefficients for pipes connecting nodes im and nodes jm are defined as:

$$K_{im} = \frac{l_{oe}k}{l_{im}u} \tag{4.8}$$

$$K_{jm} = \frac{l_{og}k}{l_{jm}u} \tag{4.9}$$

The flow rate Q_{ij} through the matrix pipe ij is defined as:

$$Q_{ij} = K_{ij}(p_i - p_j) \tag{4.10}$$

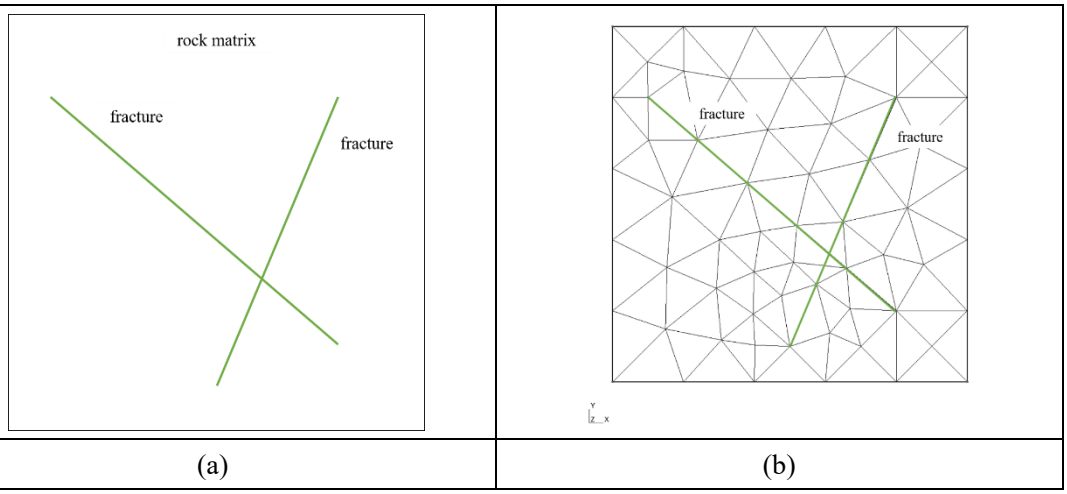

Fig. 4.4. Schematic diagram of the unified pipe-network model: (a) a 2D fractured rock mass; (b) fracture pipes corresponding to fractures and matrix pipes corresponding to rock matrix.

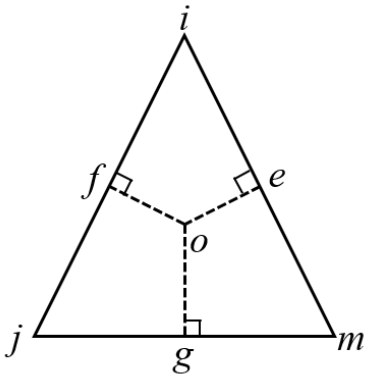

Fig. 4.5. Schematic diagram of rock matrix which is discretized into three matrix pipes for deriving the matrix pipe conductance. *o* represents the center of rock matrix.

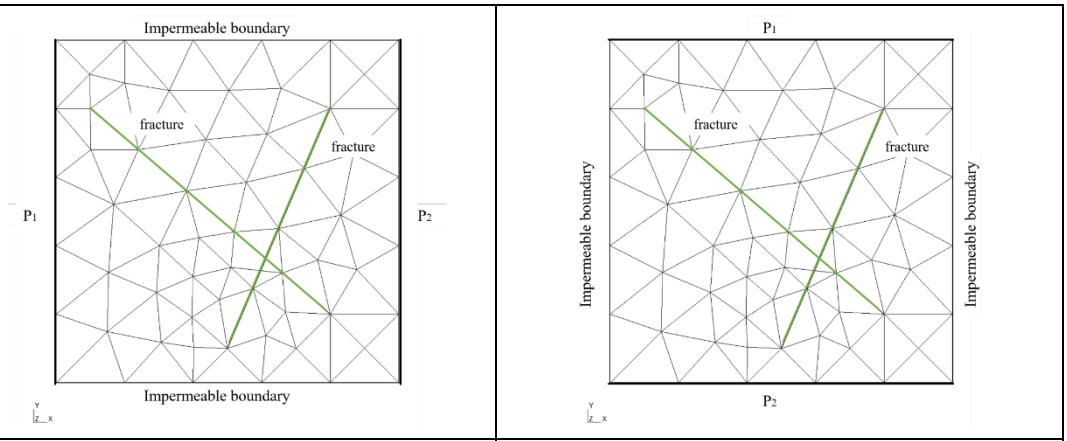

Fig. 4.6. Schematic diagram of boundary conditions for two numerical experiments to estimate

of the equivalent permeability of fractured rock: (a) the left boundary and right boundary are prescribed as constant pressure boundary conditions with of P_1 = 1 Pa, P_0 = 0 Pa; (b) the top boundary and bottom boundary are prescribed as constant pressure boundary conditions with of P_1 = 1 Pa, P_0 = 0 Pa. The boundary conditions are used in the unified pipe network model to estimate pressures in the model.

Equivalent permeability

There are two terms regarding fractured rock permeability: equivalent permeability and effective permeability (Amaziane et al., 2001; Lang et al., 2014; Renard and De Marsily, 1997). The effective permeability exists if a representative elementary volume (REV) is well defined in fractured rock. However, the REV does not necessarily exist if the fracture network lacks a homogenization scale to represent a heterogeneous medium. Since whether the REV exists in fractured rock is not checked, the equivalent permeability is estimated in this chapter. The equivalent permeability varies with scale and are not an intrinsic property of fractured rock. The equivalent permeability is defined as follows:

$$\mathbf{k} = \begin{bmatrix} k_{xx} & k_{xy} \\ k_{yx} & k_{yy} \end{bmatrix} \tag{4.11}$$

where k_{xx} presents the dependence of flow rate along the *x* axis on pressure difference which is also along the *x* axis in a Cartesian two-dimensional coordinate system; similarly, k_{yy} represents the dependence of flow rate along the *y* axis on pressure difference which is also along the *y* axis; k_{xy} accounts for the dependence of flow rate along the *x* axis on pressure difference which is long the y axis; k_{yx} accounts for the dependence of flow rate along the *y* axis on pressure difference which is long the *x* axis. Theoretically, $\mathbf{k}$ is a symmetric positive-define tensor which indicates $k_{xy} = k_{yx}$. However, for a numerical method which determines $\mathbf{k}$ does not always make sure that $k_{xy} = k_{yx}$ holds true. The Darcy's law which describes the relationship between flow rate and hydraulic head gradient is expressed as follows for anisotropic fractured rock:

$$u_j = \frac{k_{ij}}{\mu}\frac{\partial p}{\partial x_i} \tag{4.12}$$

where u_j is flow rate along the *j* axis, k_{ij} are the components of $\mathbf{k}$, μ is the dynamic viscosity of the fluid, $\frac{\partial p}{\partial x_i}$ is the pressure gradient in the *i* direction. An oriented volume-averaged flow rate $< u_j >$ is defined as

$$< u_j > = \frac{1}{V}\sum_e \int_{V_e} u_j^e \, dV_e \tag{4.13}$$

where V is the volume of the computational domain for estimating $\mathbf{k}$. Similarly, an oriented

volume averaged pressure gradient $< \frac{\partial p}{\partial x_i} >$ is expressed as

$$< \frac{\partial p}{\partial x_i} >= \frac{1}{V} \sum_e \int_{V_e} \frac{\partial p_e}{\partial x_i} dV_e \tag{4.14}$$

The rock matrix of fractured rock is represented by a series of triangular matrix elements, whereas the embedded fractures are modeled by 1D segments between triangular elements. The volume of the fracture element is the fracture length scaled by its corelated fracture aperture. Finally, $\mathbf{k}$ can be estimated by

$$\begin{bmatrix} < \frac{\partial p}{\partial x} >^I & < \frac{\partial p}{\partial y} >^I & 0 & 0 \\ 0 & 0 & < \frac{\partial p}{\partial x} >^I & < \frac{\partial p}{\partial y} >^I \\ < \frac{\partial p}{\partial x} >^{II} & < \frac{\partial p}{\partial x} >^{II} & 0 & 0 \\ 0 & 0 & < \frac{\partial p}{\partial x} >^{II} & < \frac{\partial p}{\partial x} >^{II} \end{bmatrix} \begin{bmatrix} k_{xx} \\ k_{xy} \\ k_{yx} \\ k_{yy} \end{bmatrix} = \begin{bmatrix} < u_x >^I \\ < u_y >^I \\ < u_x >^{II} \\ < u_y >^{II} \end{bmatrix} \tag{4.15}$$

where *I*, *II* indicates two flow experiments in the *x* and *y* axis, respectively. Two basic fluid flow experiments are necessary to solve Eq. 4.15. The boundary conditions for the numerical experiments are shown in Fig. 4.6 (K. B. Min et al., 2004b; Min and Jing, 2003; Zhao et al., 2013; Zimmerman and Bodvarsson, 1996). Fig. 4.6a shows the boundary condition for the first experiment. The left boundary and right boundary are prescribed constant fluid pressures of 1 Pa and 0 Pa, respectively. The other boundaries are assigned to be impermeable. Similarly, Fig. 4.6b shows the other numerical experiment with the top and bottom boundary prescribed constant fluid pressure of 1 Pa and 0 Pa. The pressures in both experiments are solved numerically using the unified pipe network model.

4.3 Results

Case 1

In Case 1 as shown in Figs. 4.7 and 4.8, a single fracture whose length is 5 m is embedded into a rock matrix with a side length of 10 m. This case is used to show that the unified pipe network model can be admirably adapted to model a static steady flow through fractured rock. The rock matrix and the fracture are meshed using Gmsh (Geuzaine and Remacle, 2009). The rock matrix is discretized into 2D triangular elements. The fracture is meshed into 1D segments. To calculate the equivalent permeability tensor of fractured rock, two basic numerical experiments are necessary. The boundary conditions are prescribed on the outer boundaries of rock matrix following the way shown in Fig. 4.6.

The rock matrix permeability is 1.0×10^{-20} m^2. The fracture permeability is 1.0×10^{-15} m^2. The fracture aperture (hydraulic aperture) is 1.0×10^{-3} m. The hydraulic pressure distributions under Boundary I, Boundary II are shown Fig. 4.9. As shown in Fig. 4.9a, hydraulic

pressures in the *x* direction p_{xx} around the fracture vary much due to the existence of the fracture. In contrast, hydraulic pressures in the y direction p_{yy} do not change (Fig. 4.9b). Thus, k_{xx} varies while k_{yy} keeps constant when a horizontal fracture exists in the rock matrix.

To show how equivalent permeabilities change over fracture orientations, several fracture configurations for fracture orientations are made. The configurations are shown in Fig. 4.8. The fracture angle is at 0°, 15°, 30°, 45°, 60°, 75°, and 90°, respectively. The pressures for each subcase are shown Fig. 4.9. The extent of variations of p_{xx} around the fracture decreases as the fracture angle increases. In contrast, the extent of variations of p_{yy} increases. When fracture orientation is 45°, the extent of variations of p_{xx} and p_{yy} are equal as shown in Fig. 4.9g and 5.9h. When fracture orientation is 90°, the extent of variations of p_{xx} disappears and the extent of variations of p_{yy} increases to the maximum as shown in Fig. 4.9m and 4.9n.

The pressures shown Fig. 4.9 demonstrate that the unified pipe network can simulate the hydraulic pressure distribution. Using these pressures, equivalent permeabilities of fractured rock for each fracture configuration can be estimated using Eq. 4.15. The equivalent permeabilities k_{xx}, k_{yy}, k_{xy} and k_{yx} are shown in Fig. 4.10. From Fig. 4.10, we can see that k_{xx} decreases as fracture orientation increases as expected because the extent of variations of pressures around the fracture decrease gradually. In contrast, as fracture angle increases, k_{yy} also increases because the extent of variation of pressures around the fracture increase. For a symmetric permeability tensor, k_{xy} should be equal to k_{yx}. Using Eq. 4.15, there is a slight difference between k_{xy} and k_{yx} as shown in Fig. 4.10b. k_{xy} increases as fracture orientation increases between 0° and 45°. Between 0° and 45°, the variation in p_{yy} under Boundary I increase due to the existence of the fracture as its angle increase. Thus, k_{xy} increases as the fracture angle increases between 0° and 45°. Similarly, as fracture angle increase between 45° and 90°, the variation of p_{yy} under Boundary I decreases. Thus, k_{xy} decreases as the fracture angle increases between 45° and 90°.

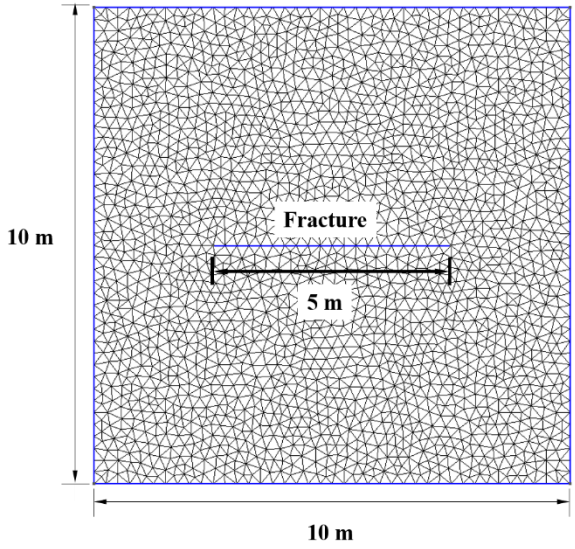

Fig. 4.7. Schematic diagram of Case 1 where a fracture with a length of 5 m is embedded into a rock matrix whose side length is 10 m.

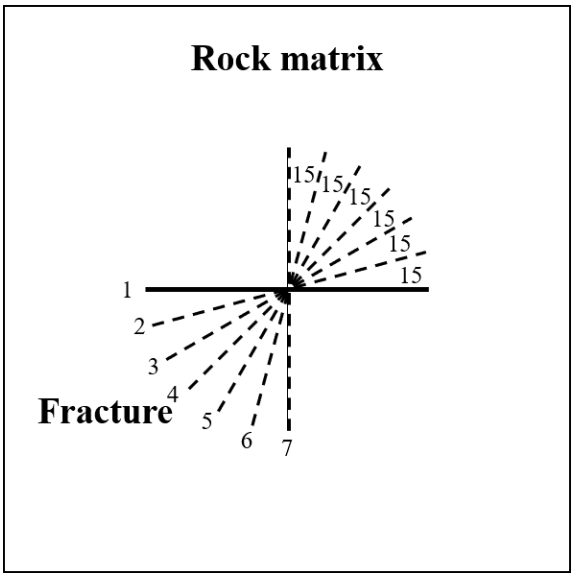

Fig. 4.8. Schematic diagram of fracture orientations. The fracture is at orientations of 0°, 15°, 30°, 45°, 60°, 75°, and 90°. Each fracture with a length of 5 m is embedded into rock matrix with a side length of 10 m.

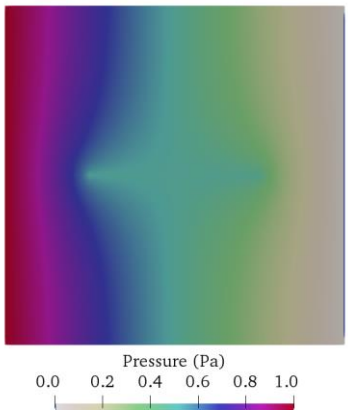 Pressure (Pa) 0.0 0.2 0.4 0.6 0.8 1.0	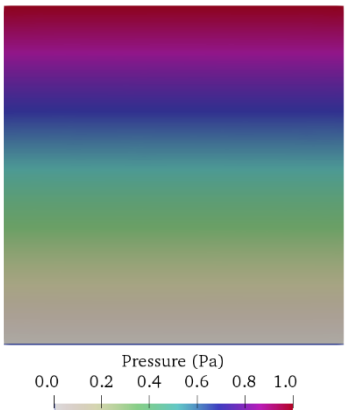 Pressure (Pa) 0.0 0.2 0.4 0.6 0.8 1.0
(a)	(b)
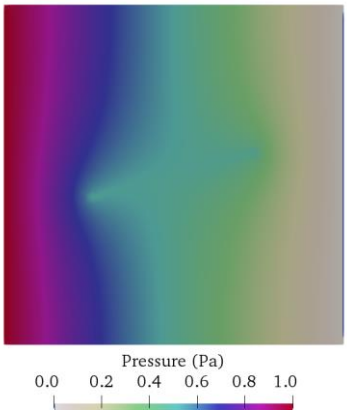 Pressure (Pa) 0.0 0.2 0.4 0.6 0.8 1.0	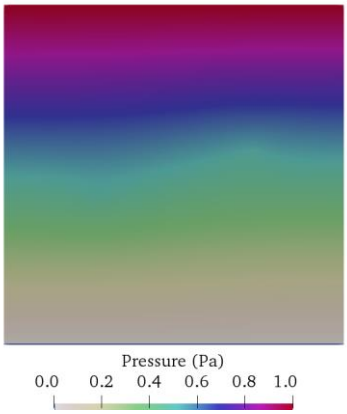 Pressure (Pa) 0.0 0.2 0.4 0.6 0.8 1.0
(c)	(d)
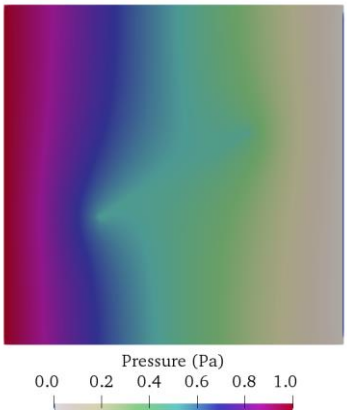 Pressure (Pa) 0.0 0.2 0.4 0.6 0.8 1.0	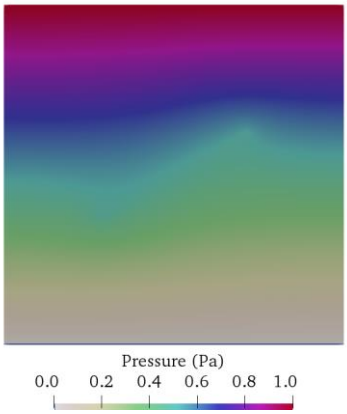 Pressure (Pa) 0.0 0.2 0.4 0.6 0.8 1.0
(e)	(f)

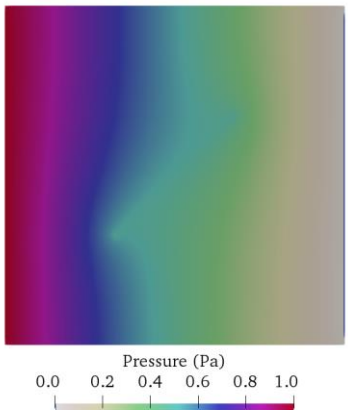 Pressure (Pa) 0.0 0.2 0.4 0.6 0.8 1.0	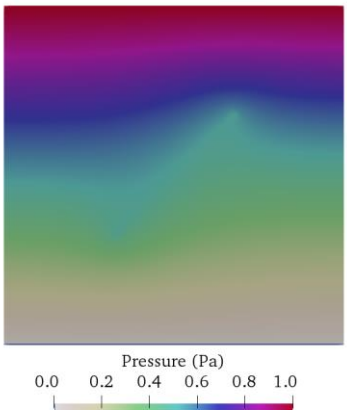 Pressure (Pa) 0.0 0.2 0.4 0.6 0.8 1.0
(g)	(h)
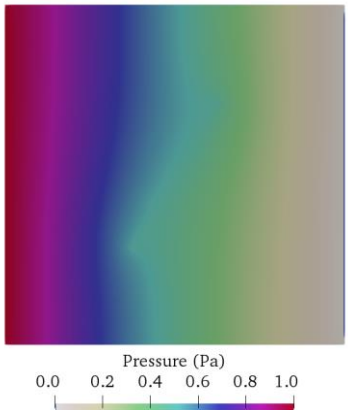 Pressure (Pa) 0.0 0.2 0.4 0.6 0.8 1.0	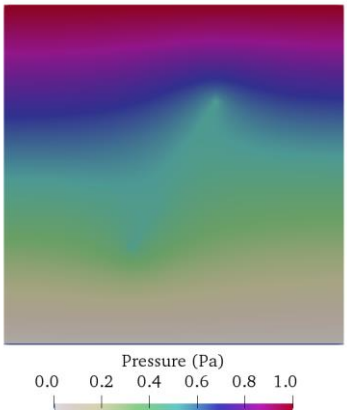 Pressure (Pa) 0.0 0.2 0.4 0.6 0.8 1.0
(i)	(j)
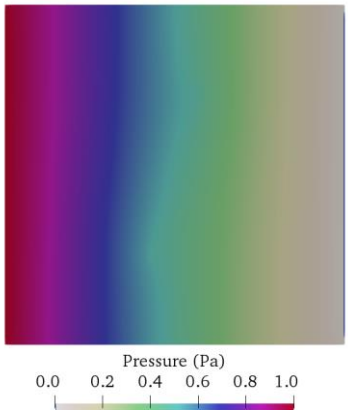 Pressure (Pa) 0.0 0.2 0.4 0.6 0.8 1.0	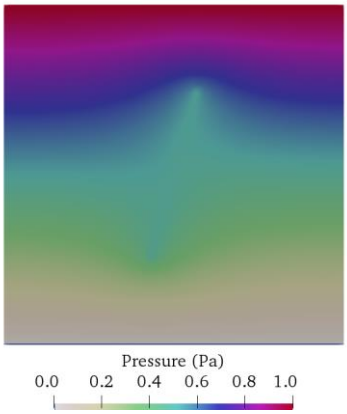 Pressure (Pa) 0.0 0.2 0.4 0.6 0.8 1.0
(k)	(l)

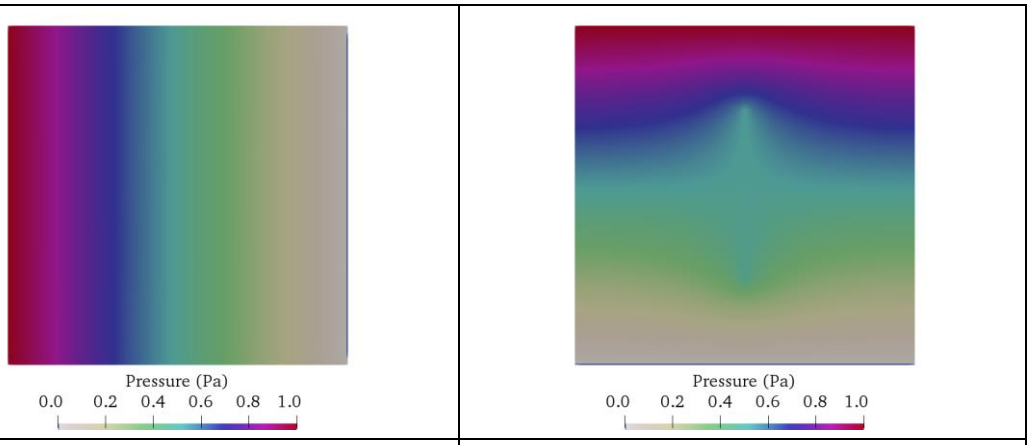

(m) (n)

Fig. 4.9. Pressure distributions in rock with a single fracture (shown in Fig. 4.8) which are under Boundary I and II, respectively.

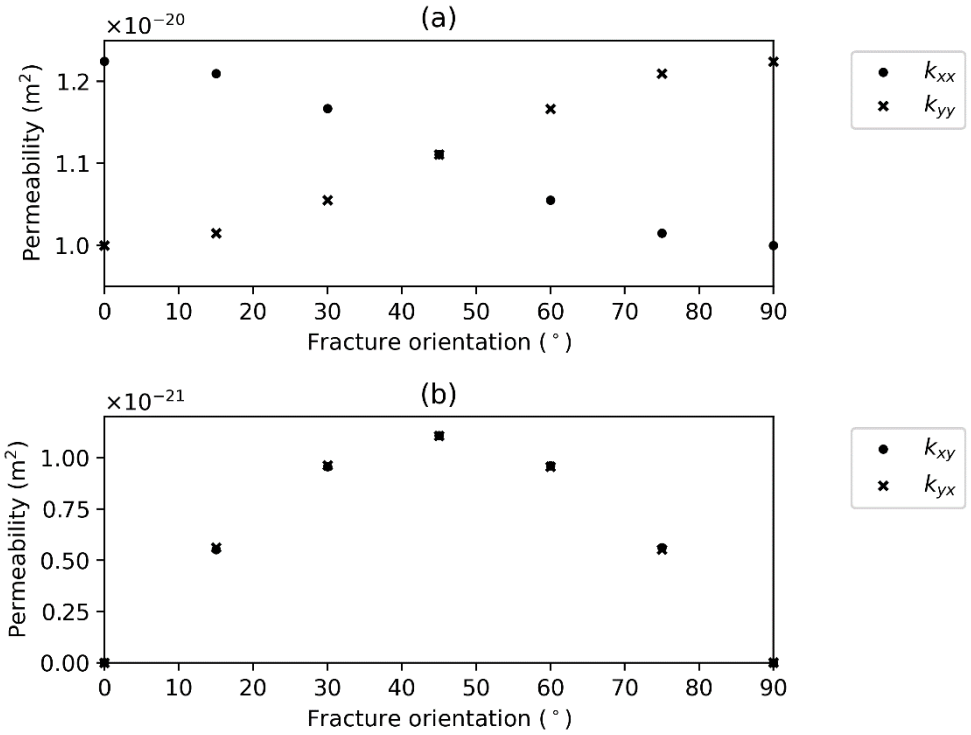

Fig. 4.10. Equivalent permeabilities of fractured rock with different fracture orientations which are shown in Fig. 4.8.

Case 2

In Case 2, the equivalent permeability tensor of the DFN model is calculated. Before calculating the equivalent permeability tensor, it is necessary to model hydraulic pressures in the DFN model using the unified pipe network model. The DFN modeling approach is used to

generate fractures in a cubic domain whose side length is 20 m. Fig. 4.11 shows 5 DFN models with varying fracture densities. P_{32} for each DFN model is 0.2, 0.4, 0.6, 0.8, 1.0 m^2/m^3, respectively. The fracture orientations are uniform distributed and fracture sizes follow the power-law distribution with the scaling exponent of 3.0 for each DFN model. The minimum, and maximum fracture length of each DFN model is 1.0 m and 200.0 m, respectively. The fracture aperture for each fracture is 1.0×10^{-3} m. The Fracture permeability for each fracture is 1.0×10^{-15} m^2. The rock matrix permeability is set to 1.0×10^{-20} m^2. Since our model can only handle a 2D model in which rock matrix is discretized into triangular elements and fractures are meshed into 1D segments, fractures in the crossing section which cuts through the 3D DFN model by plane at z = 10 m is considered. For example, Fig. 4.11a shows a 3D DFN model with P_{32} of 0.2 m^2/m^3. Fig. 4.11b shows a 2D fracture network in the cross section cutting through the DFN model by plane at z = 10 m. Using the 2D fracture networks shown in Figs. 4.11b, 4.11d, 4.11f, 4.11h, and 11j, the hydraulic pressures through fractured rocks are shown Fig. 4.12. Based on those pressures, the equivalent permeabilities of DFN models are shown in Fig. 4.13. It shows that k_{xx}, k_{yy}, k_{xy}, and k_{yx} increase as fracture densities increase though their increase rates are decreasing. As Fig. 4.13a, k_{xx}, k_{yy}, k_{xy}, k_{yx} for the DFN model (Fig. 4.11b) are 1.6×10^{-20} m^2, 1.04×10^{-20} m^2, -9.1×10^{-22} m^2, -9.9×10^{-22} m^2, respectively. Since k_{xx} and k_{yy} are different, the DFN model is anisotropic. k_{xy} and k_{yx} are negative. It shows that p_{xx} causes a negative effect in fluid flow in the y axis. However, for the DFN model as shown in Fig. 4.11j, k_{xx}, k_{yy}, k_{xy}, k_{yx} for the DFN model (Fig. 4.11b) are 2.9×10^{-20} m^2, 2.3×10^{-20} m^2, 1.9×10^{-21} m^2, 2.8×10^{-21} m^2, respectively. The k_{xx} and k_{yy} are nearly the same. It indicates that the DFN model is nearly isotropic. The k_{xy} and k_{yx} are positive, which indicates that p_{xx} contributes to fluid flowing in the y axis. As the fracture density increases, the anisotropic characteristic of the DFN model disappears.

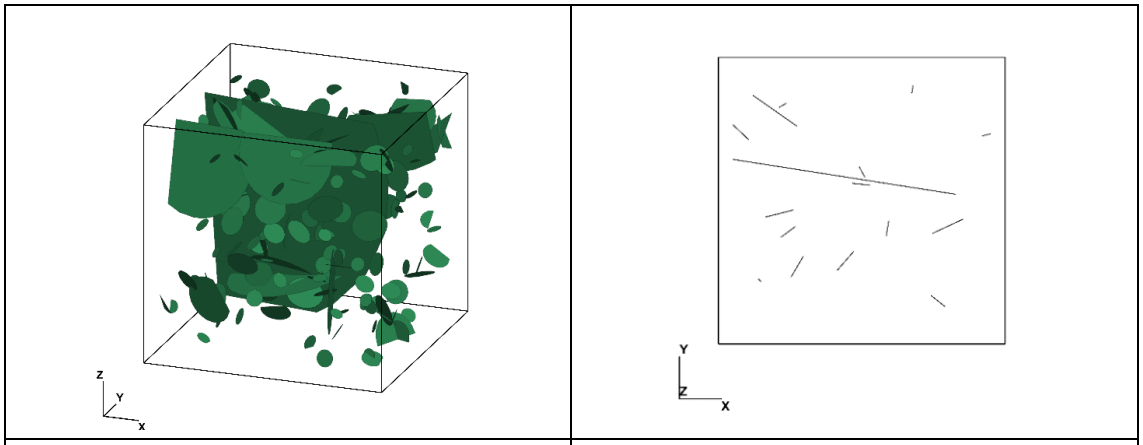

(a) (b)

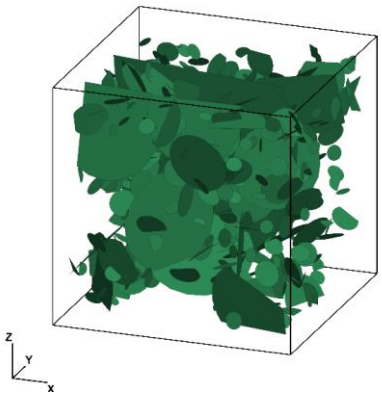	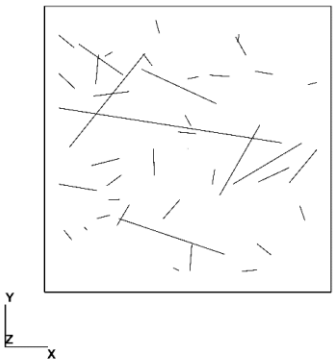
(c)	(d)
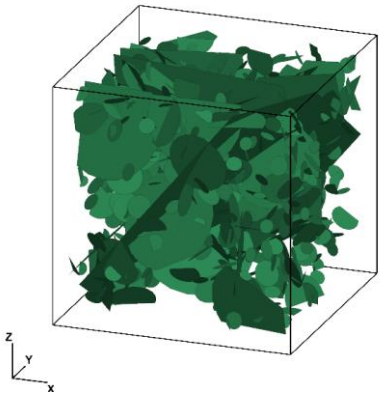	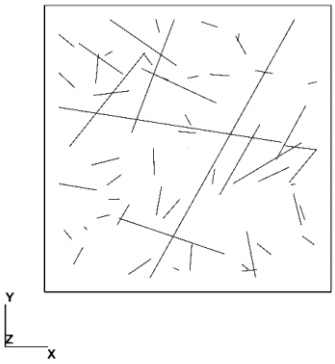
(e)	(f)
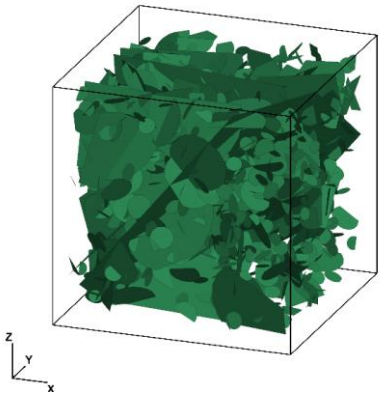	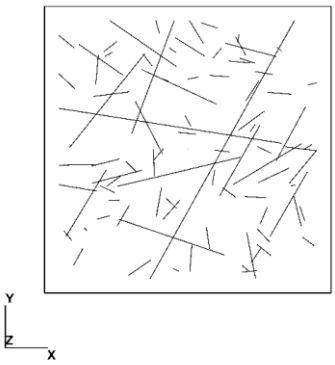
(g)	(h)

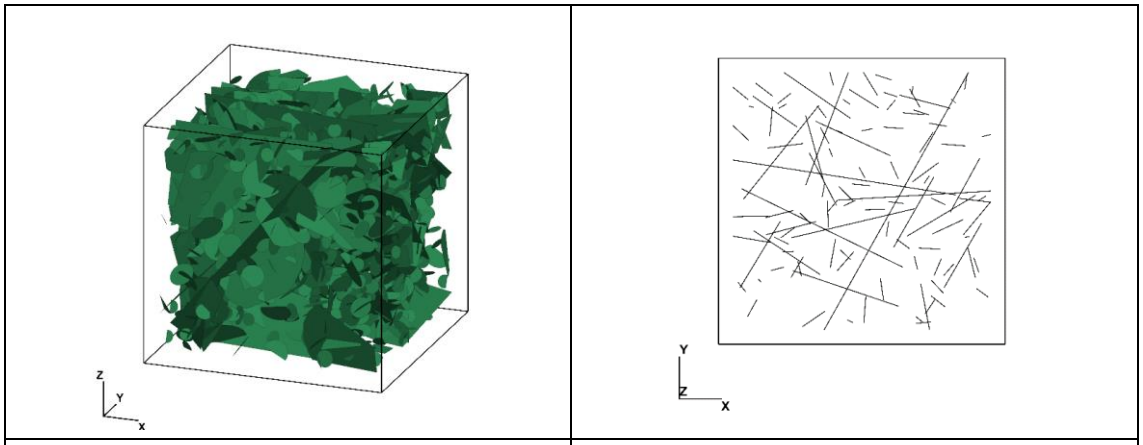

(i) (j)

Fig. 4.11. DFN models with different fracture densities (P_{32}) of 0.2, 0.4, 0.6, 0.8, 1.0 m^2/m^3, respectively.

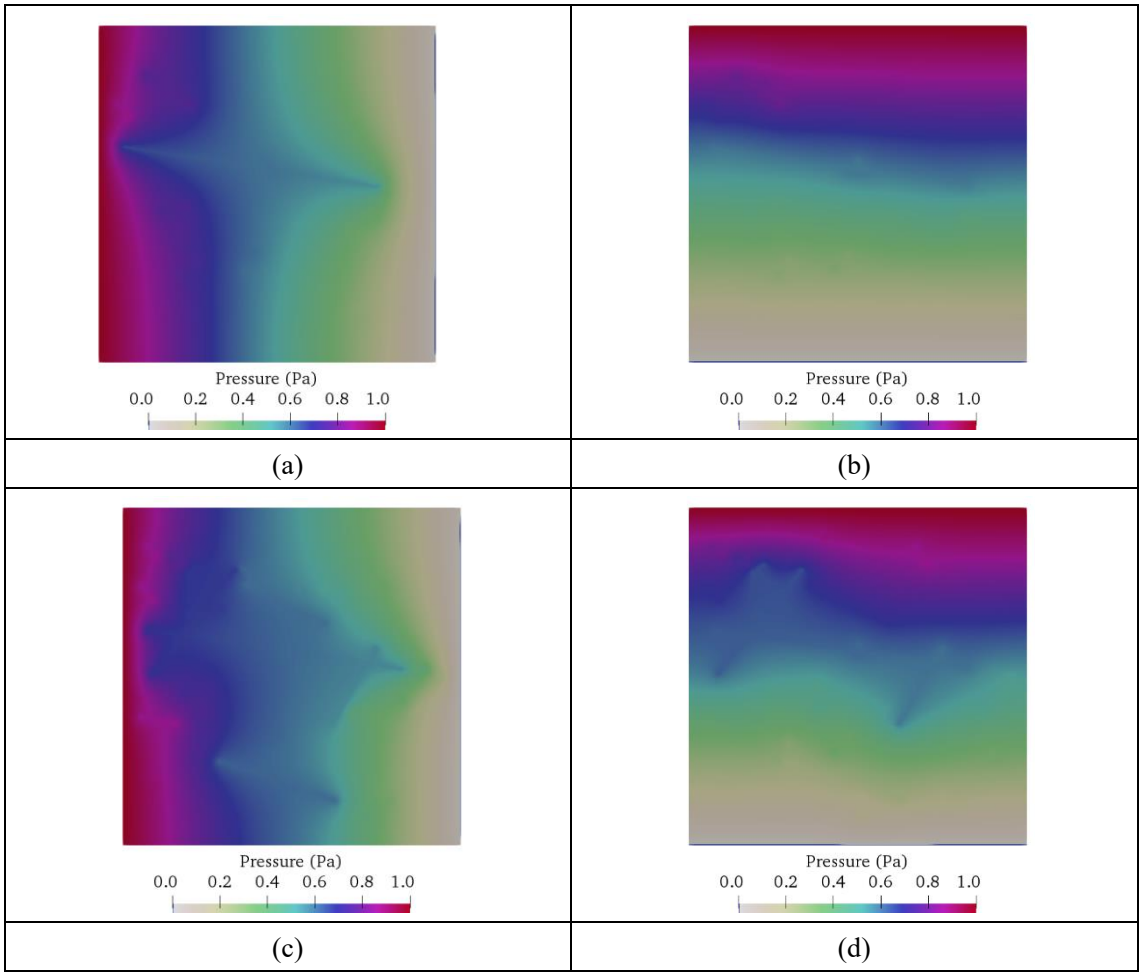

(a) (b)

(c) (d)

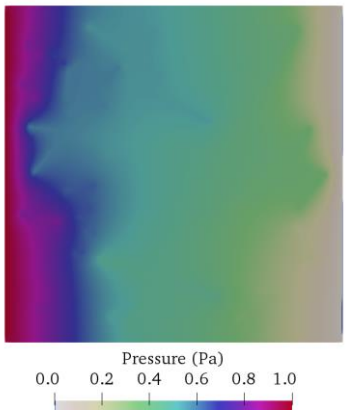

(e)

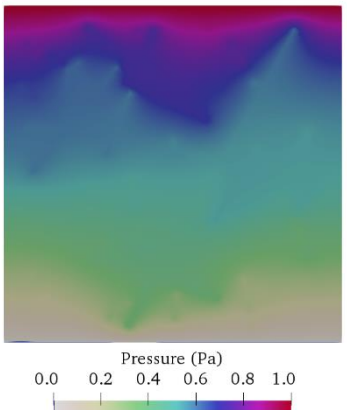

(f)

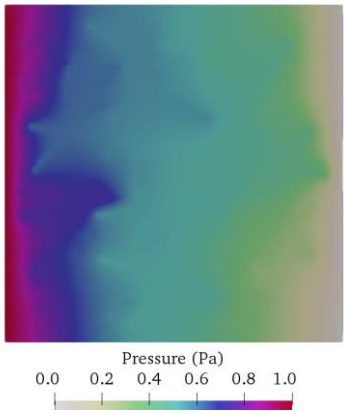

(g)

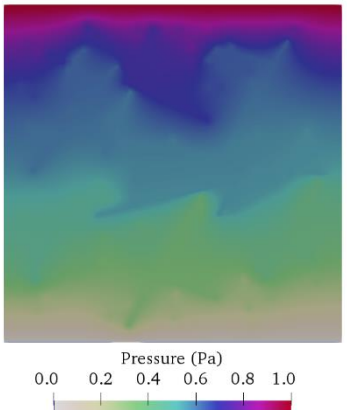

(h)

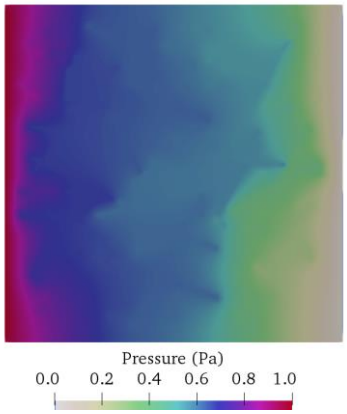

(i)

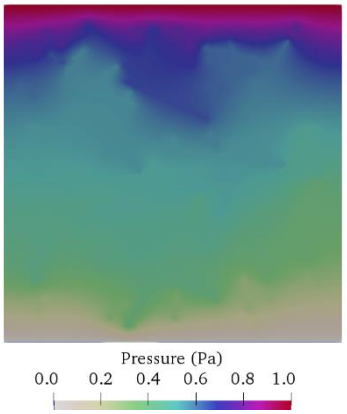

(j)

Fig. 4.12. Pressure distributions in the DFN models (shown in Fig. 4.11) which are under Boundary I and II, respectively.

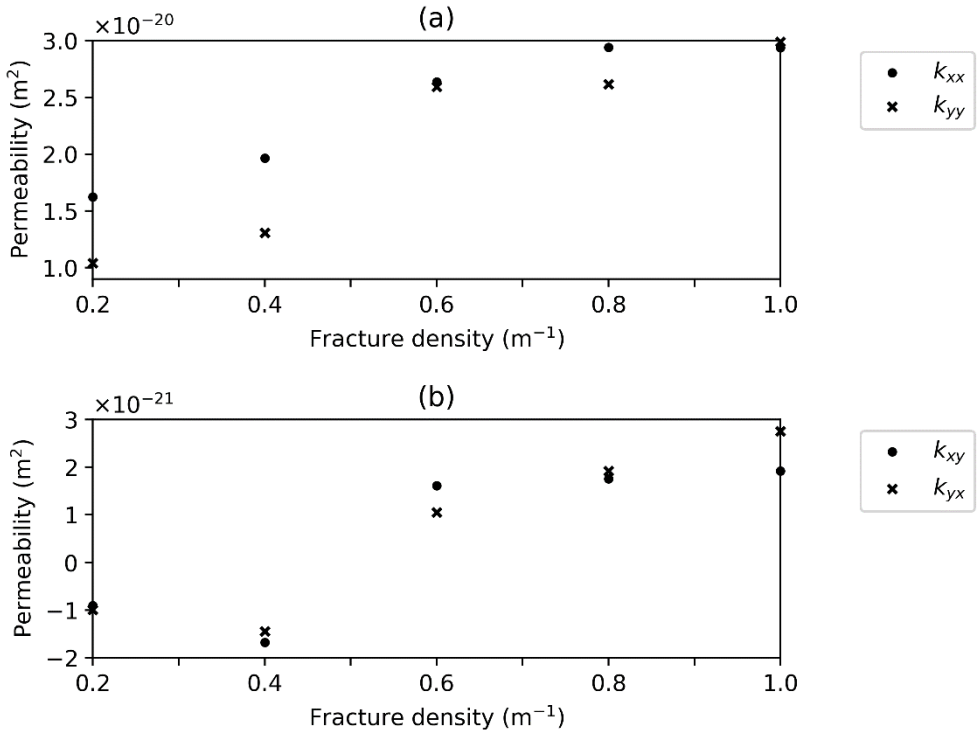

Fig. 4.13. Equivalent permeabilities of DFN models (Fig. 4.11) using pressure distributions (Fig. 4.12).

Case 3

A uniaxial compression test of a rock specimen is made to show that our proposed method can capture variations of equivalent permeabilities due to the initialization and propagation in intact rock under the uniaxial loading condition. The Y-Geo in which FEMDEM is embedded (Lisjak and Grasselli, 2014; Munjiza, 2004; Munjiza et al., 1995) is used. Table 4.1 shows the model parameters used in modeling the uniaxial compression test. The model and geometrical parameters are from Tatone and Grasselli (2015). The geometry and loading conditions of rock sample is shown in Fig. 4.14. The rock sample is loaded without two rigid platens in our analysis thus end effect on fracture initial and propagation in the rock sample may exist. The rock specimen with a height of 0.072 m, a width of 0.036 m is meshed into triangular matrix elements using Gmsh. The smallest mesh size is 7.5×10^{-4} m. Cohesive elements are inserted between two neighboring matrix elements. To ensure numerical stability of the explicit Euler integration scheme used in the FEMDEM fracture model, a small step size of 3.0×10^{-9} s is adopted. The total time steps are 150,000. The stress-strain curve of rock sample under compression test is shown in Fig. 4.15. The UCS is determined as 29.5 MPa. Four case studies, namely Methods 1, 2, 3 and 4, respectively, are carried out in Case 3. For all methods, a constant matrix permeability of 1.0×10^{-15} m^2 is assigned. In Method 1, a constant fracture permeability of 1.0×10^{-10} m^2

is assigned. A constant fracture aperture of 5 μm is assigned to each fracture which is developed in the intact rock. In Method 2, fracture permeability is calculated as Eq. 4.5 (a = 5 μm). In Methods 3 and 4, the fracture openings simulated from the FEMDEM fracture model are adopted. In Method 3, fracture permeability is calculated as Eq. 4.5 for each fracture. In Method 4, a constant fracture permeability of 1.0×10^{-10} m^2 are assigned.

Fig. 4.16 shows the progressive evolution of fracture initialization and propagation in intact rock as time step is 105,000, 110,000, 115,000, 120,000, and 125,000, respectively. The fractures start to develop when time step is 105000. The apertures are also shown in Fig. 4.16. The fracture openings which are modeled by the FEMDEM fracture model are regarded as the apertures. These apertures are used for Methods. 2 and 3 for estimating fracture permeability. The hydraulic pressures under Boundary I and Boundary II are shown in Fig. 4.17, respectively. Based on these pressures, the equivalent permeabilities are shown in Figs. 4.18 and 4.19. As Fig. 4.18 shows, both k_{xx} and k_{yy} increase as the progressive evolution of fractures in intact rock and their increase rates decrease. The increase rates indicate that fractures are finally developed as time steps increase. As Fig. 4.18a shows, both k_{xx} and k_{yy} calculated from Method 4 are the largest.

Table 4.1. Input parameters used in the FEMDEM fracture model for Case 3

Parameters	
Rock	
Height	0.072 m
Diameter	0.036 m
Density	1704 kg/m^3
Young's modulus	15 GPa
Poisson ratio	0.24
Friction coefficient	0.5
Viscous damping	7584 kg/(m·s)
Contact Penalty	1.5×10^{11} kg/s^2
Tangential Penalty	1.5×10^{10} kg/(m·s^2)
Cohesive element	
Friction	0.4
Cohesion	16.4 MPa
Tensile strength	1.3 MPa
Mode I fracture energy	3.8 J/m^2
Mode II fracture energy	84 J/m^2
Fracture penalty	7.5×10^{10} kg/(m·s^2)

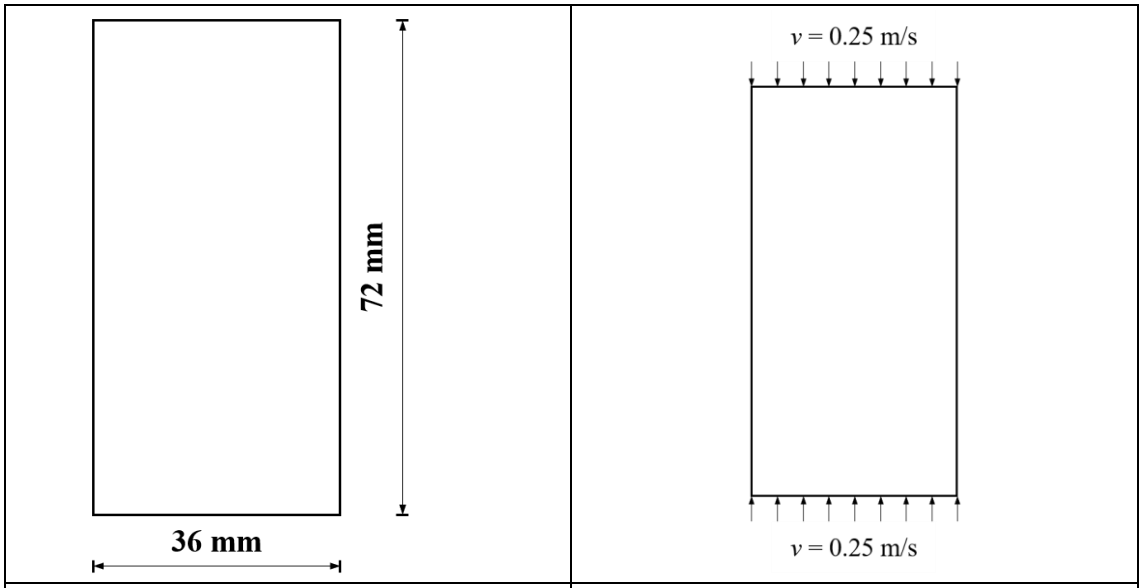

Fig. 4.14. Geometry (a) and loading conditions (b) for rock specimen under uniaxial compression test.

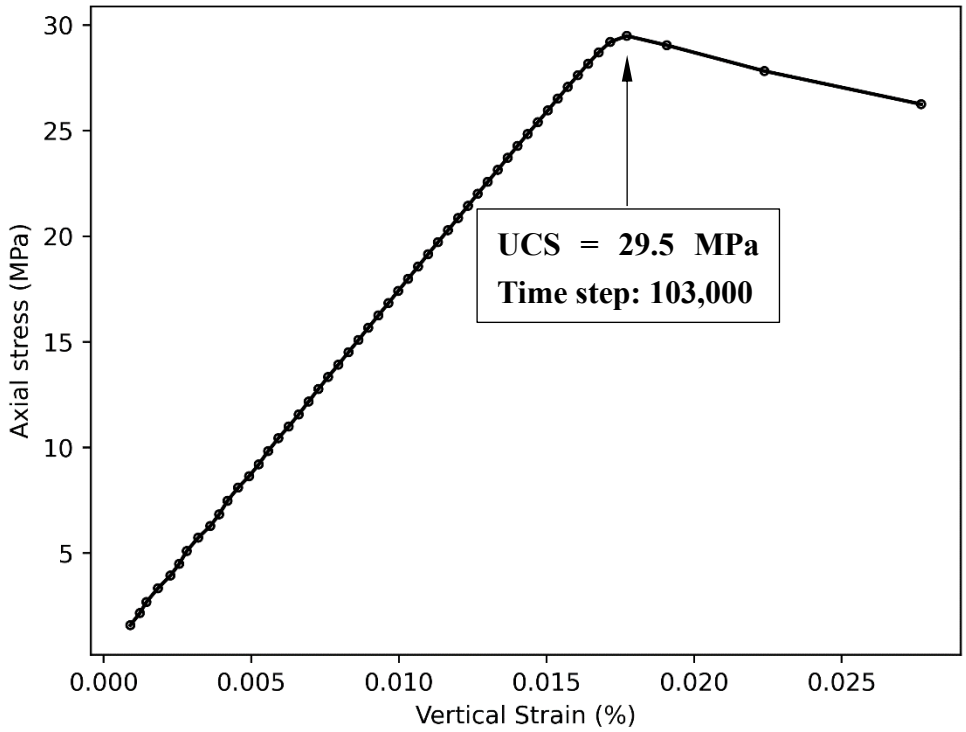

Fig. 4.15. Stress-strain curve of uniaxial compression test of rock sample.

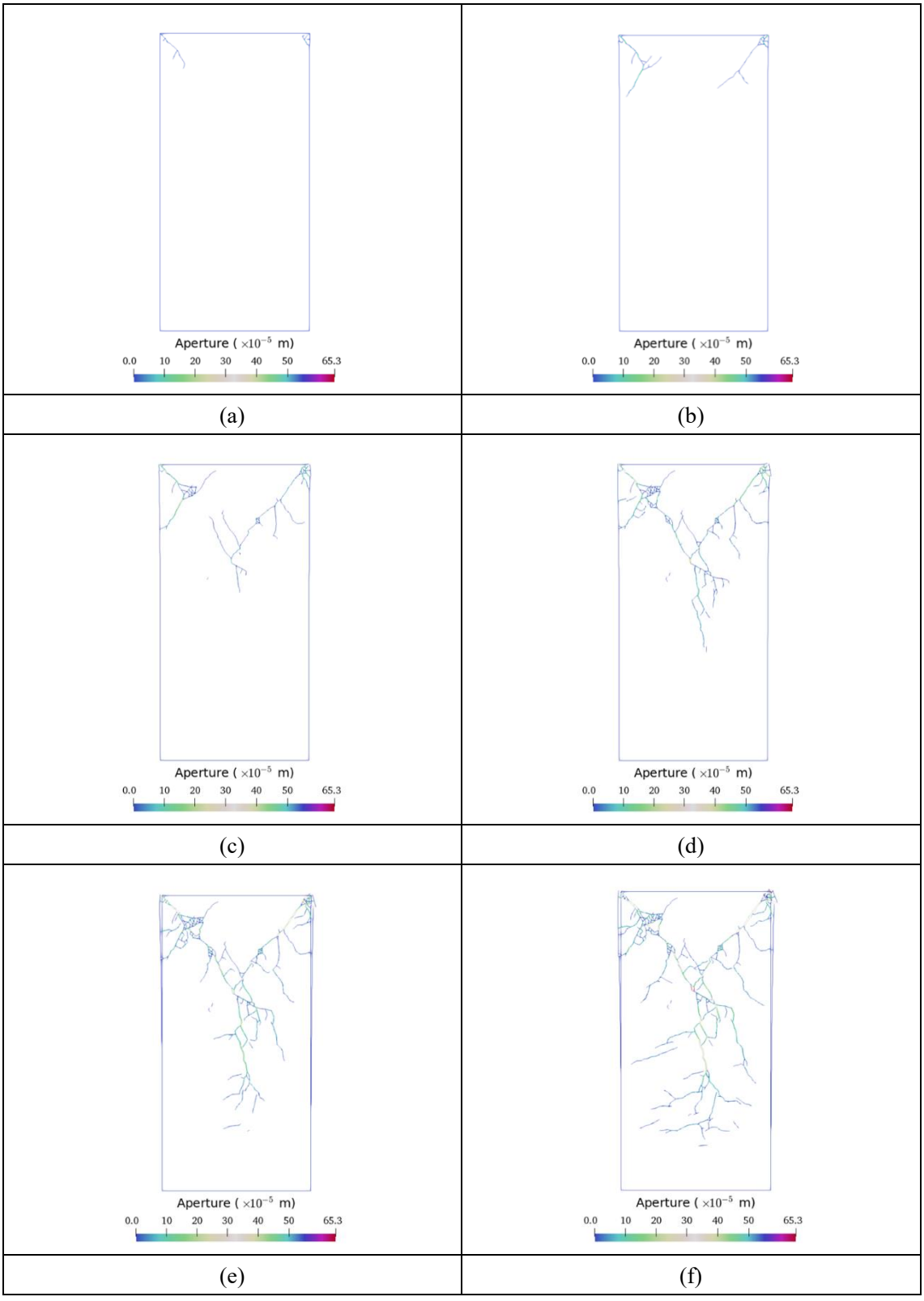

Fig. 4.16. The initialization and propagation of fractures that developed in intact rock. The fracture openings are regarded as fracture apertures.

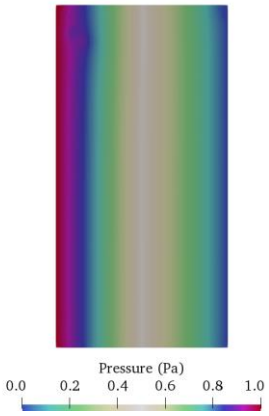 Pressure (Pa) 0.0 0.2 0.4 0.6 0.8 1.0	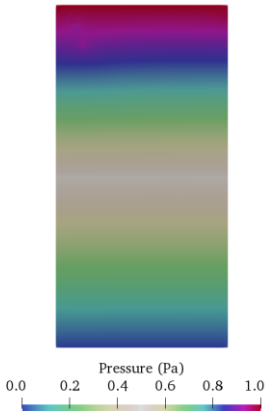 Pressure (Pa) 0.0 0.2 0.4 0.6 0.8 1.0
(a)	(b)
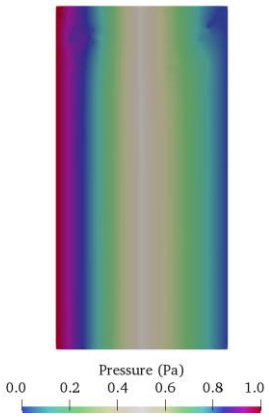 Pressure (Pa) 0.0 0.2 0.4 0.6 0.8 1.0	 Pressure (Pa) 0.0 0.2 0.4 0.6 0.8 1.0
(c)	(d)
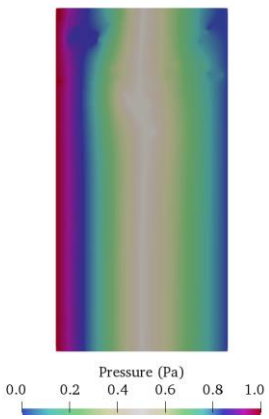 Pressure (Pa) 0.0 0.2 0.4 0.6 0.8 1.0	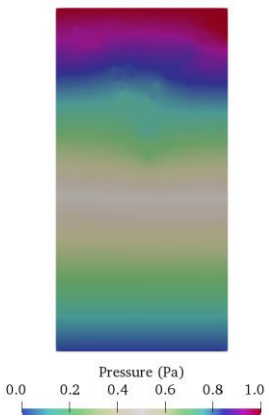 Pressure (Pa) 0.0 0.2 0.4 0.6 0.8 1.0
(e)	(f)

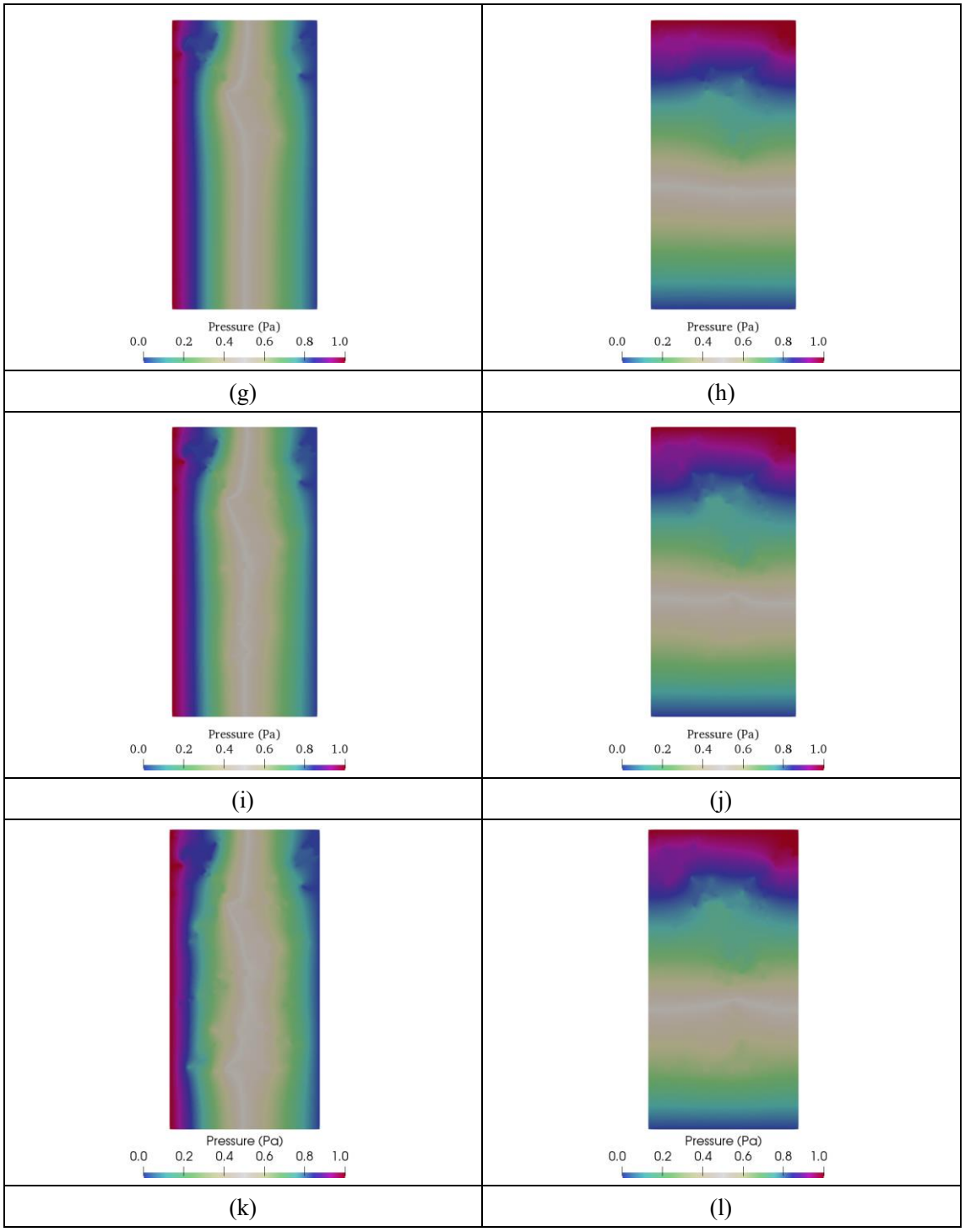

Fig. 4.17. Pressure distributions in fracture networks (Fig. 4.16) which are under Boundary I and II, respectively.

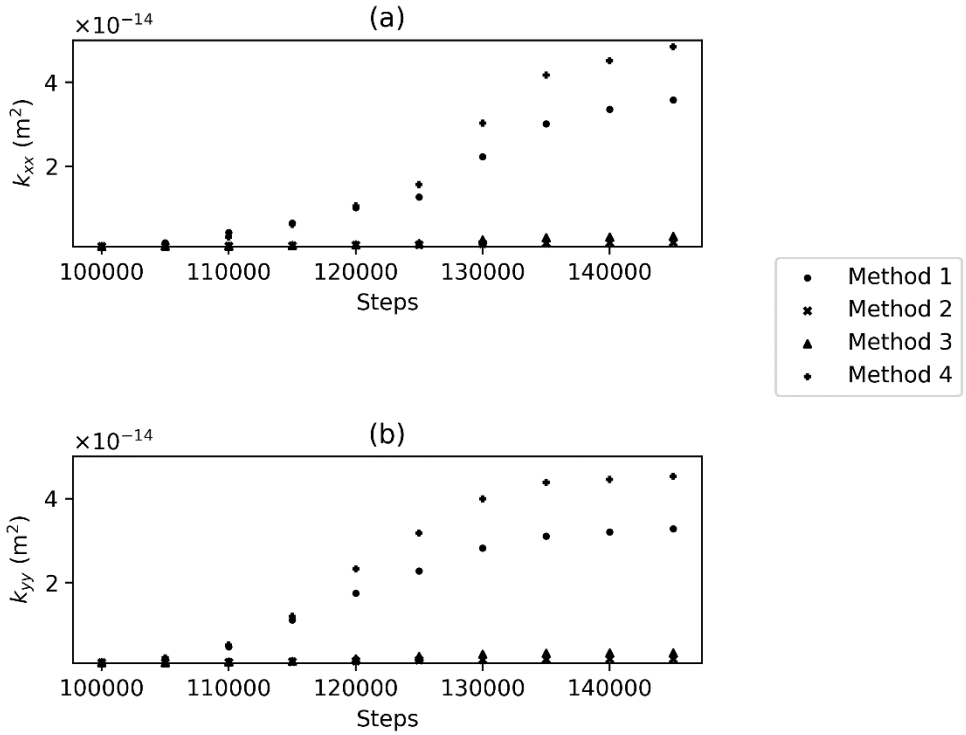

Fig. 4.18. k_{xx} and k_{yy} of fracture networks (Fig. 4.16) using the pressure distributions (Fig. 4.17). There are four methods with each method applying a different fracture permeability.

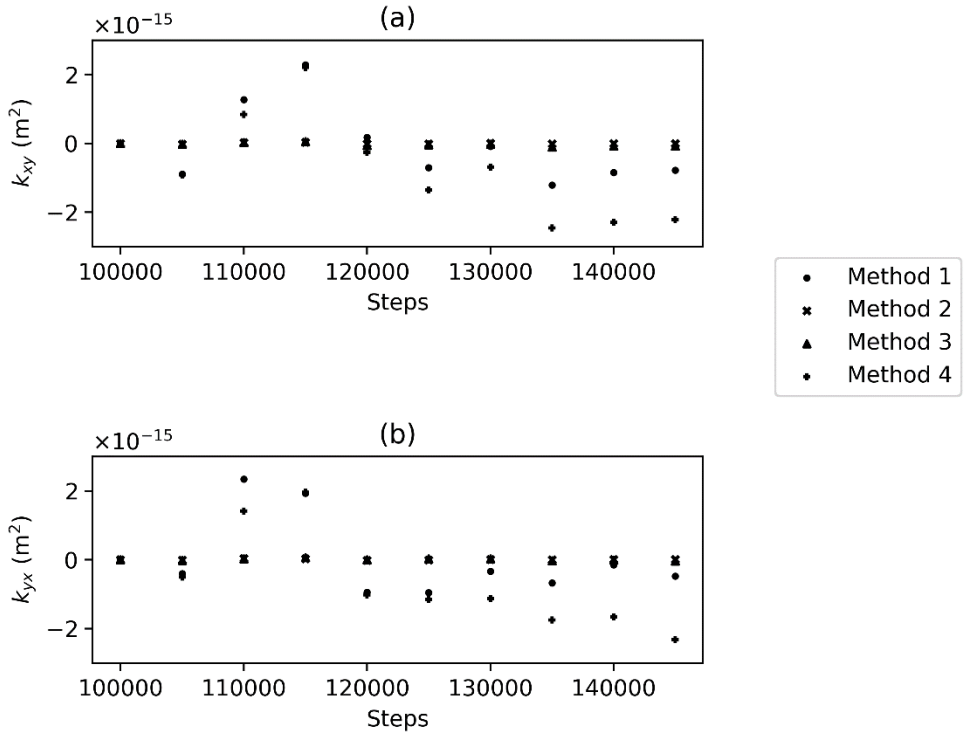

Fig. 4.19. k_{xy} and k_{yx} of fracture networks (Fig. 4.16) using pressure distributions (Fig. 4.17).

There are four methods with each method applies a different fracture permeability.

Case 4

An in-situ site numerical investigation of the initialization and propagation of fractures due to the tunnel excavation is carried out in the Case 4. The Horonobe Underground Research Laboratory (URL) , Japan carries out a high-level radioactive waste disposal project to characterize fractures in the EDZ around a tunnel that induced by an excavation at a depth of 350 m (Aoyagi et al., 2017; Aoyagi and Ishii, 2019; Ishii, 2017). Fig. 4.20 shows a schematic diagram of the tunnel in the mudstone sedimentary rock mass. The side length of the rock mass is 25 m. The tunnel is horseshoe-shaped with a height of 4.0 m and a span of 3.2 m. Fixed displacement boundary conditions are prescribed on the model boundaries. The initial horizontal and vertical in-situ stress is 4.81 MPa and 5.04 MPa. The Y-Geo in which FEMDEM is embedded (Lisjak and Grasselli, 2014; Munjiza, 2004; Munjiza et al., 1995) is used here. The input model parameters for the FEMDEM fracture model are listed in the Table 4.2. The input model parameters are partly from Aoyagi et al. (2017). The total number of time steps is 500,000. The time steps size is 1.0×10^{-8} s. The tunnel starts to be excavated at time step 30,000 and ends at time step 50,000. To ensure numerical stability, the Young's modulus of tunnel is reduced to zero gradually. The model is meshed by Gmsh (Geuzaine and Remacle, 2009). There are approximately 160,000 triangular elements in the model. The smallest element size is 0.01 m. An Excavation Damaged Zone (EDZ) is developed around the tunnel. To estimate the equivalent permeabilities of the EDZ, three representative blocks around the tunnel are chosen to represent the permeability of the EDZ. Fig. 4.21 shows a schematic diagram of representative blocks: Top Block, Right Block, and Bottom Block. Note that the blocks have different sizes. The effect of the block size on the equivalent permeability tensor is neglected in this chapter. The rock matrix permeability is 1.0×10^{-20} m^2. The fracture permeability of fractures that developed in the EDZ are not easy to calculate. In our case, several methods (namely Methods 1, 2, 3, 4, respectively), in which different fracture permeabilities are made. In the Method 1, a constant fracture permeability and a constant fracture aperture for each fracture is adopted. An average permeability of the EDZ is 5.0×10^{-13} m^2 (Aoyagi and Ishii, 2019). The fracture permeability is the same with that of the EDZ. An arbitrary fracture aperture 5.0×10^{-6} m is used. In the Method 2, fracture permeability is calculated from Eq. 4.5. *a* here is 5.0×10^{-6} m. For the Methods 3 and 4, fracture openings that calculated from the FEMDEM fracture model are adopted. The fracture permeabilities for Methods 3 and 4 are 2.08×10^{-12} m^2, and 5.0×10^{-13} m^2, respectively. The parameters for fracture aperture and fracture permeability are summarized in the Table 4.3.

The fracture initialization and propagation in the EDZ as time step is 200,000, 300,000, 400,000, and 500,000 is shown in Fig. 4.22. At time step 200,000, the extent of the EDZ is around

0.5 m (Fig. 4.22a). At time step 50,000, its extent is near 2.5 m (Fig. 4.22d). The fracture apertures which are used for estimating fracture permeability for each fracture are shown in Fig. 4.23. Figs. 4.24–4.27 show equivalent permeabilities in the Top, Right, and Bottom Block in the EDZ. Both k_{xx} and k_{yy} generally increase as time steps increase for all locations in the EDZ for all methods. In Method 3 in which fracture openings are assigned for fractures and fracture permeability is estimated from Eq. 4.5, k_{xx} and k_{yy} are the largest. As Figs. 4.24a, 4.25a, 4.26a, 4.27a show, the k_{xx} of the Top Block (Fig. 4.21) is the largest in three blocks. However, the k_{yy} of the Right Block (Fig. 4.21) are the largest as shown in Figs. 4.24b, 4.25b, 4.26b, 4.27b.

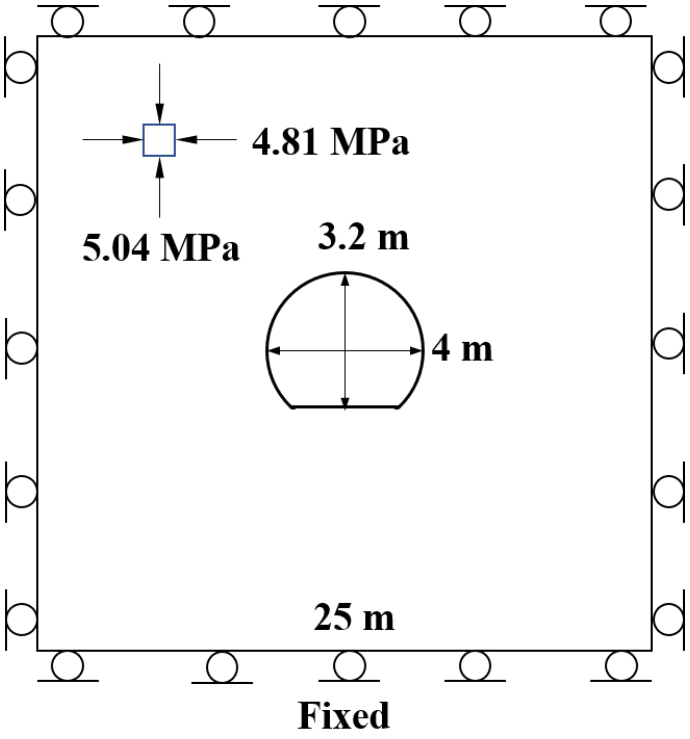

Fig. 4.20. Schematic layout of the tunnel in the mudstone sedimentary rock mass. The tunnel is horseshoe shaped with a height of 3.2 m and a span of 4.0 m. The side length of the rock mass is 25 m. Here, a small side length is adopted to avoid generating large numbers of elements. Fixed displacement boundary conditions are prescribed at the model boundaries. The horizontal, vertical initial in-situ stress is 4.81 MPa, 5.04 MPa, respectively.

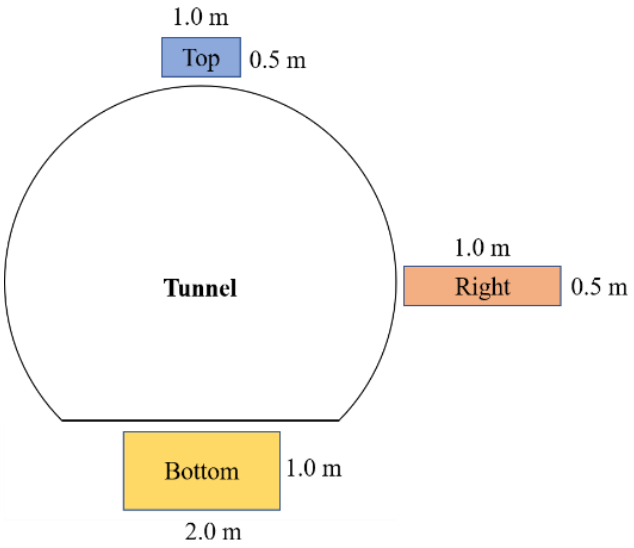

Fig. 4.21. Schematic layout of measuring locations around tunnel excavation. The equivalent permeabilities of Top Block, Right Block, and Bottom Block are chosen to represent the equivalent permeabilities of the EDZ that induced by tunnel excavation. The blocks have different sizes.

Table 4.2. Input parameters used in the FEMDEM fracture model for Case 4

Parameters	
Rock	
Density	1800 kg/m^3
Young's modulus	1.82 GPa
Poisson ratio	0.17
Friction coefficient	0.5
Viscous damping	361994 kg/(m·s)
Contact Penalty	1.82×10^{10} kg/s^2
Tangential Penalty	1.82×10^{9} kg/(m·s^2)
Cohesive element	
Friction	0.3054
Cohesion	2.87 MPa
Tensile strength	1.83 MPa
Mode I fracture energy	5 J/m^2
Mode II fracture energy	10 J/m^2
Fracture penalty	9.1×10^{9} kg/(m·s^2)

Table 4.3. The definition of permeability, aperture for fractures in the EDZ

Method	Aperture	Fracture permeability
Method 1	5.0×10^{-6} m	5.0×10^{-13} m^2
Method 2	5.0×10^{-6} m	2.08×10^{-12} m^2
Method 3	Fracture openings	Base on Eq. 4.5
Method 4	Fracture openings	5.0×10^{-13} m^2

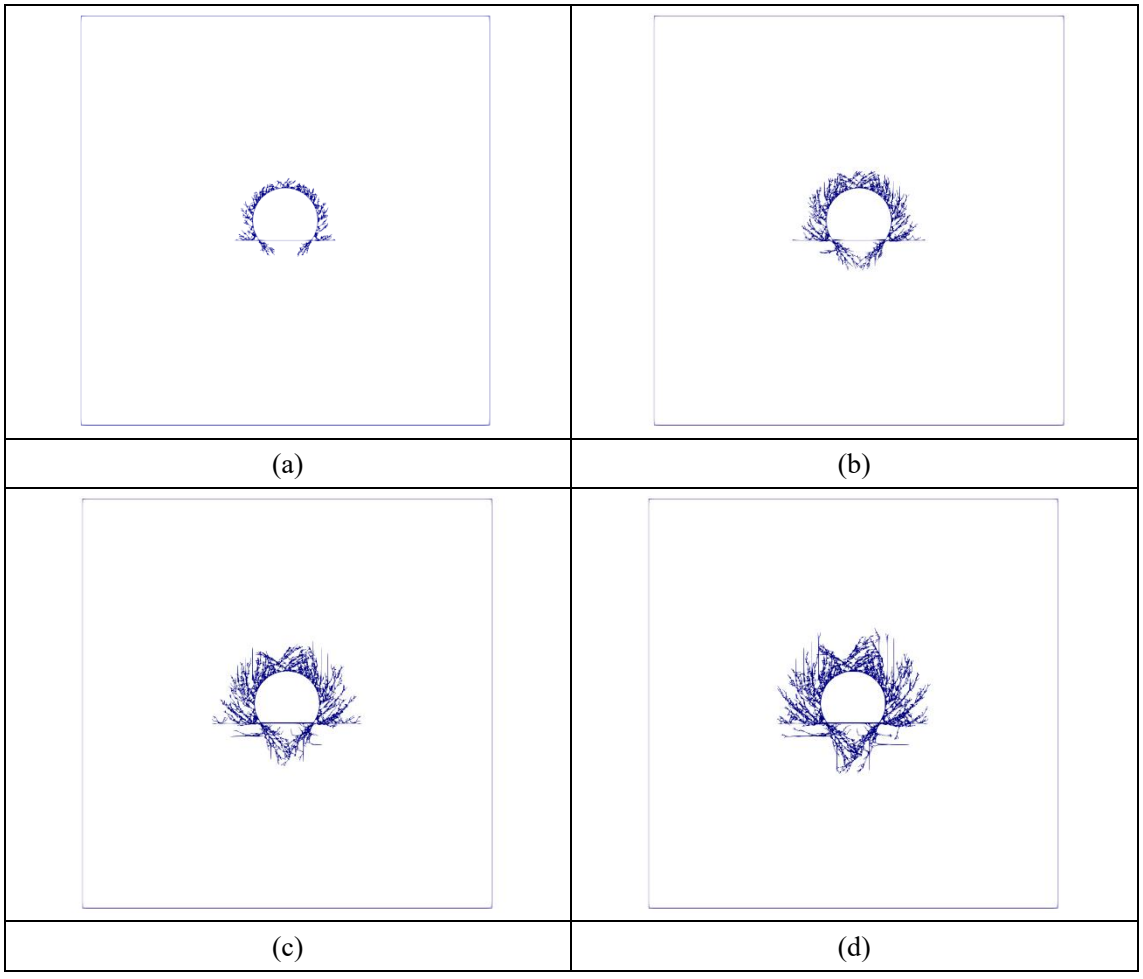

(a) (b) (c) (d)

Fig. 4.22. The initialization and propagation of fractures that induced by a tunnel excavation in the rock mass at time step 200,000, 300,000, 400,000, and 500,000, respectively.

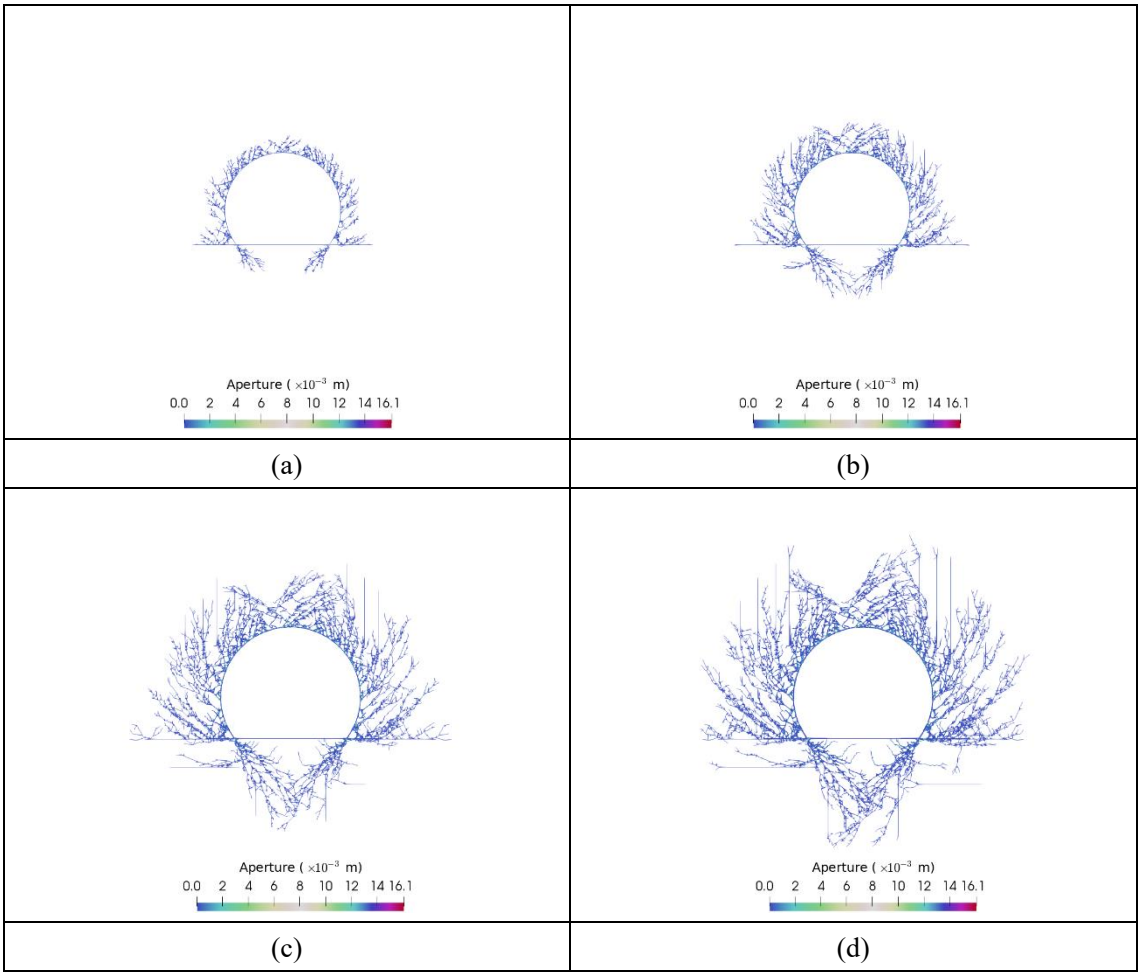

Fig. 4.23. Fracture apertures developed in the fracture networks (Fig. 4.22). Fracture openings modeled by the FEMDEM fracture model are regarded as fracture apertures.

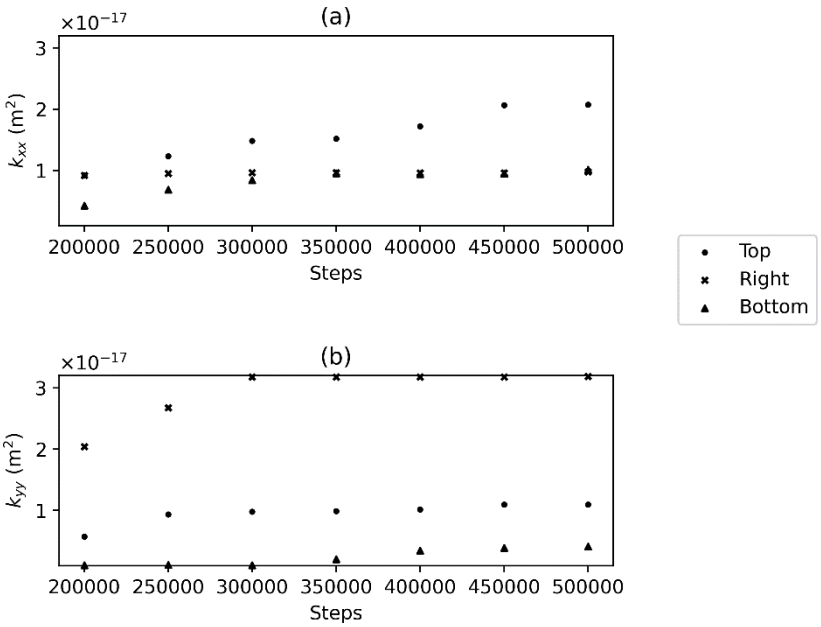

Fig. 4.24. Progressive evolution of k_{xx} and k_{yy} of Top Block, Right Block, and Bottom Block (Fig. 4.21) in the Method 1.

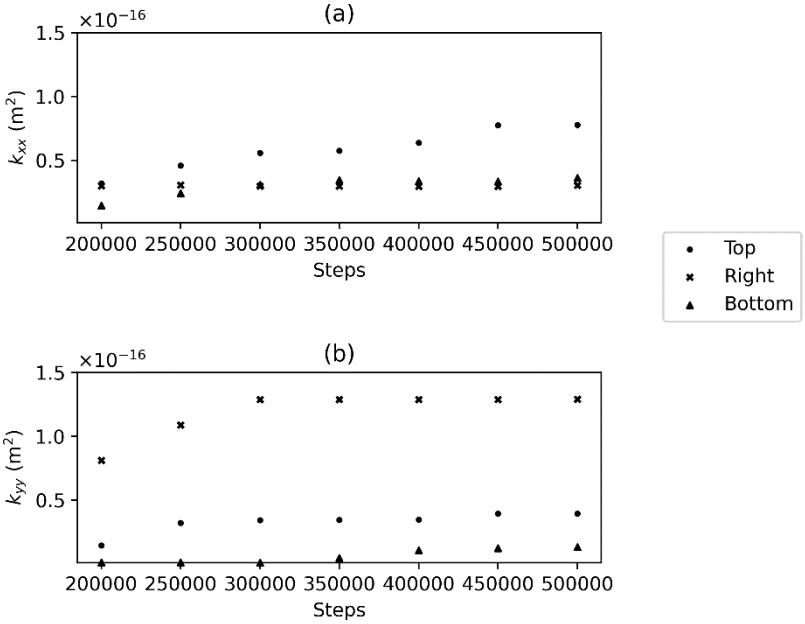

Fig. 4.25. Progressive evolution of k_{xx} and k_{yy} of Top Block, Right Block, and Bottom Block (Fig. 4.21) in the Method 2.

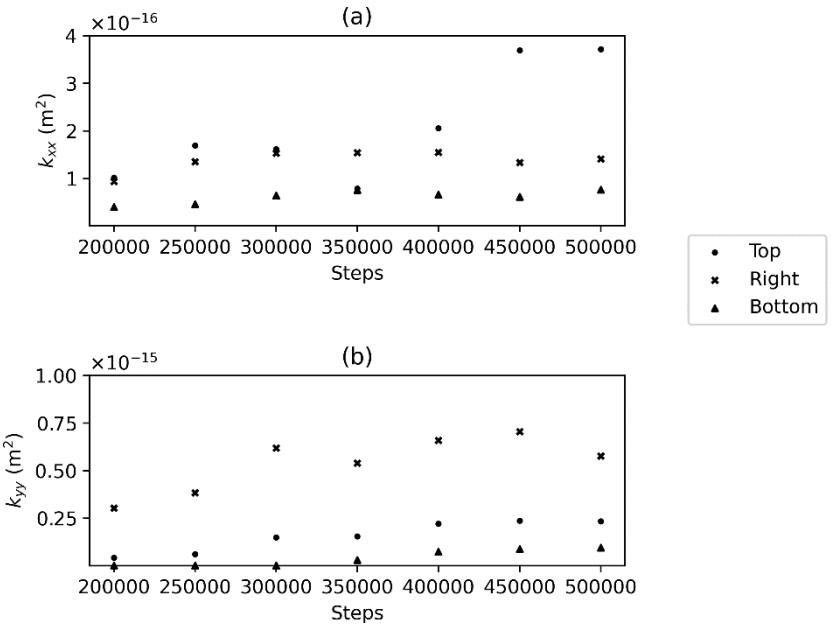

Fig. 4.26. Progressive evolution of k_{xx} and k_{yy} of Top Block, Right Block, and Bottom Block (Fig. 4.21) in the Method 3.

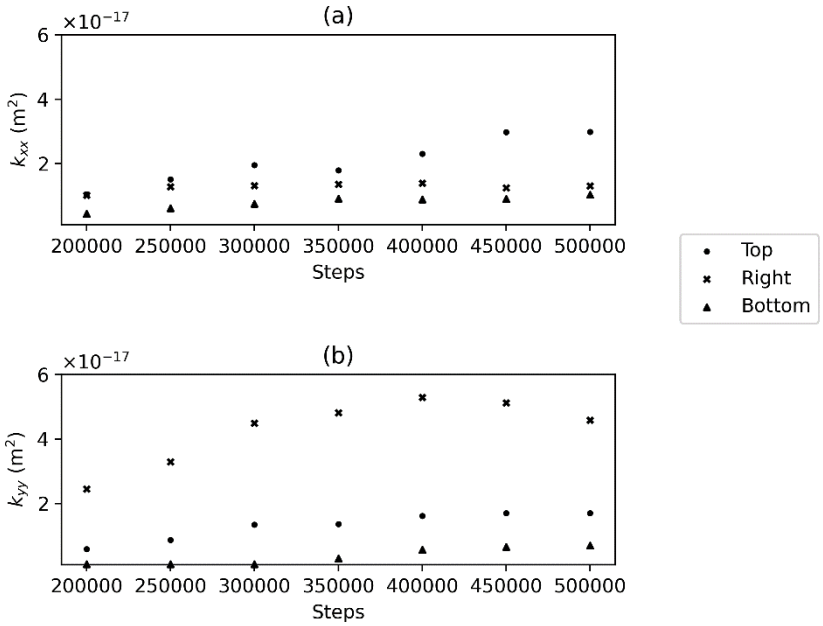

Fig. 4.27. Progressive evolution of k_{xx} and k_{yy} of Top Block, Right Block, and Bottom Block (Fig. 4.21) in the Method 4.

4.4 Discussion

The dynamic evolution of fractured rock permeability as a result of stress perturbations is

common in engineering practice especially for assessment of EDZ. The conventional numerical approach for modeling evolution of permeability of EDZ uses a continuum damage model with implicit representation of fractures (Rutqvist et al., 2009). The evolution of permeability is caused by aperture changes calculated from volumetric strain. Another approach is that EDZ is modeled by a DFN model where fractures are explicitly described. The permeability change comes from aperture changes estimated from empirical formula such as the Oda's crack tensor theory. Recently, predicting evolution of permeability based on a numerical modeling of fracture initialization and propagation in the EDZ have been also proposed. Shen et al. (2011) used FRACOD to model fracturing process in the EDZ and incorporated theoretical formulations to estimate its permeability change. The theoretical formulations are empirical and not accurate. Though fracture properties (e.g., lengths, apertures) are accurately described numerically, estimating equivalent permeability using theoretical formulations is not accurate. In this chapter, a modeling of equivalent permeability by a numerical model is proposed. In our scheme, not only fractures in the EDZ are modeled numerically but also equivalent permeability is solved numerically. Thus, the dynamic evolution of equivalent permeability is reliable.

In Case 3 and Case 4, we choose several configurations for estimating fracture permeability. The reason behind it is that it is hard to accurately estimate fracture permeability. A straightforward way to assign fracture permeability is assuming a known value is assigned to each fracture. The value can be measured through laboratory tests, in-situ measurements, or follows statistical distributions. Another way is establishing empirical relationships between fracture permeability and fracture aperture. The method is still questionable because it is not easy to define fracture aperture for fractures that are modeled by numerical methods. Thus, it is still a challenging problem to accurately estimate fracture permeability which is necessary for modeling fluid flow through fracture rock.

Several limitations still exist in our scheme. The definition of fracture aperture in the fracture network is still problematic. The fracture openings which are estimated from the FEMDEM are assumed as fracture apertures in this chapter. However, there are still other possible definitions of fracture apertures. For example, fracture aperture can be estimated by summing fracture opening and shear displacements. Using different definitions of fracture apertures, equivalent permeabilities may vary. Another problem is that equivalent permeability may vary block sizes. In the future, such effect needs further investigations.

4.5 Conclusion

In this chapter, the unified pipe network and the FEMDEM fracture model were jointly combined to estimate the equivalent permeability of the fractured rock mass. The unified pipe network used matrix pipes which represent the 2D rock matrix and fracture pipes which represent

the 1D fractures. The FEMDEM fracture model was used to characterize the initialization and propagation of fractures in the rock mass. To validate our proposed model, four representative cases were carried out. In the first case, the equivalent permeability of a rock mass in which a single fracture was embedded was estimated. The effect of fracture orientations on the permeability was also studied. The second case was a fractured rock where multiple fractures were generated by the DFN modeling approach. The effect of fracture density on the equivalent permeability was studied. Another case was an intact rock under a uniaxial compression test. The last case an in-situ site numerical investigation of the initialization and propagation of fractures due to the tunnel excavation. These cases showed possibilities of the applicability of our proposed model in estimating the permeability of fractured rock in engineering practice.

References

Amaziane, B., Hontans, T., Koebbe, J. V., 2001. Equivalent permeability and simulation of two-phase flow in heterogeneous porous media. Comput. Geosci. 5, 279–300. https://doi.org/10.1023/A:1014508622020

Aoyagi, K., Ishii, E., 2019. A Method for Estimating the Highest Potential Hydraulic Conductivity in the Excavation Damaged Zone in Mudstone. Rock Mech. Rock Eng. 52, 385–401. https://doi.org/10.1007/s00603-018-1577-z

AOYAGI, K., ISHII, E., ISHIDA, T., 2017. Field Observations and Failure Analysis of an Excavation Damaged Zone in the Horonobe Underground Research Laboratory. J. MMIJ 133, 25–33. https://doi.org/10.2473/journalofmmij.133.25

Baghbanan, A., Jing, L., 2007. Hydraulic properties of fractured rock masses with correlated fracture length and aperture. Int. J. Rock Mech. Min. Sci. 44, 704–719. https://doi.org/10.1016/j.ijrmms.2006.11.001

Barenblatt, G.., Zheltov, I.., Kochina, I.., 1960. Basic concepts in the theory of seepage of homogeneous liquids in fissured rocks [strata]. J. Appl. Math. Mech. 24, 1286–1303. https://doi.org/10.1016/0021-8928(60)90107-6

Dershowitz, W.S., Fidelibus, C., 1999. Derivation of equivalent pipe network analogues for three-dimensional discrete fracture networks by the boundary element method. Water Resour. Res. 35, 2685–2691. https://doi.org/10.1029/1999WR900118

Geuzaine, C., Remacle, J.F., 2009. Gmsh: A 3-D finite element mesh generator with built-in pre- and post-processing facilities. Int. J. Numer. Methods Eng. 79, 1309–1331. https://doi.org/10.1002/nme.2579

Heydari, A., Jalali, S.E., Noroozi, M., 2018. Developing a 3D stochastic discrete fracture network model for hydraulic analyses, International Journal of Mining and Geo-Engineering. University of Tehran. https://doi.org/10.22059/IJMGE.2018.244675.594704

Ishii, E., 2017. Preliminary assessment of the highest potential transmissivity of fractures in fault zones by core logging. Eng. Geol. 221, 124–132. https://doi.org/10.1016/j.enggeo.2017.02.026

Karimi-Fard, M., Firoozabadi, A., 2001. Numerical Simulation of Water Injection in 2D Fractured Media using Discrete-Fracture Model, in: Proceedings - SPE Annual Technical Conference and Exhibition. Society of Petroleum Engineers (SPE), pp. 2487–2502. https://doi.org/10.2118/71615-ms

Lang, P.S., Paluszny, A., Zimmerman, R.W., 2014. Permeability tensor of three-dimensional fractured porous rock and a comparison to trace map predictions. J. Geophys. Res. Solid Earth 119, 6288–6307. https://doi.org/10.1002/2014JB011027

Lei, Q., Latham, J.P., Xiang, J., Tsang, C.F., 2017. Role of natural fractures in damage evolution around tunnel excavation in fractured rocks. Eng. Geol. 231, 100–113. https://doi.org/10.1016/j.enggeo.2017.10.013

Li, S.C., Xu, Z.H., Ma, G.W., 2014. A Graph-theoretic Pipe Network Method for water flow simulation in discrete fracture networks: GPNM. Tunn. Undergr. Sp. Technol. 42, 247–263. https://doi.org/10.1016/j.tust.2014.03.012

Lisjak, A., Grasselli, G., 2014. A review of discrete modeling techniques for fracturing processes in discontinuous rock masses. J. Rock Mech. Geotech. Eng. https://doi.org/10.1016/j.jrmge.2013.12.007

Lisjak, A., Grasselli, G., Vietor, T., 2014. Continuum-discontinuum analysis of failure mechanisms around unsupported circular excavations in anisotropic clay shales. Int. J. Rock Mech. Min. Sci. 65, 96–115. https://doi.org/10.1016/j.ijrmms.2013.10.006

Liu, C., Kubo, T., Lu, L., Koike, K., Zhu, W., 2019. Spatial Simulation and Characterization of Three-Dimensional Fractures in Gejiu tin District, Southwest China, Using GEOFRAC. Nat. Resour. Res. 28, 99–108. https://doi.org/10.1007/s11053-018-9381-8

Mahabadi, O.K., Lisjak, A., Munjiza, A., Grasselli, G., 2012. Y-Geo: New Combined Finite-Discrete Element Numerical Code for Geomechanical Applications. Int. J. Geomech. 12, 676–688. https://doi.org/10.1061/(asce)gm.1943-5622.0000216

Min, K.-B., Jing, L., Stephansson, O., 2004. Determining the equivalent permeability tensor for fractured rock masses using a stochastic REV approach: Method and application to the field data from Sellafield, UK. Hydrogeol. J. 12, 497–510. https://doi.org/10.1007/s10040-004-0331-7

Min, K.B., Jing, L., 2003. Numerical determination of the equivalent elastic compliance tensor for fractured rock masses using the distinct element method. Int. J. Rock Mech. Min. Sci. 40, 795–816. https://doi.org/10.1016/S1365-1609(03)00038-8

Min, K.B., Jing, L., Stephansson, O., 2004a. Determining the equivalent permeability tensor for fractured rock masses using a stochastic REV approach: Method and application to the field data from Sellafield, UK. Hydrogeol. J. 12, 497–510. https://doi.org/10.1007/s10040-004-0331-7

Min, K.B., Jing, L., Stephansson, O., 2004b. Determining the equivalent permeability tensor for fractured rock masses using a stochastic REV approach: Method and application to the field data from Sellafield, UK. Hydrogeol. J. 12, 497–510. https://doi.org/10.1007/s10040-004-0331-7

Munjiza, A., 2004. The Combined Finite-Discrete Element Method, The Combined Finite-Discrete Element Method. John Wiley & Sons, Ltd, Chichester, UK. https://doi.org/10.1002/0470020180

Munjiza, A., Owen, D.R.J., Bicanic, N., 1995. A combined finite-discrete element method in transient dynamics of fracturing solids. Eng. Comput. 12, 145–174. https://doi.org/10.1108/02644409510799532

Oda, M., 1985. Permeability tensor for discontinuous rock masses. Géotechnique 35, 483–495. https://doi.org/10.1680/geot.1985.35.4.483

Priest, S.D., 1993. Discontinuity Analysis for Rock Engineering, Discontinuity Analysis for Rock Engineering. Springer Netherlands. https://doi.org/10.1007/978-94-011-1498-1

Pruess, K., Narasimhan, T., 1982. A practical method for modeling fluid and heat flow in fractured porous media.

Pruess, K., Oldenburg, C.M., Moridis, G.J., 1999. TOUGH2 User's Guide Version 2.

Ren, F., Ma, G., Wang, Y., Li, T., Zhu, H., 2017. Unified pipe network method for simulation of water flow in fractured porous rock. J. Hydrol. 547, 80–96. https://doi.org/10.1016/j.jhydrol.2017.01.044

Renard, P., De Marsily, G., 1997. Calculating equivalent permeability: A review. Adv. Water Resour. https://doi.org/10.1016/s0309-1708(96)00050-4

Rutqvist, J., Bäckström, A., Chijimatsu, M., Feng, X.T., Pan, P.Z., Hudson, J., Jing, L., Kobayashi, A., Koyama, T., Lee, H.S., Huang, X.H., Rinne, M., Shen, B., 2009. A multiple-code simulation study of the long-term EDZ evolution of geological nuclear waste repositories. Environ. Geol. 57, 1313–1324. https://doi.org/10.1007/s00254-008-1536-1

Sævik, P.N., Berre, I., Jakobsen, M., Lien, M., 2013. A 3D Computational Study of Effective Medium Methods Applied to Fractured Media. Transp. Porous Media 100, 115–142. https://doi.org/10.1007/s11242-013-0208-0

Schrauf, T.W., Evans, D.D., 1986. Laboratory Studies of Gas Flow Through a Single Natural Fracture. Water Resour. Res. 22, 1038–1050. https://doi.org/10.1029/WR022i007p01038

Shen, B., Stephansson, O., Rinne, M., Amemiya, K., Yamashi, R., Toguri, S., Asano, H., 2011. FRACOD Modeling of Rock Fracturing and Permeability Change in Excavation-Damaged Zones. Int. J. Geomech. 11, 302–313. https://doi.org/10.1061/(ASCE)GM.1943-5622.0000034

Shen, B., 2014. Development and applications of rock fracture mechanics modelling with FRACOD: a general review. Geosystem Eng. 17, 235–252. https://doi.org/10.1080/12269328.2014.969388

Snow, D.T., 1969. Anisotropie Permeability of Fractured Media. Water Resour. Res. 5, 1273–1289. https://doi.org/10.1029/WR005i006p01273

Tatone, B.S.A., Grasselli, G., 2015. A calibration procedure for two-dimensional laboratory-scale hybrid finite–discrete element simulations. Int. J. Rock Mech. Min. Sci. 75, 56–72. https://doi.org/10.1016/J.IJRMMS.2015.01.011

Tsang, Y.W., Witherspoon, P.A., 1981. Hydromechanical behavior of a formable rock fracture subject to

normal stress. J. Geophys. Res. 86, 9287–9298. https://doi.org/10.1029/JB086iB10p09287

Valera, M., Guo, Z., Kelly, P., Matz, S., Cantu, V.A., Percus, A.G., Hyman, J.D., Srinivasan, G., Viswanathan, H.S., 2017. Machine learning for graph-based representations of three-dimensional discrete fracture networks. Comput. Geosci. 22, 695–710. https://doi.org/10.1007/s10596-018-9720-1

Vogel, T., Gerke, H.H., Zhang, R., Van Genuchten, M.T., 2000. Modeling flow and transport in a two-dimensional dual-permeability system with spatially variable hydraulic properties. J. Hydrol. 238, 78–89. https://doi.org/10.1016/S0022-1694(00)00327-9

Wang, X.H., Li, L., Wang, M., Liu, Z.F., Shi, A.F., 2020. A discrete fracture model for two-phase flow involving the capillary pressure discontinuities in fractured porous media. Adv. Water Resour. 142, 103607. https://doi.org/10.1016/j.advwatres.2020.103607

Warren, J.E., Root, P.J., 1963. The Behavior of Naturally Fractured Reservoirs. Soc. Pet. Eng. J. 3, 245–255. https://doi.org/10.2118/426-PA

Zhao, Z., Li, B., Jiang, Y., 2013. Effects of Fracture Surface Roughness on Macroscopic Fluid Flow and Solute Transport in Fracture Networks. Rock Mech. Rock Eng. 47, 2279–2286. https://doi.org/10.1007/s00603-013-0497-1

Zimmerman, R.W., Bodvarsson, G.S., 1996. Effective transmissivity of two-dimensional fracture networks. Int. J. Rock Mech. Min. Sci. Geomech. 33, 433–438. https://doi.org/10.1016/0148-9062(95)00067-4

Chapter 5

Estimating and characterizing equivalent resistivity using fractures characterized by FEMDEM method

5.1 Introduction

It is still challenging to characterize and detect rock fractures (e.g., faults, joints) in engineering practice (Wolfsberg, 1997). Various geophysical methods (e.g., electrical or electromagnetic methods) have been widely used to detect water-filled fractures since they show more conductive than intact rock (Elis et al., 2019; SEKINE et al., 1997; Wolfsberg, 1997). The rock equivalent or effective electrical conductivity can be determined by laboratory experiments (e.g., Brace and Orange, 1966, 1968; Wang et al., 1978). Several effective medium methods such as self-consistent approximation have also been developed to estimate equivalent electrical conductivity of fractured rock (e.g., Saevik et al., 2014). The numerical methods can also be adopted to estimate electrical conductivity by utilizing an analogy between Darcy's law and Ohm's law (e.g., Bahr, 1997; Brown, 1989; Kirkby et al., 2016; Kirkby and Heinson, 2017; Sanz et al., 2017). For example, a discrete-dual-porosity model is was proposed for modeling electric current flow in a 2D fractured rock (Caballero Sanz et al., 2017; Roubinet and Irving, 2014). The TOUGH2 was used to model electric current flow in fractured rock (Magnusdottir et al., 2012).

The geometrical properties of fractures used in those methods are described by certain statistical distributions of natural fractures in rocks. The discrete fracture network (DFN) modelling approach provides possible statistical descriptions of natural fractures (e.g., Dverstorp and Andersson, 1989; Lei et al., 2017). The variations in electrical resistivity of fractures caused by the initiation and propagation of fractures in intact rock are not well described by the DFN modeling approach. Instead, the hybrid finite-discrete element method (FEMDEM) fracture model has been developed to simulate fracture initialization and propagation due to local stress perturbations (e.g., tunnel excavations) in intact rock (Lisjak and Grasselli, 2014; Munjiza, 2004; Munjiza et al., 1995). To our best knowledge, there is no research that has been made to estimate equivalent electrical resistivity of fractures characterized by the FEMDEM fracture model.

In this chapter, we propose a novel numerical way to model electrical current flow in fractured rock using the unified pipe network model. The unified pipe network model proposed by Ren et al. (2017) was developed to model a steady-state fluid flow in fracture rock by discretizing rock matrix and fractures into matrix pipes and fracture pipes, respectively. The model is admirably adapted to model electric current flow in fractured rock by making an analogy between the Darcy's law and the Ohm's law. Then, the equivalent electrical resistivity of fractured rock can be estimated based on the electrical potential distribution modelled by the method. The

chapter is organized as follows: the DFN modeling approach which describes fracture geometrical properties statistically, the hybrid FEMDEM fracture model which models the initialization and propagation of fractures, the unified pipe network model which simulates electrical current flow in fractured rock under the steady state conditions are introduced. Then, several case studies are made to estimate the equivalent electrical resistivity of fractured rock. Case 1 shows the electrical resistivity of a rock where only a single fracture is embedded. Case 2 shows the equivalent resistivities of DFN models with different fracture densities. Case 3 shows variations in equivalent resistivities of a rock sample through a uniaxial compressive strength (UCS) laboratory test. The last case shows the variations in equivalent electrical resistivities at different locations near the tunnel excavation surface which capture the initiation and propagation due to a local excavation in the rock mass.

5.2 Theories and methods

DFN

The DFN modelling approach which generates fractures stochastically has been widely used to characterize geometrical properties (e.g., orientations lengths) of natural fractures (Lei et al., 2017). Fractures can be represented by planar disks in a 3D DFN model or line segments in a 2D DFN model (Baecher, 1983). Their locations are assumed to follow a Gaussian, Fisher, or a uniform distribution (Einstein and Baecher, 1983).The fracture mass density can be defined as P_{32}, P_{21} or P_{10} (Dershowitz and Herda, 1992). A negative power law distribution with a scaling exponent has been proved reasonably through field studies to describe fracture lengths (Baecher, 1983; Barton, 1981; Bonnet et al., 2001; Bour, 2002; Davy et al., 2010; Lei et al., 2015). Fig. 5.1 shows a representative case of a DFN model.

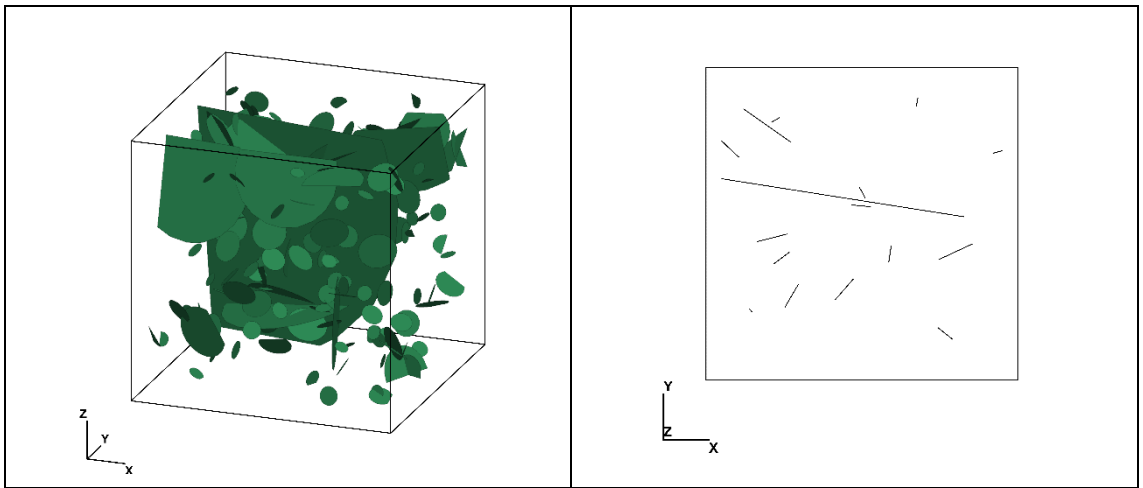

(a) (b)

Fig. 5.1. A representative case of the DFN model: (a) a 3D DFN model; (b) 2D fracture network

cut through z = 10.0.

Hybrid finite-discrete element method

The initialization and propagation in fractured rock mass can be well modeled by the combined finite-discrete element method (FEMDEM) (Lisjak and Grasselli, 2014; Munjiza, 2004; Munjiza et al., 1995). The FEMDEM fracture model has been applied in simulating fracture patterns developed under biaxial loading conditions and modeling of EDZ formation process caused a tunnel excavation in a bedded rock, etc. (Lisjak and Grasselli, 2014). In the model, the rock matrix should be discretized into a two-dimensional (2D) unstructured mesh of triangular elements and fracture embedded in the rock are meshed into 1D segments. As Fig. 4.1a shows, every side of a typical triangular element is surrounded by two four-node joint elements. The linear elastic finite element analysis of linear triangular elements is used to model the deformation of the rock matrix. Two model parameters: Young's modulus and Poisson's ratio are enough to characterize its deformations for an isotropic linear elastic analysis. The four-node joint elements are sued to capture fracture initialization and propagation that developed in fractured rock. The joint elements are created between triangular elements pairs. The joint element is assumed to be broken if a fracture initializes and propagates.

Regarding characterizing possible failure types of joint elements, three types of modes: Mode I, Mode II, and a mixed mode of both exist. The possible fracture types of joint elements are shown in Figs. 4.2a, 4.2b, and 4.2c, respectively. Mode I as shown in Fig. 4.2a is a tensile mode which describes tensile failure of a joint element. In the Mode I, a joint element starts to undergo tensile damage as its joint opening amount increase over a critical value δ_0. As its joint opening amount increases over the maximum opening amount δ_f, it finally breaks and a tensile fracture is formed between two matrix triangular elements. Similarly, Mode II as shown in Fig. 4.2b shows a formation process of shear fracture. The shear fracture is generated as its joint slip amount is equal to the maximum slip amount s_f. If its tangential slip amount is not larger than a critical value s_0, there is no shear fracture. As its slip amount is larger than s_0, shear damage starts to occur in the joint element. The mixed mode shown in Fig. 4.2c is a failure combination of Mode I and Mode II. The joint element is considered as a fracture when the joint opening is equal to δ_f and the joint slip is equal to s_f. The fracture element undergoes both shear and tensile damage.

Unified pipe network model

To calculate the equivalent electrical resistivity of fractured rock numerically, electric current flow through fractures and rock matrix should be modeled first. The unified pipe network model is initially developed to simulate a steady state fluid flow in fractured rock (Ren et al.,

2017). By making an analogy between the Darcy's law which describes fluid flow and the Ohm's law which models electric current flow, the unified pipe network model can be easily adapted for modeling a steady state electric current flow in fractured rock. To introduce clearly where the unified pipe network model is adapted for simulating electric current flow it is introduced with comparing with the original unified pipe network model which models fluid flow through fractured rock.

The classic Darcy's law is written as:

$$Q = \frac{k}{u}\nabla p \tag{5.1}$$

where Q is the flow rate, k is the permeability, u is the fluid viscosity, p is the fluid pressure. Similarly, the Ohm's law is defined as:

$$J = \sigma\nabla\varphi \tag{5.2}$$

where J is the electric current, σ is the rock electrical conductivity, and φ is the electric potential. The similarities between the Darcy's law and Ohm's law are described in Table 5.1.

Table 5.1. The Darcy's law which describes a steady state fluid flow and the Ohm's law which models a steady state electric current flow.

	Darcy's law	Ohm's law
Rock property	Hydraulic conductivity $\frac{k}{u}$ (unit: $\mathrm{m}^2/\mathrm{Pa}\cdot\mathrm{s}$)	Electrical conductivity σ (unit: $1/\Omega\cdot\mathrm{m}$)
Potential	Pressure p (unit: Pa)	Electric potential φ (unit: V)
Flux	Q (unit: m/s)	J (unit: A/m^3)

Following the adapted unified pipe-network model, the electric potential in the unstructured mesh of triangular matrix elements and four-node fracture elements under electric potential conditions can be calculated. In the unified pipe network model, the fractured rock mass is divided into a pipe network system as shown in Fig. 4.4. Fig. 4.4a illustrates the rock matrix into which natural fractures are embedded. Fig. 4.4b shows the pipe network system representing the fractured rock mass. There are two types of pipes which are shown in Fig. 4.4b: matrix pipes representing rock matrix, and fracture pipes representing fractures. The unified pipe network model has an advantage over the traditional pipe network model (e.g., Heydari et al., 2018; Li et al., 2014) in that the former can consider dead-end fractures which are also important in fluid flow and electric current flow in fractured rock. The equivalent electrical (or hydraulic) parameters of both matrix pipes and fracture pipes are derived from the locally homogenized macroscopic media.

The Ohm's law is valid for modeling electric current flow in both matrix pipes and fracture pipes. Instead of obeying the law of conservation of mass for a steady state fluid flow, a nodal electric current flow at each pipe node obeys the law of conservation of charge for a steady-state electric current flow. It can be expressed as:

$$\sum_{i=1}^{n} J_i = J_{si} \tag{5.3}$$

where n is the total number of pipes which are connected to the node, J_i is the electric flux, and J_{si} is the source term. A general governing equation of the Ohm's law in a matrix form by substituting Eq. 5.3 into Eq. 5.2 is written as follows:

$$[K]_{n\times n}\{J\}_{n\times 1} = \{J_s\}_{n\times 1} \tag{5.4}$$

Prescribing electric potential boundary conditions, the governing equation can be solved numerically. A natural rough fracture is homogenized into an idealized fracture pipe through the parallel plate model. The flow rate through an idealized fracture pipe obeys the cubic law, which is defined as (Li et al., 2014; Priest, 1993; Ren et al., 2017; Schrauf and Evans, 1986; Tsang and Witherspoon, 1981):

$$Q = \frac{a^3}{12u}\frac{\partial p}{\partial l} \tag{5.5}$$

where a is the hydraulic aperture, l is the fracture pipe length. Here, fracture permeability k_f is equal to $\frac{a^2}{12}$. The electric flux through fracture pipes does not follow Eq. 5.5. Instead, it is defined as:

$$J = a\sigma_f \frac{\partial \varphi}{\partial l} \tag{5.6}$$

where a is electric aperture, σ_f is fracture electrical conductivity. A rock matrix triangle element consists of three matrix pipe elements as shown in Fig. 4.5. o is the circumcenter of the triangle ijk. l_{of} is the length of the perpendicular from o to the line ij. The equivalent conductance coefficient K_{ij} of the matrix pipe which connecting node i and node j is defined as:

$$K_{ij} = \frac{l_{of}\sigma_f}{l_{ij}} \tag{5.7}$$

where l_{ij} is the length of the line ij, σ_f is rock matrix electrical conductivity. Similarly, the equivalent conductance coefficients for pipes connecting nodes im and nodes jm are defined as:

$$K_{im} = \frac{l_{oe}\sigma_f}{l_{im}} \tag{5.8}$$

$$K_{jm} = \frac{l_{og}\sigma_f}{l_{jm}} \tag{5.9}$$

The electric flux J_{ij} through the matrix pipe *ij* is defined as:

$$J_{ij} = K_{ij}(\varphi_i - \varphi_j) \tag{5.10}$$

Equivalent electrical resistivity

Electrical resistivity is the reciprocal quantity of electrical conductivity. The electrical resistivity tensor of fractured rock is written in a 2D tensor as follows:

$$\boldsymbol{\rho} = \begin{bmatrix} \rho_{xx} & \rho_{xy} \\ \rho_{yx} & \rho_{yy} \end{bmatrix} \tag{5.11}$$

The electrical resistivity tensor is symmetric. Thus, $\rho_{xy} = \rho_{yx}$. A volume-averaged electric flux <J> is defined as:

$$< \mathrm{J} >= \frac{1}{V}\sum_{e}\int_{V_e} J_e \, dV_e \tag{5.12}$$

In that equation, V is the total volume of rock mass; V_e is the element volume. For a fracture element, V_e is scaled by fracture aperture a; J_e represents an element-wise electric flux. Similarly, the volume-averaged electric potential gradient is given as:

$$< \frac{\partial \varphi}{\partial x_i} \geq \frac{1}{V}\sum_{e}\int_{V_e} \frac{\partial \varphi_e}{\partial x_i} dV_e \tag{5.13}$$

where $\frac{\partial \varphi_e}{\partial x_i}$ is the electric potential gradient in the i direction. Finally, the equivalent electrical resistivity is calculated as follows:

$$\begin{bmatrix} < \frac{\partial \varphi}{\partial x} >^{I} & < \frac{\partial \varphi}{\partial y} >^{I} & 0 & 0 \\ 0 & 0 & < \frac{\partial \varphi}{\partial x} >^{I} & < \frac{\partial \varphi}{\partial y} >^{I} \\ < \frac{\partial \varphi}{\partial x} >^{II} & < \frac{\partial \varphi}{\partial x} >^{II} & 0 & 0 \\ 0 & 0 & < \frac{\partial \varphi}{\partial x} >^{II} & < \frac{\partial \varphi}{\partial x} >^{II} \end{bmatrix} \begin{bmatrix} {\rho_{xx}}^{-1} \\ {\rho_{xy}}^{-1} \\ {\rho_{yx}}^{-1} \\ {\rho_{yy}}^{-1} \end{bmatrix} = \begin{bmatrix} < J_x >^{I} \\ < J_y >^{I} \\ < J_x >^{II} \\ < J_y >^{II} \end{bmatrix} \tag{5.14}$$

where $<>^{\mathrm{I}}$, $<>^{\mathrm{II}}$ are numerical experiments under Boundary I, and II (Fig. 5.2), respectively.

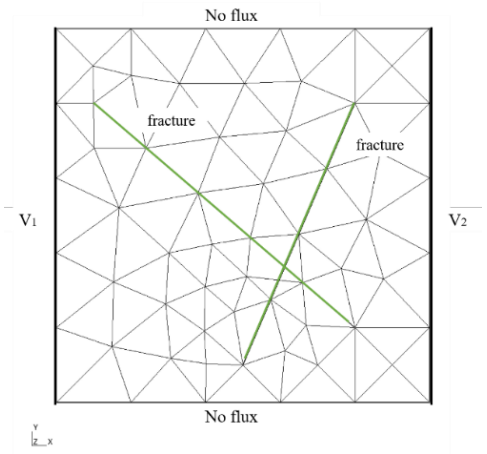

(a) (b)

Fig. 5.2. Schematic diagram of two basic numerical experiments for deriving equivalent resistivity tensor: (a) The left boundary and right boundary are prescribed as the Dirichlet boundaries with constant electric potential with V_1 = 1.0 V and V_2 = 0.0 V; the other boundaries are nonconductive. (b) The top boundary and bottom boundary as the Dirichlet boundaries with constant electric potential with V_1 = 1.0 V and V_2 = 0.0 V; the other boundaries are nonconductive.

5.3 Case studies

Case 1

In Case 1 as shown Fig. 4.7, we apply our proposed method to estimate an equivalent electrical resistivity tensor of a rock where only a single fracture is embedded in rock matrix. The fracture with a length of 5 m is located in the center of the rock matrix whose side length is 10 m. The rock matrix and the fracture are meshed using Gmsh (Geuzaine and Remacle, 2009). The rock matrix is discretized into matrix pipes. In contrast, the fracture is discretized into 20 1D fracture pipes. To study the relationship between the equivalent electrical resistivity and the fracture orientation, several fracture orientation configurations as shown in Fig. 4.8 are made. The fracture orientation is 0°, 15°, 30°, 45°, 60°, 75°, 90° for fracture 1, 2, 3, 4, 5, 6, and 7. For each fracture configuration, fracture electrical resistivity and matrix resistivity is $1.0 \times 10^{-5}\ \Omega \cdot$ m, 1.0 $\Omega \cdot$ m, respectively.

The simulated electric potential distributions are shown in Fig. 5.3. Based on those electric potential distributions, Fig. 5.4 shows the estimated electrical resistivities of the rock calculated from Eq. 5.14. From Fig. 5.4a, it is clear that ρ_{xx} increases as fracture angle increases between 0° and 90°. In contrast, ρ_{yy} decreases as fracture angle increases. As fracture orientation is 0°, the fracture has no effect on the ρ_{yy} though it has the largest effect on the ρ_{xx}. Similarly, as fracture orientation is 90°, the fracture does not contribute to ρ_{xx}, but has the most effect on

decreasing the ρ_{yy}. As Fig. 5.4b, as fracture orientation is 0° or 90°, both ρ_{xy} and ρ_{yx} are large. As fracture orientation changes between 0° and 90°, both ρ_{xy} and ρ_{yx} decrease as fracture orientation increases between 0° and 45°, then increase as fracture orientation increases between 45° and 90°.

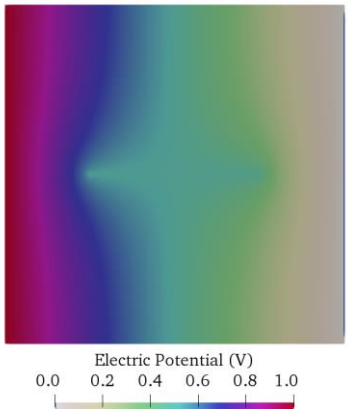

(a)

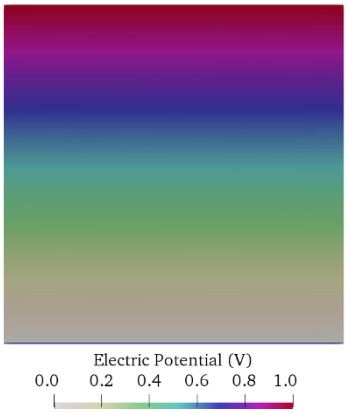

(b)

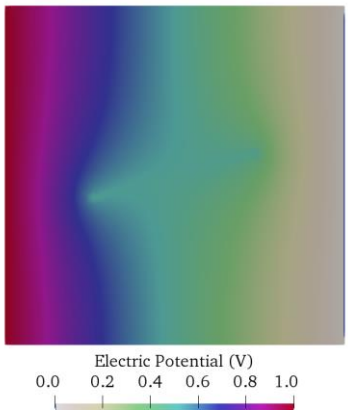

(c)

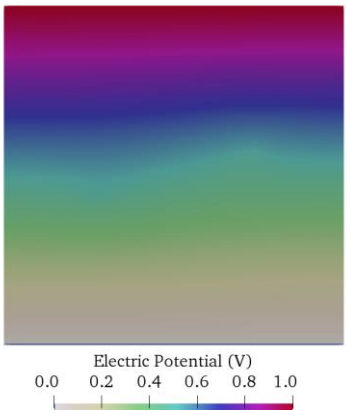

(d)

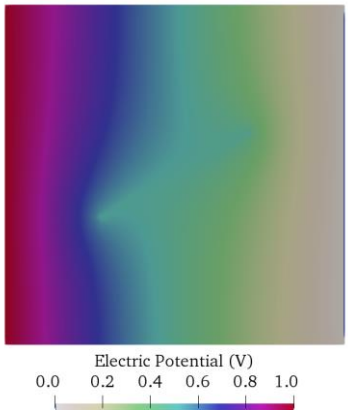

(e)

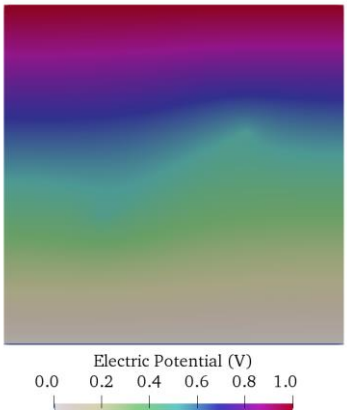

(f)

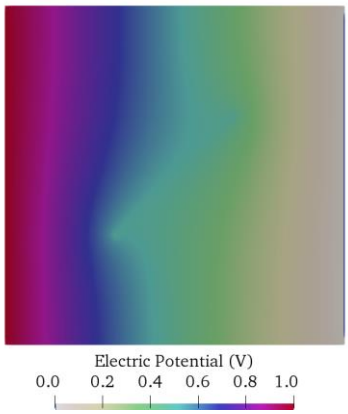 Electric Potential (V) 0.0 0.2 0.4 0.6 0.8 1.0	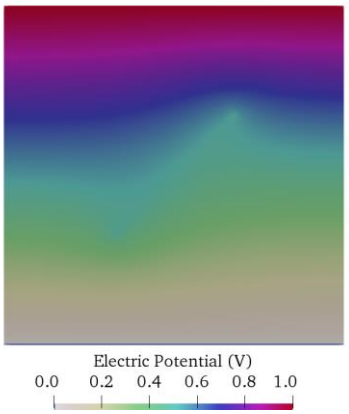 Electric Potential (V) 0.0 0.2 0.4 0.6 0.8 1.0
(g)	(h)
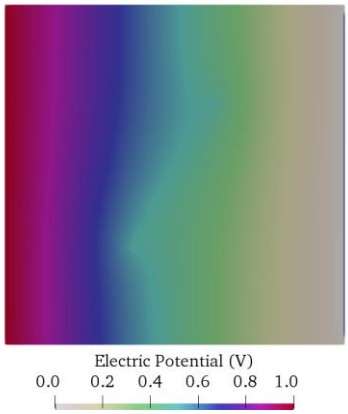 Electric Potential (V) 0.0 0.2 0.4 0.6 0.8 1.0	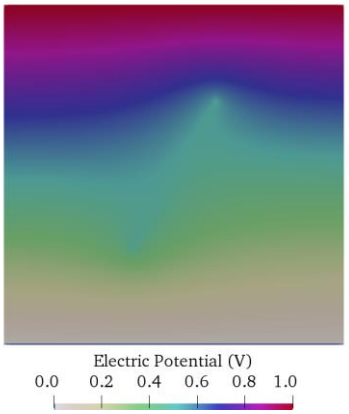 Electric Potential (V) 0.0 0.2 0.4 0.6 0.8 1.0
(i)	(j)
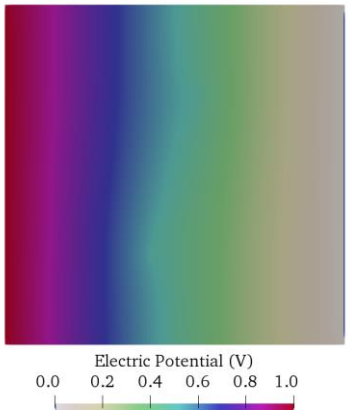 Electric Potential (V) 0.0 0.2 0.4 0.6 0.8 1.0	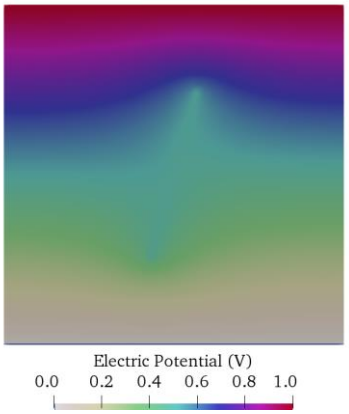 Electric Potential (V) 0.0 0.2 0.4 0.6 0.8 1.0
(k)	(l)

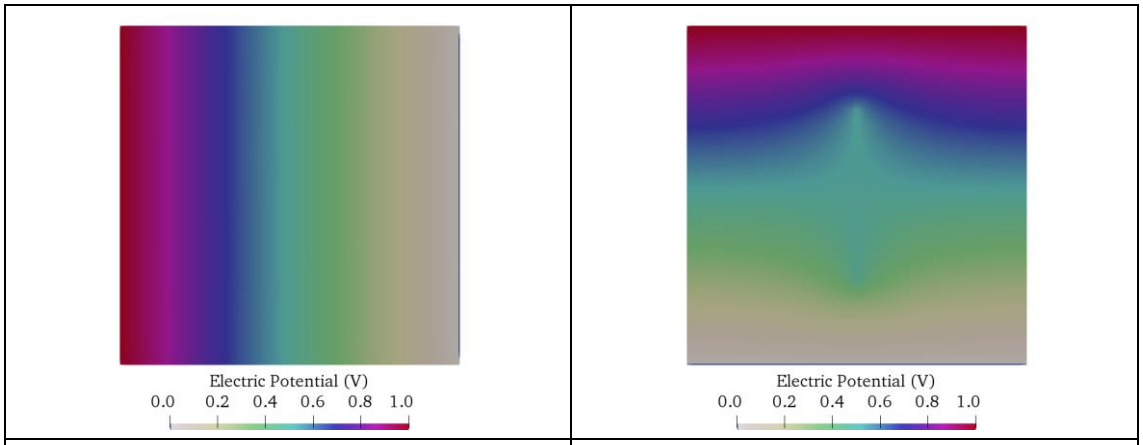

Fig. 5.3. Electric potential distribution of each fracture configuration under Boundary I and II (Fig. 5.2).

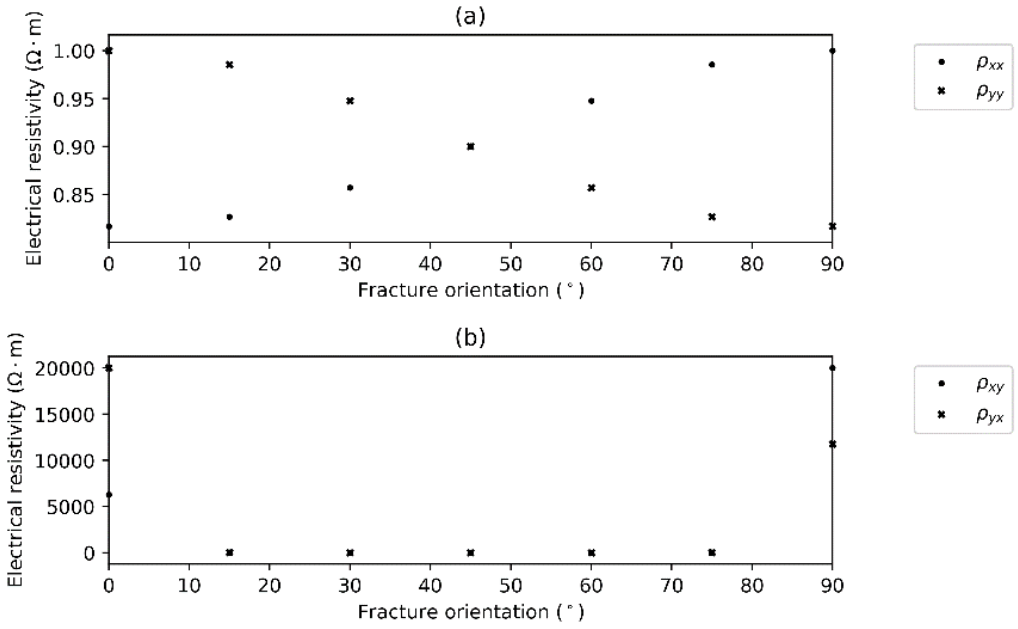

Fig. 5.4. Equivalent electrical resistivities using electric potential distributions shown in Fig. 5.3.

Case 2

In Case 2, we calculate the equivalent electrical resistivities of the DFN models with varying fracture densities using our proposed method. The DFN models which are generated in the domain with a size of 20 m × 20 m × 20 m using the DFN modeling approach are shown in Fig. 4.11. The mass density P_{32} for each DFN model is 0.2, 0.4, 0.6, 0.8, 1.0 m^2/m^3, respectively. In each DFN model, fracture orientations are assumed to be uniformly distributed. The fracture lengths for each

DFN model are distributed following a power-law distribution with a scaling exponent of 3.0. The maximum, minimum fracture size is 200.0 m, and 1.0 m, respectively. To apply our method, a 2D model in which fractures are considered line segments in a 2D rock matrix is necessary. Thus, the cross-sections (Fig. 4.11b, 4.11d, 4.11f, 4.11h, 4.11j) that cut through 3D DFN models (Fig. 4.11a, 4.11c, 4.11e, 4.11g, 4.11i) by plane z = 10 m are used to model the static steady current flow under Boundary I and Boundary II. The matrix electrical resistivity is assigned to 1.0 $\Omega \cdot$ m. The fracture electrical resistivity is $1.0 \times 10^{-5}\ \Omega \cdot$ m. For each fracture, its aperture is 1.0×10^{-3} m.

The electric potential distributions under Boundary I and II are shown in Fig. 5.5. Based on those electric potential distributions, their equivalent electrical resistivities are shown in Fig. 5.6. As Fig. 5.6a shows, as P_{32} increases, both ρ_{xx} and ρ_{yy} decease. However, ρ_{xy} or ρ_{yx} increases at first and then decrease a bit. The ρ_{xx} and ρ_{yy} of the DFN model whose P_{32} is 0.2 m^2/m^3 is 0.62, 0.96 $\Omega \cdot$ m, respectively. ρ_{yy} is almost equal to the rock matrix electrical resistivity. It indicates, the DFN model is almost isotropic in the y axis. As P_{32} reaches 1.0 m^2/m^3, ρ_{xx} and ρ_{yy} are 0.34 and 0.33 $\Omega \cdot$ m, respectively. The DFN model are nearly isotropic since ρ_{xx} and ρ_{yy} are almost the same. As Fig. 4.11j shows, fractures are homogeneous distributed in the rock mass. The ρ_{xy}, ρ_{yx} for the DFN model with P_{32} of 0.2 m^2/m^3 is -11.0 $\Omega \cdot$ m, -10.5 $\Omega \cdot$ m, respectively. The ρ_{xy} is negative, which means that the components of fractures in the x axis act as barriers that prevent electric current flow across fractures in the y axis. The components of fractures in the y axis also act as electric barriers. The ρ_{xy} and ρ_{yx} become 5.2, and 3.6 $\Omega \cdot$ m, respectively. The ρ_{xy} becomes positive. It demonstrates that the components of fractures in the x axis act as electric conductors that contribute to electric current flow across fractures in the y axis. The components of fractures in the y axis also act as electric conductors.

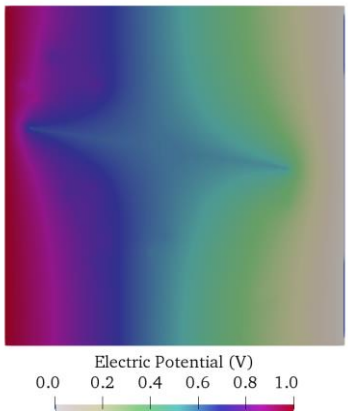

(a)

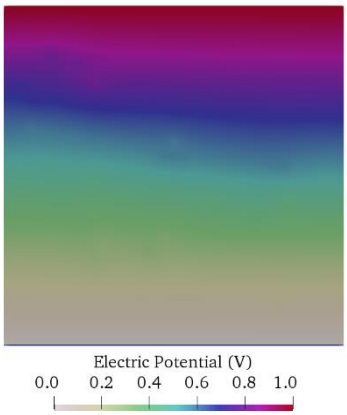

(b)

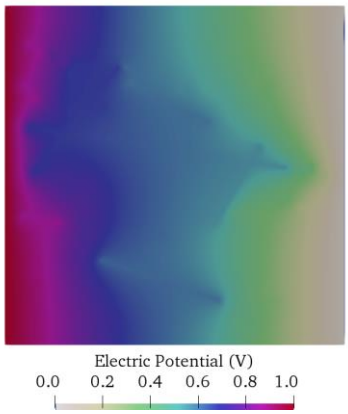 Electric Potential (V) 0.0 0.2 0.4 0.6 0.8 1.0	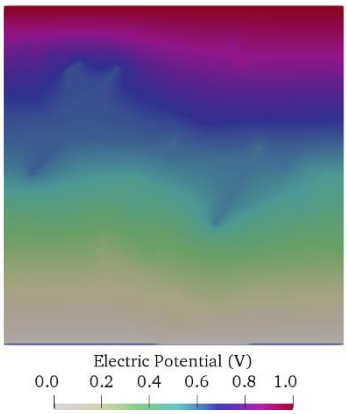 Electric Potential (V) 0.0 0.2 0.4 0.6 0.8 1.0
(c)	(d)
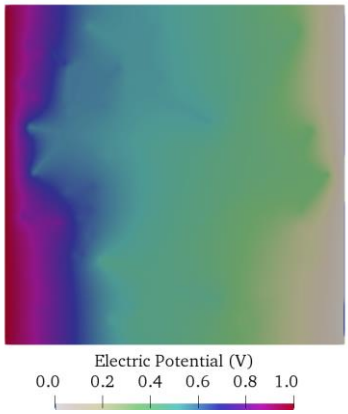 Electric Potential (V) 0.0 0.2 0.4 0.6 0.8 1.0	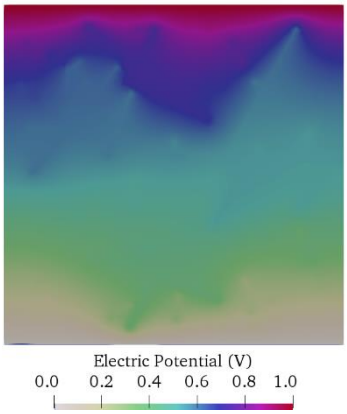 Electric Potential (V) 0.0 0.2 0.4 0.6 0.8 1.0
(e)	(f)
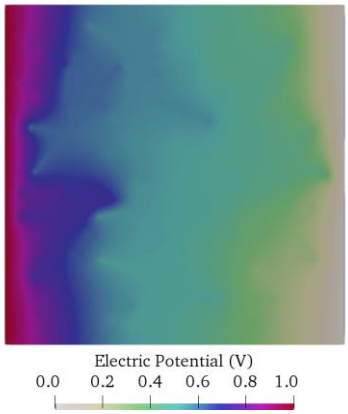 Electric Potential (V) 0.0 0.2 0.4 0.6 0.8 1.0	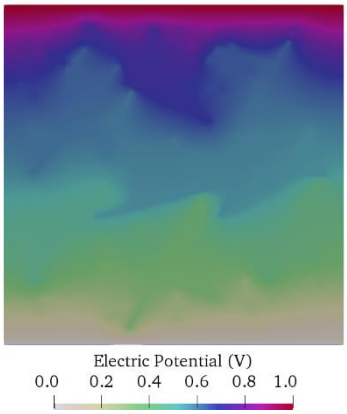 Electric Potential (V) 0.0 0.2 0.4 0.6 0.8 1.0
(g)	(h)

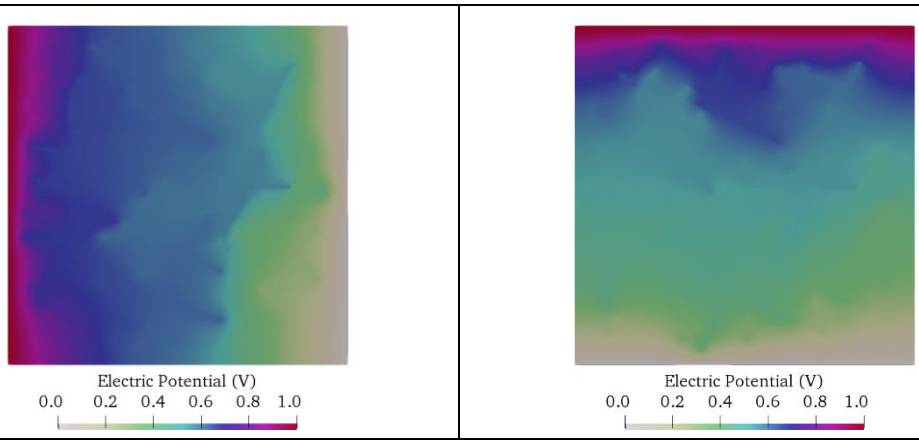

(i) (j)

Fig. 5.5. Electric potential distributions in the DFN models (Fig. 4.11) under Boundary I and Boundary II using the electric pipe network model.

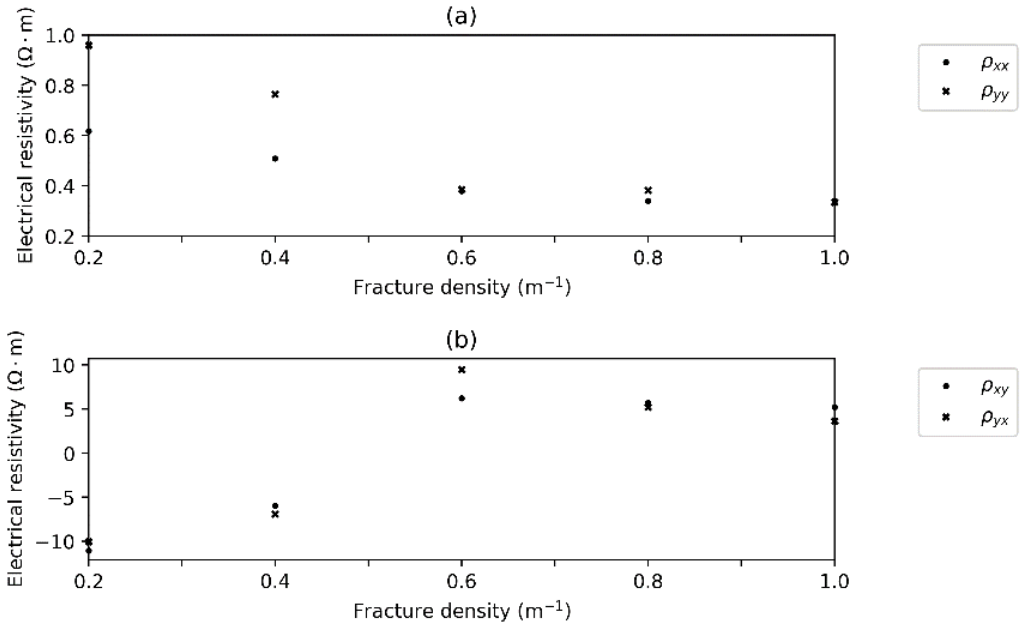

Fig. 5.6. Equivalent electrical resistivities of DFN models (Fig. 4.11) using corresponding electric potentials (Fig. 5.5).

Case 3

The initialization and propagation of new fractures in intact rock are modeled using the FEMDEM fracture model under a representative uniaxial compressive strength (UCS) laboratory test in Case 3. The Y-Geo in which FEMDEM is embedded (Lisjak and Grasselli, 2014; Munjiza, 2004; Munjiza et al., 1995) is used. The steady electric current flow in such fractured rock under

Boundary I and Boundary II is modeled by the electric pipe network model. At last, the equivalent electrical resistivities of fractured rock using Eq. 5.14 are calculated. The input model parameters used in the FEMDEM model are shown in Table 4.1. The specimen is discretized into 2D unstructured triangular matrix elements using Gmsh (Geuzaine and Remacle, 2009). The cohesive elements with zero thickness are inserted between neighboring matrix elements. The smallest element size is 7.5×10^{-4} m. The time step size is 3.0×10^{-9} s to ensure numerical stability of the explicit time integration of the FEMDEM fracture model. In the uniaxial loading condition, the top boundary and the bottom boundary move in opposite directions with a constant velocity of 0.25 m/s. Although the loading rate is much greater than that of an actual experiment, fractures in intact rock can develop fast in a short time. The total number of time steps is 150000. The fracture initializes when the step number is 100,000. Fig. 4.16 shows fractures and their fracture apertures that developed in intact rock when the time step is 105,000, 110,000, 115,000, 120,000, 125,000, and 130,000, respectively. The matrix electrical resistivity is 10000 $\Omega \cdot$ m. The fracture openings which modeled by the FEMDEM fracture model are regarded as electrical apertures. The apertures are shown in Fig. 4.16. To study the effect of the fracture electrical resistivity on the equivalent resistivity, it is assigned 1, 10, 100, and 1,000 $\Omega \cdot$ m, in Methods 1, 2, 3, 4, respectively.

The electric potential distribution in intact rock under Boundaries I and II are shown in Fig. 5.7. Based on those electric potential distributions, the calculated electrical resistivities are shown in Fig. 5.8. As Fig. 5.8 shows, ρ_{xx} and ρ_{yy} decease as time steps increase for all methods. Their values decrease at the fastest rate in the Method 1 in which rock matrix resistivity/fracture resistivity are the largest. Since matrix resistivity/fracture resistivity are relatively small for Methods 2, 3 and 4, ρ_{xx} and ρ_{yy} decease slowly.

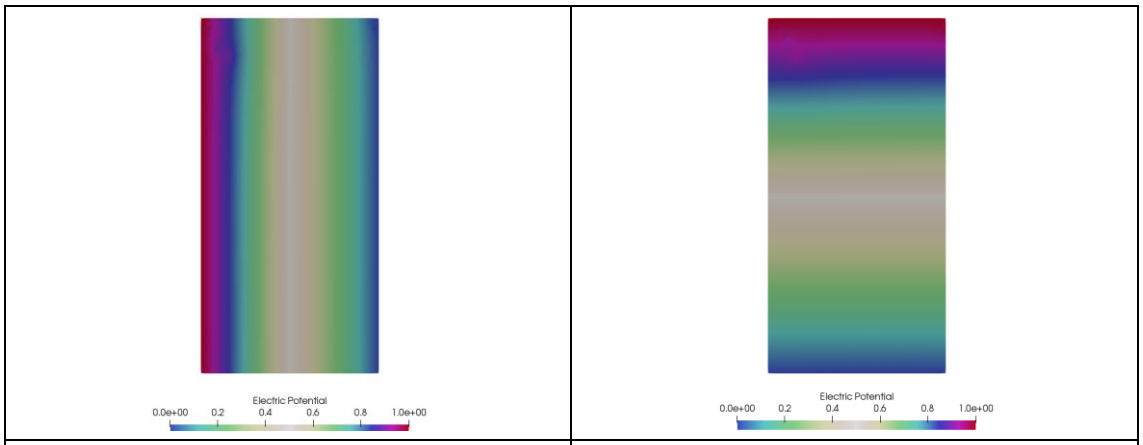

(a) (b)

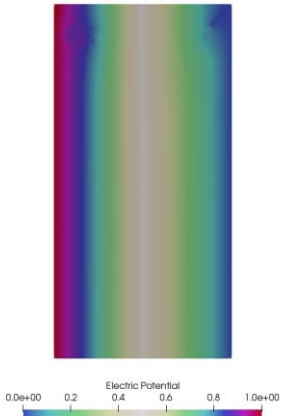 Electric Potential 0.0e+00 0.2 0.4 0.6 0.8 1.0e+00	 Electric Potential 0.0e+00 0.2 0.4 0.6 0.8 1.0e+00
(c)	(d)
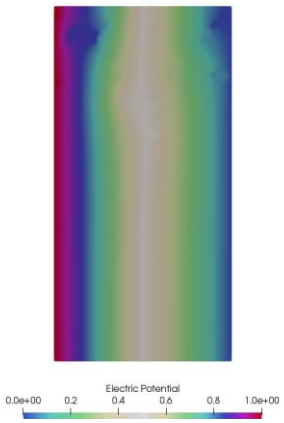 Electric Potential 0.0e+00 0.2 0.4 0.6 0.8 1.0e+00	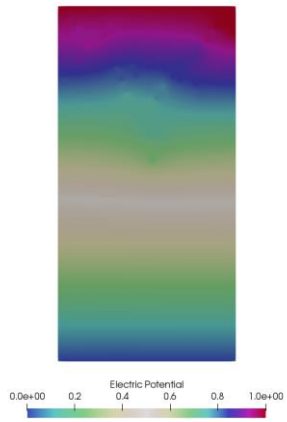 Electric Potential 0.0e+00 0.2 0.4 0.6 0.8 1.0e+00
(e)	(f)
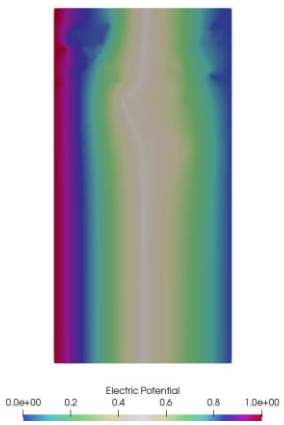 Electric Potential 0.0e+00 0.2 0.4 0.6 0.8 1.0e+00	 Electric Potential 0.0e+00 0.2 0.4 0.6 0.8 1.0e+00
(g)	(h)

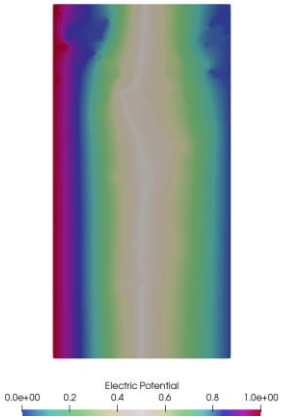

(i)

(j)

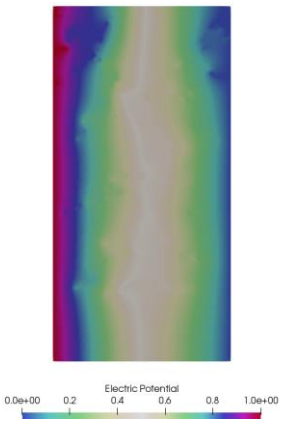

(k)

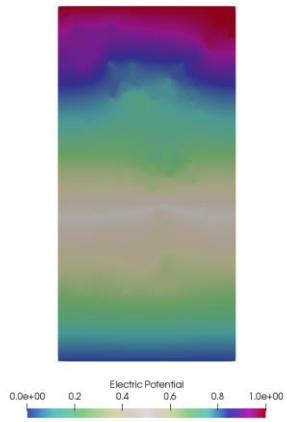

(l)

Fig. 5.7. Electric potential distributions of fracture that are initialized and propagated in the intact rock under the compressive uniaxial test.

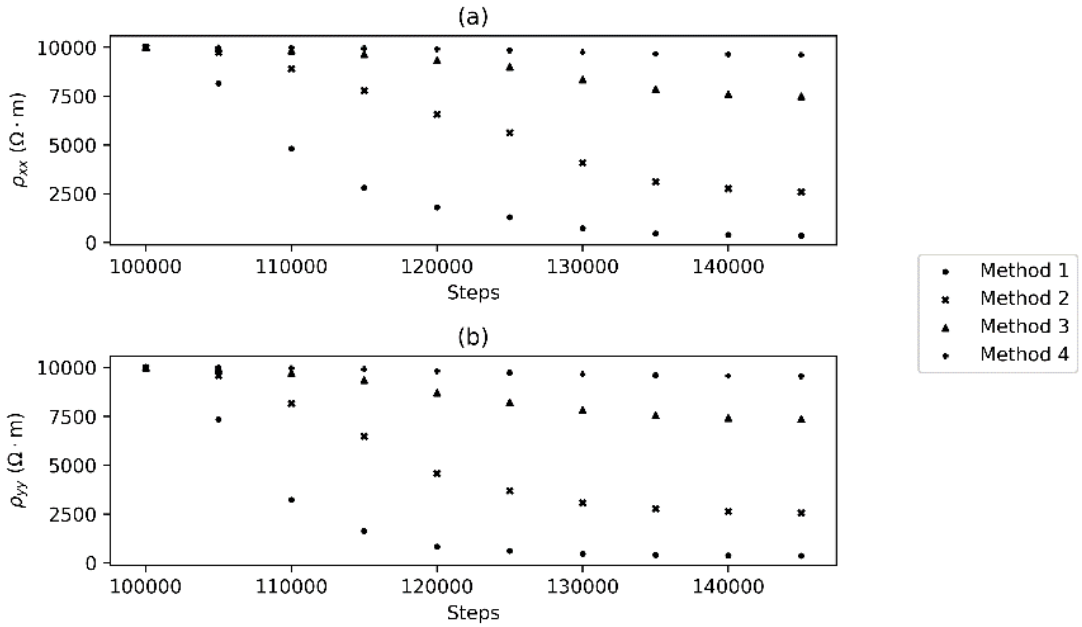

Fig. 5.8. Progressive evolution of ρ_{xx} and ρ_{yy} with fracture initiation and propagation in intact rock (Fig. 4.16). A different fracture electrical conductivity is assigned in each method.

Case 4

The EDZ permeability has been calculated through the in-situ experiments and numerical investigations (Aoyagi and Ishii, 2019). However, to our best knowledge, there is still no research that estimates the EDZ electrical resistivity. In the Case 4, the EDZ electrical resistivity tensor is estimated.

Fig. 4.20 shows a schematic layout of the model. The rock mass with a side length of 25 m is a mudstone sedimentary rock. The initial horizontal, vertical compressive stress is 4.81 MPa and 5.04 MPa, respectively. A horseshoe shaped tunnel is excavated in the rock mass. The model boundary conditions are fixed displacement boundary conditions. The rock mass is meshed into unstructured triangular mesh using Gmsh. The Y-Geo in which FEMDEM is embedded (Lisjak and Grasselli, 2014; Munjiza, 2004; Munjiza et al., 1995) is used. Approximate 160,000 matrix elements are generated. The minimum element size is 0.01 m. To capture fracture initialization and propagation in the rock mass, cohesive elements are inserted between matrix elements. The extent of fractures that develops in the EDZ are not homogenous. Thus, permeabilities at different positions around tunnel excavation are different. To represent the EDZ electrical resistivity, three different locations namely, Top Block, Right Block, Bottom Block are chosen. The positions and sizes of the chosen blocks are shown in Fig. 4.21. The effect of the block size on the electrical resistivity tensor is neglected in this chapter though the electrical resistivity tensor varies with the block size. The model parameters for the FEMDEM fracture model are summarized in Table 4.2. The total number of time steps is 500,000. The time step size is 1.0×10^{-8} s. The tunnel is

excavated at time step 30,000 and totally removed at time step 50,000.

The electrical resistivity of intact rock is assumed to be 10,000 $\Omega \cdot \mathrm{m}$. The fracture resistivity for each fracture is set to 1, 10, 100, and 1,000 $\Omega \cdot \mathrm{m}$, respectively to study its effect on fractured rock equivalent resistivity. Since the fracture resistivity is much smaller than the matrix resistivity, the fractures in the rock decrease the electrical resistivity of the rock mass. The fracture openings defined in the Mode I of the FEMDEM fracture model are used to represent fracture apertures.

The fractures that developed in the EDZ at time step 200,000, 300,000, 400,000, and 500,000, respectively, are shown Fig. 4.22. The size of the EDZ increases gradually. The progressive of fracture apertures is shown in Fig. 4.23. Fracture openings modeled by the FEMDEM fracture model are regarded as fracture apertures. Figs. 5.9 – 5.12 show estimated electrical resistivities at different locations around tunnel excavation surface. As Figs. 5.9 – 5.12 show, both ρ_{xx} and ρ_{yy} decrease gradually as time steps increase.

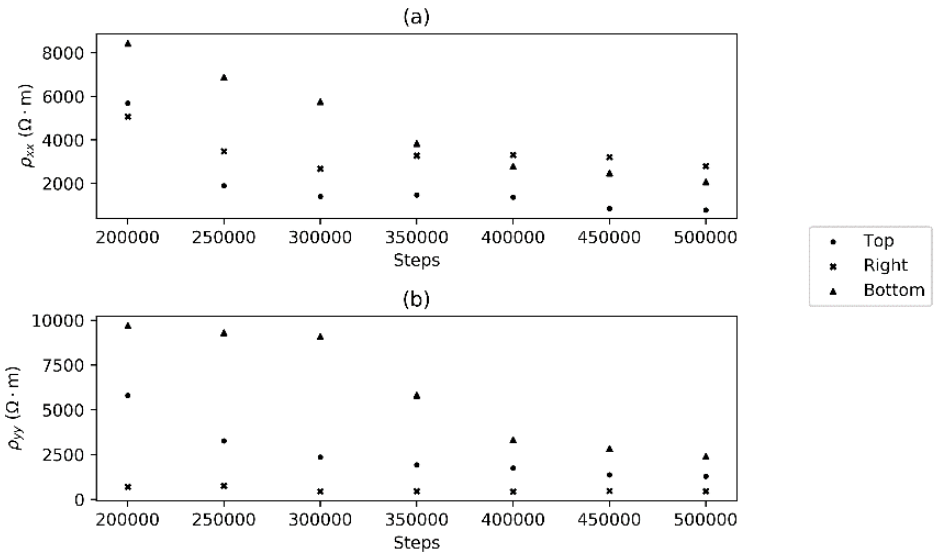

Fig. 5.9. Progressive evolution of ρ_{xx} and ρ_{yy} at different locations around tunnel excavation under Method 1.

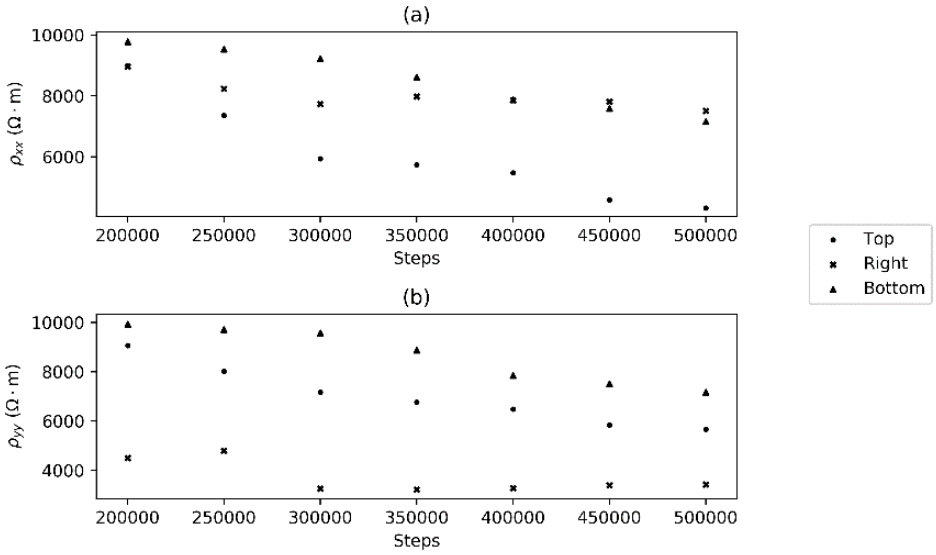

Fig. 5.10. Progressive evolution of ρ_{xx} and ρ_{yy} at different locations around tunnel excavation under Method 2.

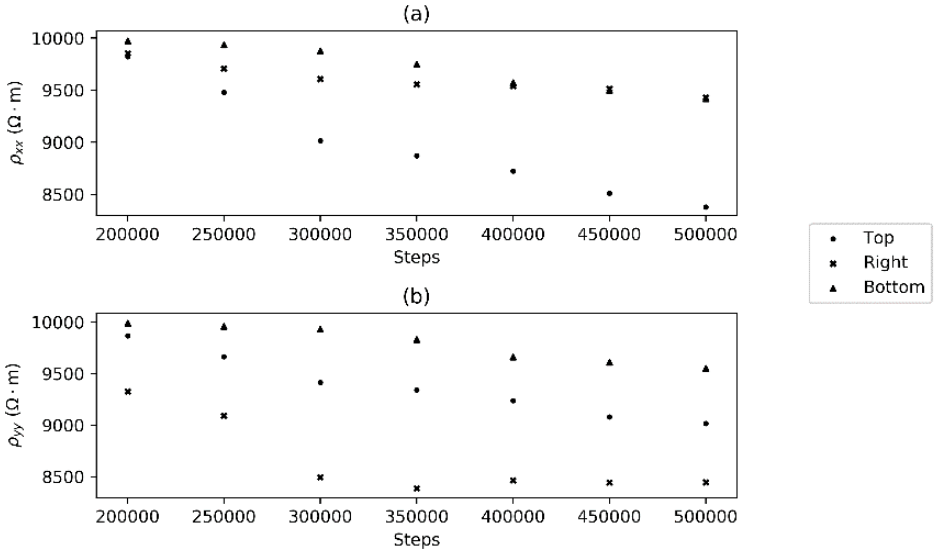

Fig. 5.11. Progressive evolution of ρ_{xx} and ρ_{yy} at different locations around tunnel excavation under Method 3.

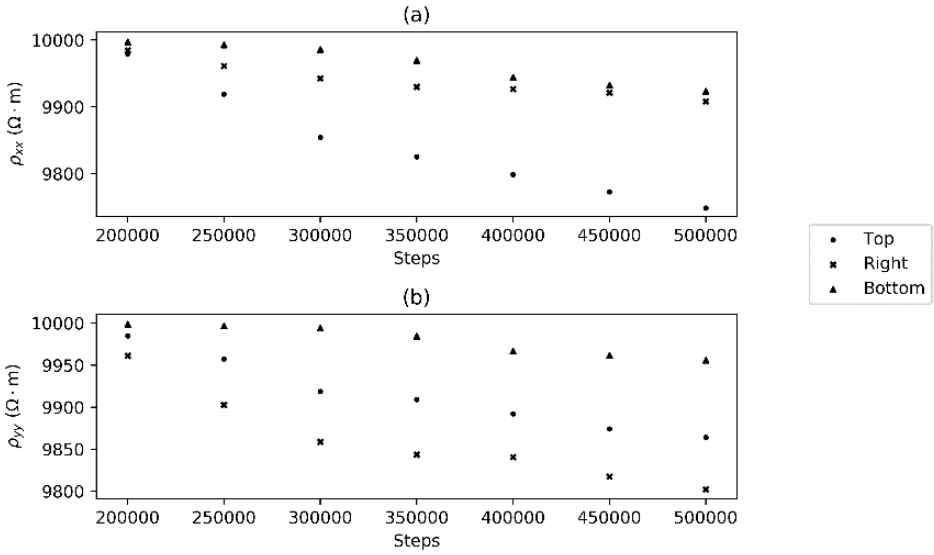

Fig. 5.12. Progressive evolution of ρ_{xx} and ρ_{yy} at different locations around tunnel excavation under Method 4.

5.4 Discussion

Since there are still no similar research that studies equivalent electrical resistivity change due to fracture initiation and propagation in intact rock, it is a challenging issue to validate our proposed method. However, by making analogy between Darcy's law and Ohm's law, our proposed method of estimating equivalent electrical resistivity is reliable. The cubic law which assumes that a fracture is separated by a constant aperture between two smooth parallel plates can define fracture permeability deepening on aperture. However, there are no similar law that defines a relationship between fracture electrical resistivity and aperture. The fracture electrical resistivity should be determined in advance and its change with aperture can not be described quantitatively. Thus, several constant fracture resistivities without resorting to in-situ measurements are assigned to each fracture in Cases 3 and 4. Thus, calculated equivalent resistivity of fractured rock may not be real. A careful check of fracture electrical resistivity is necessary.

The numerically upscaled resistivity is called equivalent resistivity here. To our best knowledge, there is no equivalent resistivity that has been used before yet. Thus, whether it is suitable to use equivalent resistivity should also be further checked.

5.5 Conclusion

In this chapter, the equivalent electrical resistivity of the fractured rock mass was estimated using the unified pipe network model and the FEMDEM fracture model. The unified pipe network model which originally used for modeling fluid flow through fractures was adapted to simulate electric current flow in the fractured rock mass. The initialization and propagation of fractures was characterized by the FEMDEM fracture model. Four cases were used to show the

applicability of the proposed model in estimating the equivalent electrical resistivity of fractured rock mass. The first case is a rock where a single fracture is embedded. It was a simple case which shows that the unified pipe network model was admirably adapted to simulate electric flow in the rock. Nevertheless, a fractured rock mass where fractures were statistically described by the DFN modeling approach was presented in the second case.

The effect of fracture densities on the electrical resistivity was investigated. In the next case, the electrical current flow through the fractures which were developed in an intact rock under a uniaxial compressive test was analyzed. The equivalent electrical resistivities evolution with the propagation of fractures were estimated. In the last case, the electrical resistivities at different locations of the EDZ developed by the tunnel excavation in the Horonobe URL were estimated. Their values changed with the development of the EDZ. Those cases showed the possibilities of extending our proposed to other applications in estimating the electrical resistivities of the fractured rock mass.

References

Aoyagi, K., Ishii, E., 2019. A Method for Estimating the Highest Potential Hydraulic Conductivity in the Excavation Damaged Zone in Mudstone. Rock Mech. Rock Eng. 52, 385–401. https://doi.org/10.1007/s00603-018-1577-z

AOYAGI, K., ISHII, E., ISHIDA, T., 2017. Field Observations and Failure Analysis of an Excavation Damaged Zone in the Horonobe Underground Research Laboratory. J. MMIJ 133, 25–33. https://doi.org/10.2473/journalofmmij.133.25

Baecher, G.B., 1983. Statistical analysis of rock mass fracturing. J. Int. Assoc. Math. Geol. 15, 329–348. https://doi.org/10.1007/BF01036074

Bahr, R., 1997. Electrical anisotropy and conductivity distribution functions of fractal random networks and of the crust: The scale effect of connectivity. Geophys. J. Int. 130, 649–660. https://doi.org/10.1111/j.1365-246X.1997.tb01859.x

Barton, N., 1981. Some size dependent properties of joints and faults. Geophys. Res. Lett. 8, 667–670. https://doi.org/10.1029/GL008i007p00667

Bonnet, E., Bour, O., Odling, N.E., Davy, P., Main, I., Cowie, P., Berkowitz, B., 2001. Scaling of fracture systems in geological media. Rev. Geophys. 39, 347–383. https://doi.org/10.1029/1999RG000074

Bour, O., 2002. A statistical scaling model for fracture network geometry, with validation on a multiscale mapping of a joint network (Hornelen Basin, Norway). J. Geophys. Res. 107. https://doi.org/10.1029/2001jb000176

Brace, W.F., 1975. Dilatancy-related electrical resistivity changes in rocks. Pure Appl. Geophys. PAGEOPH 113, 207–217. https://doi.org/10.1007/BF01592911

Brace, W.F., Orange, A.S., 1968. Electrical resistivity changes in saturated rocks during fracture and

frictional sliding. J. Geophys. Res. 73, 1433–1445. https://doi.org/10.1029/jb073i004p01433

Brace, W.F., Orange, A.S., 1966. Electrical resistivity changes in saturated rock under stress. Science (80-.). 153, 1525–1526. https://doi.org/10.1126/science.153.3743.1525

Brace, W.F., Orange, A.S., Madden, T.R., 1965. The effect of pressure on the electrical resistivity of water-saturated crystalline rocks. J. Geophys. Res. 70, 5669–5678. https://doi.org/10.1029/jz070i022p05669

Brown, S.R., 1989. Transport of fluid and electric current through a single fracture. J. Geophys. Res. 94, 9429–9438. https://doi.org/10.1029/JB094iB07p09429

Caballero Sanz, V., Roubinet, D., Demirel, S., Irving, J., 2017. 2.5-D discrete-dual-porosity model for simulating geoelectrical experiments in fractured rock. Geophys. J. Int. 209, 1099–1110. https://doi.org/10.1093/gji/ggx080

Davy, P., Le Goc, R., Darcel, C., Bour, O., De Dreuzy, J.R., Munier, R., 2010. A likely universal model of fracture scaling and its consequence for crustal hydromechanics. J. Geophys. Res. Solid Earth 115. https://doi.org/10.1029/2009JB007043

Dershowitz, W.S., Herda, H.H., 1992. Interpretation of fracture spacing and intensity.

Dverstorp, B., Andersson, J., 1989. Application of the discrete fracture network concept with field data: Possibilities of model calibration and validation. Water Resour. Res. 25, 540–550. https://doi.org/10.1029/WR025i003p00540

Einstein, H.H., Baecher, G.B., 1983. Probabilistic and statistical methods in engineering geology - Specific methods and examples part I: Exploration. Rock Mech. Rock Eng. 16, 39–72. https://doi.org/10.1007/BF01030217

Elis, V.R., Bondioli, A., Ustra, A.T., Carlos, I.M., Pozzo, H.Â.P.D., 2019. Resistivity imaging for identification of fracture zones in crystalline bedrock in Brazil. Sustain. Water Resour. Manag. 5, 1089–1101. https://doi.org/10.1007/s40899-018-0287-8

Geuzaine, C., Remacle, J.F., 2009. Gmsh: A 3-D finite element mesh generator with built-in pre- and post-processing facilities. Int. J. Numer. Methods Eng. 79, 1309–1331. https://doi.org/10.1002/nme.2579

Heydari, A., Jalali, S.E., Noroozi, M., 2018. Developing a 3D stochastic discrete fracture network model for hydraulic analyses, International Journal of Mining and Geo-Engineering. University of Tehran. https://doi.org/10.22059/IJMGE.2018.244675.594704

Kirkby, A., Heinson, G., 2017. Three-dimensional resistor network modeling of the resistivity and permeability of fractured rocks. J. Geophys. Res. Solid Earth 122, 2653–2669. https://doi.org/10.1002/2016JB013854

Kirkby, A., Heinson, G., Krieger, L., 2016. Relating permeability and electrical resistivity in fractures using random resistor network models. J. Geophys. Res. Solid Earth 121, 1546–1564. https://doi.org/10.1002/2015JB012541

Lei, Q., Latham, J.P., Tsang, C.F., 2017. The use of discrete fracture networks for modelling coupled

geomechanical and hydrological behaviour of fractured rocks. Comput. Geotech. https://doi.org/10.1016/j.compgeo.2016.12.024

Lei, Q., Latham, J.P., Tsang, C.F., Xiang, J., Lang, P., 2015. A new approach to upscaling fracture network models while preserving geostatistical and geomechanical characteristics. J. Geophys. Res. Solid Earth 120, 4784–4807. https://doi.org/10.1002/2014JB011736

Li, S.C., Xu, Z.H., Ma, G.W., 2014. A Graph-theoretic Pipe Network Method for water flow simulation in discrete fracture networks: GPNM. Tunn. Undergr. Sp. Technol. 42, 247–263. https://doi.org/10.1016/j.tust.2014.03.012

Lisjak, A., Grasselli, G., 2014. A review of discrete modeling techniques for fracturing processes in discontinuous rock masses. J. Rock Mech. Geotech. Eng. https://doi.org/10.1016/j.jrmge.2013.12.007

Lisjak, A., Grasselli, G., Vietor, T., 2014. Continuum-discontinuum analysis of failure mechanisms around unsupported circular excavations in anisotropic clay shales. Int. J. Rock Mech. Min. Sci. 65, 96–115. https://doi.org/10.1016/j.ijrmms.2013.10.006

Magnusdottir, L., Horne, R., 2012. CHARACTERIZATION OF FRACTURES IN GEOTHERMAL RESERVOIRS USING RESISTIVITY, in: PROCEEDINGS, Thirty-Seventh Workshop on Geothermal Reservoir Engineering.

Munjiza, A., 2004. The Combined Finite-Discrete Element Method, The Combined Finite-Discrete Element Method. John Wiley & Sons, Ltd, Chichester, UK. https://doi.org/10.1002/0470020180

Munjiza, A., Owen, D.R.J., Bicanic, N., 1995. A combined finite-discrete element method in transient dynamics of fracturing solids. Eng. Comput. 12, 145–174. https://doi.org/10.1108/02644409510799532

Priest, S.D., 1993. Discontinuity Analysis for Rock Engineering, Discontinuity Analysis for Rock Engineering. Springer Netherlands. https://doi.org/10.1007/978-94-011-1498-1

Ren, F., Ma, G., Wang, Y., Li, T., Zhu, H., 2017. Unified pipe network method for simulation of water flow in fractured porous rock. J. Hydrol. 547, 80–96. https://doi.org/10.1016/j.jhydrol.2017.01.044

Roubinet, D., Irving, J., 2014. Discrete-dual-porosity model for electric current flow in fractured rock. J. Geophys. Res. Solid Earth 119, 767–786. https://doi.org/10.1002/2013JB010668

Saevik, P.N., Jakobsen, M., Lien, M., Berre, I., 2014. Anisotropic effective conductivity in fractured rocks by explicit effective medium methods. Geophys. Prospect. 62, 1297–1314. https://doi.org/10.1111/1365-2478.12173

Sanz, V.C., Roubinet, D., Demirel, S., Irving, J., 2017. 2.5-D discrete-dual-porosity model for simulating geoelectrical experiments in fractured rock. Geophys. J. Int. 209, 1099–1110. https://doi.org/10.1093/gji/ggx080

Schrauf, T.W., Evans, D.D., 1986. Laboratory Studies of Gas Flow Through a Single Natural Fracture. Water Resour. Res. 22, 1038–1050. https://doi.org/10.1029/WR022i007p01038

SEKINE, I., NISHIMAKI, H., ISHIGAKI, K., HARA, T., SAITO, A., 1997. Influence of fracture and its filling materials on rock resistivity. J. Japan Soc. Eng. Geol. 38, 213–223. https://doi.org/10.5110/jjseg.38.213

Tsang, Y.W., Witherspoon, P.A., 1981. Hydromechanical behavior of a formable rock fracture subject to normal stress. J. Geophys. Res. 86, 9287–9298. https://doi.org/10.1029/JB086iB10p09287

Wang, C.-Y., Sundaram, P.N., Goodman, R.E., 1978. Electrical Resistivity Changes in Rocks During Frictional Sliding and Fracture, in: Rock Friction and Earthquake Prediction. Birkhäuser Basel, pp. 717–731. https://doi.org/10.1007/978-3-0348-7182-2_10

Wolfsberg, A., 1997. Rock fractures and fluid flow, contemporary understanding and applications, Rock fractures and fluid flow, contemporary understanding and applications. National Academy Press USA. https://doi.org/10.1029/97eo00345

Chapter 6

Conclusion and future works

6.1 Main results

Fractures (e.g., faults, joints) provide pathways for fluid flow as hydraulic conductors or barriers that prevent flow across them. Characterization and detection of fractures in fractured rock have been of great interest in geotechnical, geological, geophysical, and hydraulic engineering practices.

Chapter 1 provides background information of fracture network and fractured rock physical properties (e.g., permeability, electrical resistivity, seismic velocity).

Chapter 2 presents a method for estimating fractured rock effective permeability by using discrete fracture networks constrained by electrical resistivity data. The conclusions are as follows:

The power-law length distributions with scaling exponents in DFN models are constrained using in-situ measured electrical resistivity data. The electrical resistivity and effective permeability of a DFN model are calculated analytically using a symmetric self-consistent method and Oda's crack tensor theory, respectively. An optimized scaling exponent of DFN model can be determined. To validate our proposed method, two case studies were carried out in the Mizunami Underground Research Laboratory (URL), central Japan. For Case 1, a DFN model with an initial scaling exponent a = 3.5 was assumed unacceptable because its electrical resistivity was 3094 $\Omega \cdot m$ which was higher than in-situ electrical resistivity. A DFN model with an optimal scaling exponent a = 3.0 was determined because its electrical resistivity (2064 $\Omega \cdot m$) is similar to in-situ measured resistivity. The corresponding effective permeability $\bar{k}$ = 6.5 × 10^{-16} m^2, which was only slightly smaller than in-situ permeability 1.0 × 10^{-15} m^2. For Case 2, a DFN model with an optimal a of 2.8 was determined. The corresponding $\bar{k}$ estimated analytically using Oda's crack tensor theory was 1.03 × 10^{-14} m^2, which was also similar to in-situ permeability 2.67 × 10^{-15} m^2. The two case studies show that our proposed method can construct realistic DFN models using in-situ measured resistivity data. The rational effective permeabilities of fractured rock masses can be further estimated. To improve our proposed method, numerical based upscaling methods can replace Oda's crack tensor to estimate effective permeability.

Chapter 3 presents a conceptual model interpreting an increase in seismic velocity and electrical resistivity after a tunnel excavation in fractured rock. The conclusions are as follows:

A special phenomenon that electrical resistivities and seismic velocities around the tunnel surface were increased after the tunnel excavation was observed the Horonobe URL. To interpret such phenomenon, a conceptual model which considered the desaturation process caused by the

ambident air in the tunnel was proposed. The Kelvin's equation was used to relate equivalent capillary pressure applied at the tunnel surface and the relative humidity of the air in the tunnel. The hydromechanical analysis was conducted jointly using TOUGH2 and FLAC3D. Using the simulated gas saturations in the rock mass, the electrical resistivities and seismic velocities were calculated using the Archie's equation and Biot-Gassmann poroelasticity theory. Assuming a constant relative humidity of the tunnel air and prescribing initial and boundary conditions, the hydromechanical analysis was simulated for 6 months. The effect of desaturation process on the change of the stress state in the rock mass was minor thought the analysis. The rock gas saturations driven by the desaturation process increased after the excavation though the increase rate was decreasing. The electrical resistivities and seismic velocities in the rock mass were also increased. The simulation result was in accordance with the observed in the Horonobe URL. Though the proposed conceptual model well explained the phenomenon, other explanations which were discussed in the Discussion were also possible. More field data were necessary to further validate our proposed model.

Chapter 4 presents a model which links a unified pipe network method and FEMDEM fracture model for estimating equivalent permeability of fractured rock masses. The conclusions are as follows:

The unified pipe network and the FEMDEM fracture model were jointly combined to estimate the equivalent permeability of the fractured rock mass. The unified pipe network used matrix pipes which represent the 2D rock matrix and fracture pipes which represent the 1D fractures. The FEMDEM fracture model was used to characterize the initialization and propagation of fractures in the rock mass. To validate our proposed model, four representative cases were carried out. In the first case, the equivalent permeability of a rock mass in which a single fracture was embedded was estimated. The effect of fracture orientations on the permeability was also studied. The second case was a fractured rock where multiple fractures were generated by the DFN modeling approach. The effect of fracture density on the equivalent permeability was studied. Another case was an intact rock under a uniaxial compression test. The last case an in-situ site numerical investigation of the initialization and propagation of fractures due to the tunnel excavation. These cases showed possibilities of the applicability of our proposed model in estimating the permeability of fractured rock in engineering practice.

Chapter 5 presents a numerical method that calculates the equivalent fractured rock electrical resistivity through a combination of the hybrid FEMDEM fracture model and the unified pipe network model. The conclusions are as follows:

The equivalent electrical resistivity of the fractured rock mass was estimated using the unified pipe network model and the FEMDEM fracture model. The unified pipe network model which originally used for modeling fluid flow through fractures was adapted to simulate electric

current flow in the fractured rock mass. The initialization and propagation of fractures was characterized by the FEMDEM fracture model. Four cases were used to show the applicability of the proposed model in estimating the equivalent electrical resistivity of fractured rock mass. The first case is a rock where a single fracture is embedded. It was a simple case which shows that the unified pipe network model was admirably adapted to simulate electric flow in the rock. Nevertheless, a fractured rock mass where fractures were statistically described by the DFN modeling approach was presented in the second case. The effect of fracture densities on the electrical resistivity was investigated. In the next case, the electrical current flow through the fractures which were developed in an intact rock under a uniaxial compressive test was analyzed. The equivalent electrical resistivities evolution with the propagation of fractures were estimated. In the last case, the electrical resistivities at different locations of the EDZ developed by the tunnel excavation in the Horonobe URL were estimated. Their values changed with the development of the EDZ. Those cases showed the possibilities of extending our proposed to other applications in estimating the electrical resistivities of the fractured rock mass.

6.2 Future works

The relationship between fractures and their geophysical properties, such as permeability, electrical resistivity and seismic velocity is a quite challenging issue. More efforts should be done to advance it. Several aspects can be done to improve our methods proposed in the thesis such as:

1. In Chapter 2, an analytical Oda's crack tensor theory and a symmetric self-consistent method were used to estimate fractured rock permeability and electrical resistivity, respectively. Instead, accurate numerical approaches which estimate permeability and electrical resistivity can replace our analytical formulas to obtain relative accurate results. In future, such 3D numerical modeling approaches of DFN models to estimate upscaled permeability and electrical resistivity requires developed. Furthermore, in-situ measured electrical resistivity in Chapter 2 was used to constrain the DFN model. Other geophysical data, such as seismic velocity can also be used to constrain the DFN model.
2. Chapter 3 only focused on the desaturation process in the EDZ to explain electrical resistivity and seismic velocity change around a tunnel excavation. Instead, a renaturation process is also necessary for further analysis to explain electrical resistivity and seismic velocity decrease after their increases after a tunnel excavation. Furthermore, a constant relative humidity was assumed in the conceptual model. The seasonal variation of relative humidity is more realistic. The parameters assumed in the models require sensitivity analysis to study their effects.
3. Chapters 4 and 5 both focused on numerical simulations of equivalent permeability and electrical resistivity of fractured rock mass. Their results should be compared with

experimental or in-situ measured data to validate our proposed method. The permeability reduction due to a closure effect of micro cracks in the sample under a uniaxial compression test was not considered in Case 3 in the Chapters 4 and 5. In future, a sample with existed cracks under a uniaxial compression test should be considered in the modeling approach.